KTH Royal Institute Of Technology
The Department of Civil and Architectural Engineering
Degree project in structural Engineering and Bridges

Polytechnic Of Turin
The Department of Structural, Geotechnical and Building Engineering

CFD Analysis for Wind Load Assessment

Wind-induced vibrations in long slender arch bridges: Bomarsunds Bridge

Examiners: The Prof. Raid **Karoumi**
The Prof. Cecilia **Surace**

Supervisors:The Prof. Jhon **Leander**
The Ing. Marco **Civera**

Fatiha El Azrak

November 2024

“*To my father,*

my first and greatest teacher,

whose guidance and strength

shaped my path.”

Abstract

The trend in recent years of building longer and slender bridges has introduced new challenges to ensure their stability and strength. This master thesis focuses on the effects of wind-induced vibrations in the context of long, slender arch bridges, particularly the recently constructed Bomarsunds Bridge between two islands in Finland.

The primary goal of this study is to comprehensively analyze the dynamic behavior of the bridge under wind loading, as wind-induced vibrations pose potential risks to its safety and structural integrity. The slender hangers of the bridge, mainly within the central span, have exhibited significant vibrations, necessitating an in-depth investigation to understand the bridge's response to wind forces. Computational fluid dynamics (CFD) simulations were performed using Ansys Fluent to design a more accurate wind load acting on the structure. Using CFD analysis, the behavior of a given bridge section subjected to wind loading can be described. In this way, it is possible to calculate the aerodynamic coefficients that characterize that given section (i.e. Strouhal number, drag coefficient, etc...). The study focuses on the rectangular hollow steel section representative of hangers and how its design influences the simulation results. By integrating advanced computer simulations and CFD analysis, the research addresses the complex challenges of the interaction of the structure with fluid dynamic phenomena, which are critical to understanding and mitigating vibration hazards in bridges. The results of this study provide an in-depth view of the wind load on the structure and allow the dynamic behavior of long and narrow arch bridges to be determined.

By analyzing the complex interactions between the bridge and wind forces, the study contributes valuable insights into the field of wind engineering. Ultimately, this research plays a key role in ongoing efforts to design robust, safe, and resilient bridge structures that can effectively resist wind-induced vibration and ensure the safety of the infrastructure.

Acknowledgments

I extend my heartfelt gratitude to Professor Raid Karoumi and Professor John Leander for entrusting me with the opportunity to delve into this captivating case study. Your invaluable guidance, unwavering support, and mentorship have been instrumental during the completion of this thesis. Your depth of knowledge and expertise has been a source of inspiration and amazement. I aspire to emulate your dedication and passion. Thank you for rekindling my passion for knowledge and research.

I am grateful to Professor Cecilia Surace and Doctor Marco Civera for their support, encouragement, and assistance. Thank you for embracing my proposal to work on this case study, and exhibiting unwavering confidence in my skills and abilities. Your advice and expertise proved to be indispensable in accomplishing this research project. I extend my heartfelt appreciation to Marco for your patience and promptness in offering valuable guidance. Your support has been invaluable.

I am deeply grateful to all my colleagues and friends who have supported me in this academic endeavor. Last but not least, I would like to express my sincere gratitude to my family for their constant encouragement, understanding, and support throughout this journey. I would like to conclude by saying that much of the good I do comes from gratitude for the way my parents raised me.

Stockholm, November 2023.
Fatiha El Azrak

Contents

List of Figures

List of Tables

Introduction

Bridges pose an enthralling challenge in civil engineering. Designers continuously aspire to surpass records by constructing longer, lighter, and more slender structures. Presently, bridges have evolved to embrace ever more intriguing and innovative materials and shapes. As well as being a landmark of engineering advancement, they symbolize the progress of a nation. Bridges are constructed to withstand progressively demanding loads and varied weather conditions. Therefore, their design and maintenance are fundamental to their safety, integrity, and efficiency.
The sophistication of bridge architecture poses challenges, particularly in confronting natural forces. Wind loading emerges as a relevant obstacle for bridges, triggering dynamic responses that may result in irreversible damage. Wind engineering enhances knowledge of the impact of wind on bridges, unveiling intricate phenomena like vortex shedding that could jeopardize their structural integrity.

In this thesis, the focus is on a particular newly built metal bridge, located on an island between Finland and Sweden. Its hangers are affected by excessive vibration at ordinary wind speeds for the area in which it is located.
The goal is to reveal how these hangers respond to the action of the wind, by using Computational Fluid Dynamics (CFD) investigations. The process involves exploring steady-state aerodynamics, observing transient responses at different wind speeds, diving into the complexity of 3D interactions, and applying standards such as Eurocode for wind load calculations.

Scope of the thesis: The objective of this research is to comprehend the interaction between wind and hangers in a dynamic environment. The primary research questions focus on the range of frequencies that represent the dynamism of the structure, considering various models with different numbers of hangers. This will help us to identify their interaction and its effect on the global response. Moreover, the research aims to understand the dynamic responses of hangers in different time domains and varying wind conditions with a logical progression of information. This study within the field of aerodynamics aims to identify the effects of wind-induced forces on significant

aerodynamic parameters, specifically the aerodynamic coefficient, strouhal number, and frequency domain. The research also explores the influence of geometric features, including rounded edges.
A comparative study is a crucial aspect of the research as it investigates the interactions between hangers in multi-section models and identifies the disparities in aerodynamic performance between two-dimensional and three-dimensional illustrations of hangers at different wind velocities. The research aligns with practical applications, and the research questions cover the application of Eurocode standards for wind load calculations. The study examines the agreement between these standards and simulated critical wind speeds for vortex shedding in bridge hangers. It also explores the influence of incorporating shedding frequencies on calculations of inertial wind force.

Limitations: While embarking on this exploration, it's crucial to acknowledge the limitations. The models, though intricate, have been simplified to achieve a balance between complexity and computational feasibility, the study focuses only on the hangers of the bridge. The digital domain has limitations and the results may not be universally applicable to all bridge types and conditions: the dimension and the inclinations are of the chosen section of the Bomarsund Bridge. Additionally, the field of CFD presents numerous intriguing possibilities that cannot all be explored due to the restrictions of time and workload involved in a thesis research study. Moreover, the computational tools used for simulation are powerful yet demanding, requiring lengthy processing times and high computational loads. To obtain satisfactory results in a reasonable time frame, simplification of the models created is often necessary.

This study aims to provide practical insights for the fields of bridge and wind engineering. Through the exploration of wind-hanger dynamics, it seeks to inform improved design practices, enhance safety protocols, and contribute to the development of bridges that not only stand tall but also sway elegantly with the wind.

Chapter 1

Wind Load Analysis in Bridge Design

1.1 Wind Flow

A flow over a body induces two important forces, a force in the direction of the flow, called Drag that tends to move the body into the same direction, and a force normal to the first, that tends to move the stationary body in the opposite direction, called lift. The Drag Force

1.1.1 Turbulence and the Boundary Layer

Turbulence and the boundary layer are fundamental aspects of fluid dynamics. The boundary layer was introduced by Ludwig Prandtl, which revolutionized the study of fluid mechanics[2]. His solution consists of dividing the fluid flow into two zones, an inviscid outer flow zone, and an inner flow zone, the boundary Layer. It is a region near a surface where the fluid velocity changes from zero to a maximum. Understanding the boundary layer is critical because it's where the effect of the viscus layer can´t be neglected and many wind-induced effects on structures originate.

Inside the boundary layers, three different flow-type zones can be distinguished, to define them it is important to introduce a fundamental parameter in the aerodynamic field: the Reynolds number(Re). It is a dimensionless quantity used to define the ranges of flow regimes.

$$Re = \frac{\rho \cdot V \cdot L}{\mu} \tag{1.1}$$

Where:

Re is the Reynolds number.

ρ is the density of the fluid.

V is the velocity of the fluid.

L is a characteristic length.

μ is the dynamic viscosity of the fluid.

Flow regimes are classifications of fluid flow, typically categorized as laminar or turbulent flow with a transition face between these two. Laminar flow is characterized by smooth and orderly movement of fluid particles on parallel streamlines with minimal mixing [3]. This flow regime prevails at low Reynolds ($Re < 10^3$). The turbulent regime is the most complex regime, there is no streamlined or predicted direction for the fluid particles, and the flow is chaotic and irregular. It occurs at high Reynolds. Between the two regimes, there is a third transitional regime, where both regimes coexist [2].

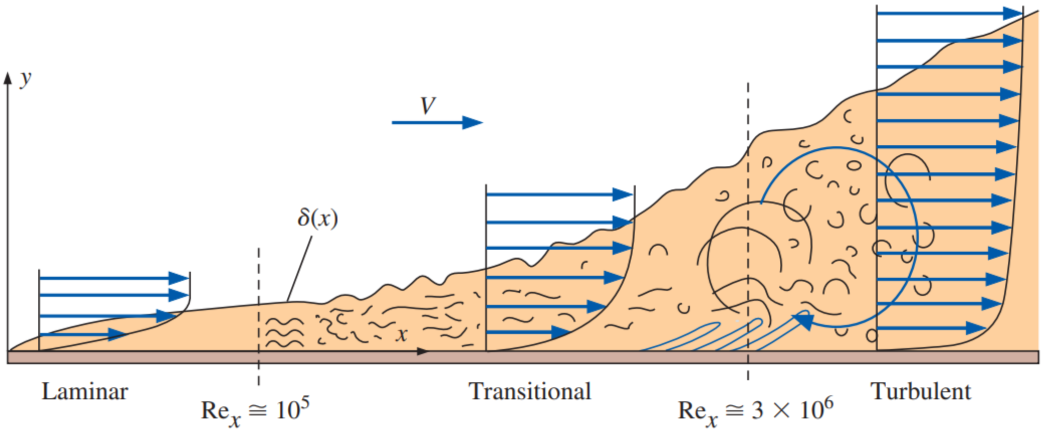

Figure 1.1: Transition of the laminar boundary layer on a flat plate into a fully turbulent boundary layer. Reprinted from "Fluid Mechanics: Fundamentals and Applications" by Cengel, Yunus A., and John M. Cimbala. [2]

1.1.2 Streamlined and Bluff Body

In the field of fluid dynamics, the shape and size of an object placed in a fluid flow has a significant influence on the fluid dynamics. They can be categorized into two macro groups, streamlined bodies and bluff bodies. The latter have distinctive characteristics: square, non-aerodynamic, and irregular. Their unique shape causes phenomena such as flow separation, turbulence, and pressure changes both around and downstream of the object.

A critical parameter in analyzing the behavior of such bodies is drag. It is the sum of the resistance of the profile and it is the sum of two main components: pressure drag and skin friction drag. The extent to which either of these components dominates the total drag depends on the shape of the body. If the viscous component, i.e. that due to skin friction, is the main contributor to the drag forces, we classify the body as streamlined. On the other hand, if pressure is a significant contributor to drag, the body falls into the bluff category [4].
It is important to understand the fluid dynamic difference between streamlined and bluff bodies. Bluff bodies tend to induce flow separation, typically at the corners of the body. This separation leads to the creation of a large wake region characterized by low pressure, which causes high drag. Aerodynamic bodies, on the other hand, keep the flows together, reducing flow separation and consequently drag [4].

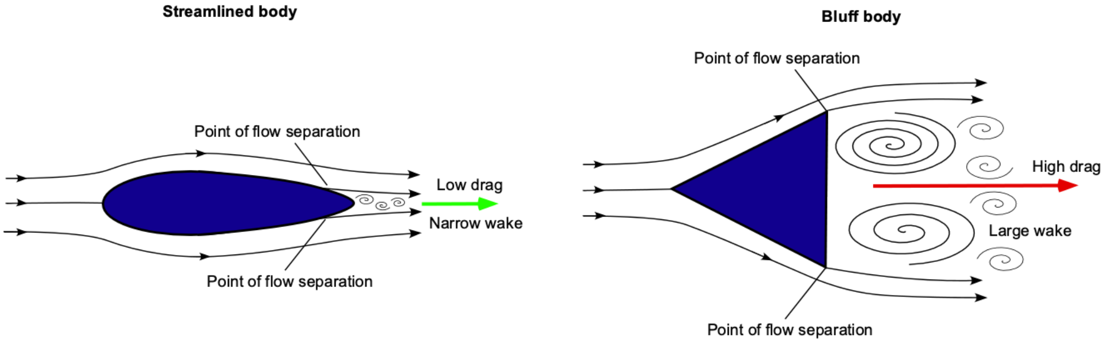

Figure 1.2: fundamental differences between the flows of streamlined versus bluff bodies. Reprinted from "Introduction to Aerospace Flight Vehicles " by J. Gordon Leishman. [4]

1.1.3 Flow Patterns in Fluid Dynamics

The study of flow patterns is essential to understanding the flow regime and the shape of the body. At different Reynolds numbers, different flow patterns can be identified, characterized by different types of turbulence. What occurs is a wake, a region of disturbed flow that trails behind an object placed in a fluid medium. This wake often contains turbulence and eddies of varying sizes. It is essential to recognize the characteristics of this wake, the frequency of oscillation, and the associated drag. Furthermore, by observing the eddies that form within the wake and observing their symmetries and asymmetries, it is possible to identify the Reynolds range of the flow.

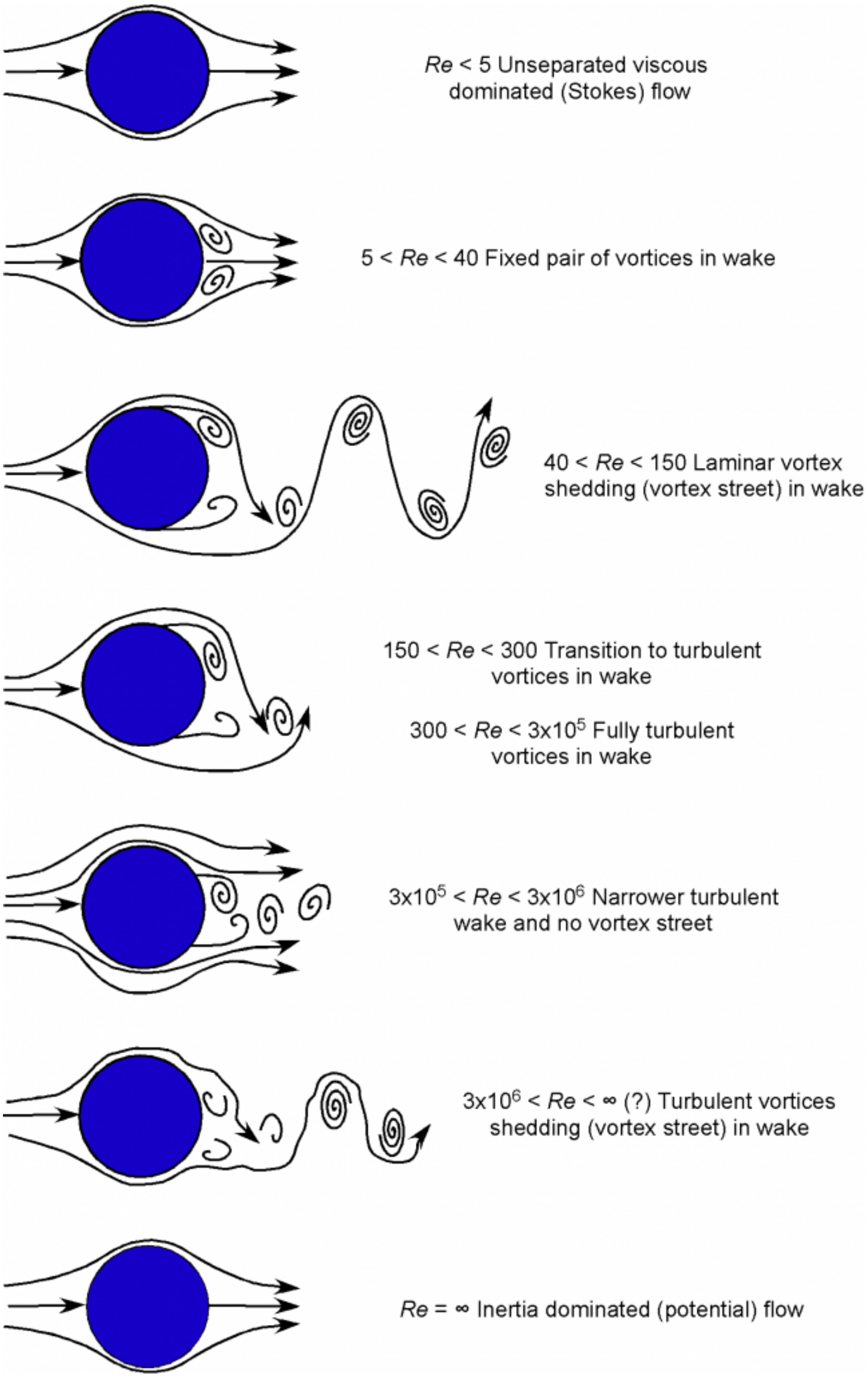

Figure 1.3: Different flow states over a circular cylinder, dependence on the Reynolds number. Reprinted from "Introduction to Aerospace Flight Vehicles " by J. Gordon Leishman. [4]

At low Reynolds numbers, where viscous effects dominate, the flow is typically described as a creeping or Stokes flow [4], with no turbulence or vorticity.
At slightly higher, but still relatively low, Reynolds numbers, a stable pair of symmetrical eddies tends to form in the wake of the body, resulting in a relatively smooth flow.
As the Reynolds number increases, the behavior of the wake changes. The eddies al-

ternately spread out in a Von Kármán vortex road pattern, creating an unstable flow. Although this flow is unstable, no time-averaged unstable lift is generated due to the asymmetry in the flow[4].

At higher Reynolds numbers, the flow patterns become more turbulent, and boundary layer separation can occur further downstream. The result is a narrower wake, corresponding to less drag.

At very high Reynolds numbers, the inertial force overcomes viscosity resistance. The flow patterns form a wake that closely resembles an inviscid flow. In these cases, the object experiences no resistance, neither lift nor drag. This condition is known as d'Alembert's paradox [4], which highlights the complex interaction between viscous and inertial effects in flow dynamics.

1.2 Aerodynamic Quantities

The study of aerodynamic coefficients, including drag, lift, moment coefficients, and Strouhal number, plays a vital role in the design of wind loads on the structure. These coefficients provide valuable insight into the forces and moments experienced by the structure when subjected to fluid flow.

In this section, the theoretical background and experimental methods for the determination of drag, lift, moment coefficients, and Strouhal are reviewed. Theoretical models and equations are discussed to provide a basis for understanding these quantities. In addition, experimental techniques such as wind tunnel testing and computational fluid dynamics (CFD) are presented as a means of determining these coefficients in practice.

1.2.1 Drag Coefficient: C_D

The drag coefficient is a dimensionless quantity that characterizes the resistance encountered by an object subjected to a fluid flow, it is representative of the resistance parallel to the free flow direction. It plays a crucial role in determining the aerodynamic drag force acting on the object. The drag coefficient of a stationary body is influenced by various factors, including the shape of the object, the Reynolds number, and the surface roughness.

$$C_D = \frac{F_D}{\frac{1}{2}\rho U^2 A} \tag{1.2}$$

It is determined by the equation1.2, where ρ and U are the density and velocity of the fluid, respectively, and A is the reference area; in the case of 2D analysis, the area is given by the unit value multiplied by the characteristic dimension d.

1.2.2 Lift Coefficient: C$_L$

The lift coefficient is another important parameter used to characterize the aerodynamic behavior of an object immersed in a fluid flow. It is more relevant for three-dimensional simulations, since it is a force normal to the drag resistance, in the opposite direction of gravity. In two-dimensional analysis, it is a resistance acting perpendicular to the flow direction, oscillating around a null value, and is responsible for generating an upward force on the object. It represents the ratio between the lift force experienced by the object and the dynamic pressure of the fluid. The lift force and the resistance force are nothing more than the two components, one parallel and the other perpendicular to the flow of the total resistance of the solid subjected to a fluid flow.

$$C_L = \frac{F_L}{\frac{1}{2}\rho U^2 A} \tag{1.3}$$

Similar to the coefficient of resistance, the lifting coefficient is influenced by various factors, including the shape of the object, the Reynolds number, and the roughness of the surface. The lifting coefficient plays a crucial role in determining the lifting force generated by an object, which can be any solid surface.

By studying the lifting coefficient and its behavior for cylinders of different shapes and in variable flow conditions, it is possible to obtain information on the aerodynamic forces acting on structures and improve design and performance in many applications. It is a fundamental value for the determination of another crucial parameter, the Struhal number 1.2.4.

1.2.3 Moment Coefficient: C$_M$

The moment coefficient is a dimensionless parameter used to describe the rotational or torsional forces suffered by a body subjected to fluid flow. Provides information on the distribution of moments along the length of the object, indicating how this one responds to aerodynamic loads.

Factors such as geometry, flow conditions, and fluid properties influence the value of the coefficient. It represents the relationship between the moment experienced by the object and the dynamic pressure of the fluid flow.

A higher momentum coefficient indicates a greater tendency of the section to rotate or twist under the influence of fluid flow and therefore more vulnerable to torsional effects.

$$C_M = \frac{M}{\frac{1}{2}\rho U^2 d^2} \tag{1.4}$$

It is a fundamental parameter in order to assess the structural stability, and integrity of a structure during the design phase.

1.2.4 Strouhal number: S_t

The Strouhal number (St) is a dimensionless number used in fluid dynamics to characterize the flow-induced oscillations or vortex shedding behind an object placed in a fluid flow. It is defined as the ratio of the shedding frequency to the product of the characteristic length and the flow velocity. It helps in understanding the dynamic response and the energy transfer between the fluid and the structure. The Strouhal number is named after the Czech physicist Vincenc Strouhal, who first studied this phenomenon in the late 19th century.

$$S_t = \frac{fd}{U} \tag{1.5}$$

The Strouhal number is particularly relevant when studying vortex shedding behind an object. When fluid flows around an obstructing body, such as a cylinder, it can lead to the formation of eddies. If the shedding frequency (f) of these eddies is similar to the natural frequency of the body, this can lead to resonance, causing vibrations and even structural damage. The shedding frequency is determined by the lift signal as explained in section 1.2.2, so for its determination it is necessary to use computational fluid dynamic analysis.

In the context of the Eurocode and structural design, the Strouhal number is used to evaluate the effects of wind-induced vibrations on structures. If the shedding frequency is equal to the natural frequency of the structure, resonance can occur, which is an important consideration in ensuring the safety and stability of structures.

A low Strouhal number typically indicates that the vortex shedding frequency is well-matched to the natural frequency of the structure. In such cases, the potential for resonant vibrations is higher. A higher Strouhal number indicates that the vortex shedding frequency is less likely to match the natural frequencies of the structure. For flows around bluff bodies, the Strouhal number usually ranges from 0.1 to 0.3. However, it is important to note that these values can vary based on factors such as the Reynolds number, which characterizes the flow regime, and the specific dimensions and shape of the cross-section.

In practice, the Strouhal number is used to predict and mitigate wind-induced vibrations in structures. By adjusting the shape, size, or orientation of objects and structures, the shedding frequency can be influenced and the likelihood of resonance reduced.

1.2.5 Experimental Determination of Aerodynamic Coefficients

The experimental determination of aerodynamic coefficients is a fundamental aspect of the field of aerodynamics. It involves performing physical experiments to measure and quantify the aerodynamic forces acting on an object immersed in a fluid flow, typically air or water with some fluid colorants, to detect the wave that forms behind the object. In the most common case, the body is scaled and fixed, for more advanced experiments a small motion is added to its support. These experiments can be challenging due to factors such as controlled Reynolds number, flow turbulence, and, in particular, model scaling issues. However, they are essential as the aerodynamic coefficients provide crucial insight into the performance, stability, and behavior of the object in different flow regimes. A variety of methods are used, ranging from wind tunnel testing to full-scale flight testing, the latter being the most recent in the aerospace field, and the data obtained is used to inform decisions relating to performance, stability, control, and overall design optimization.

Wind Tunnel testing

One of the best-known methods of aerodynamic testing is the wind tunnel. A historic and classic method, it allows measurements to be taken on models of various scales. Its advantages are undoubtedly its versatility and controllability. In practice, a scale model is placed in the specially designed gallery. The tunnel has a very simple structure, a long and narrow chamber with fans at the end that allows the wind to be simulated under controlled conditions. The geometry of the tunnel is such that there is a regular and constant flow, minimizing disturbances that could affect the validity of the measurements. Inside the tunnel, there is usually support on which the test body is positioned, which is usually fixed. This fixed body model simplifies the test procedure.

The tests are carried out at different speeds and also at different angles of attack in order to reproduce the real regimes and flow conditions. As far as the speed is concerned, the variation procedure is quite simple as it can be controlled by the fans at the ends of the tunnel. A more advanced method is to use the variable speed drive, which would allow more precise control of the wind parameters.

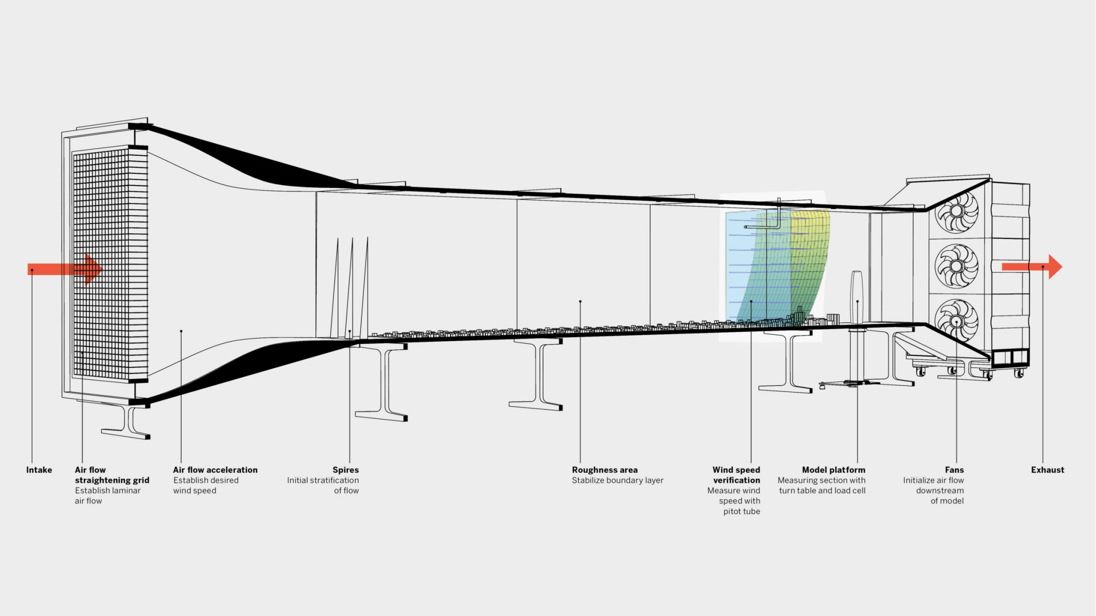

Figure 1.4: Skidmore, Owings & Merrill LLP. (n.d.). Wind Tunnel Testing for Supertall Buildings. SOM

For the actual measurement of the aerodynamic forces and moments generated by the flow, a range of instruments and sensors are used, with varying degrees of sensitivity, accuracy, and precision. The classics are force balances, which make it possible to measure the total force and moment exerted by the model. Another basic measurement parameter is the pressure distribution on the surface of the model, which is monitored by pressure sensors. A third essential measurement tool is strain gauges, which allow the deformation of the model to be measured and the response of the model to the applied wind force to be studied. The gauges presented here are the basis for a simplified test, of course, there are other instruments used depending on the purpose of the simulation. It is important to focus on the dimensions of these instruments, the scale models have dimensions of the order of a centimeter, rarely a meter, so to influence the measurements as little as possible, the instruments must be of millimeter size.

The next step is data collection, using automated data acquisition systems. These collect data in real-time, recording all the measurement parameters in such a way as to provide a reading of the model's response over time. The final step is data analysis for the determination of drag, moment and lift coefficients.
To verify the accuracy of the data obtained, the measured forces and moments are calibrated against reference parameters such as dynamic pressure and the characteristic dimensions of the object. In this calibration phase, statistical principles are used to minimize errors and uncertainties in the measurements made. Finally, the normalized

force and moment values are compared with theoretical models or reference data. This step in the experimental process is fundamental as it allows the data obtained to be validated.

This type of test has several advantages, including controllability and repeatability. It also allows accurate observation of the vorticity effects of the flow and how this interacts with the structure at the boundary layer level. This type of test has important validity and reliability in the field of aerodynamics. Furthermore, the simplicity of this type of test makes it possible to effectively reproduce different flow conditions on any type of object to be analyzed, of course always within the limits of the tunnel scale.

The wind tunnel test is a standardized test governed by specific guidelines and protocols. These cover every single step of the test, starting with the dimensions of the tunnel, the mounting, and the scale of the object to be placed in the tunnel. It is a very sensitive test and requires extreme accuracy. These standards are often provided by organizations such as the American Society of Civil Engineers (ASCE) or the International Organisation for Standardisation (ISO).

Computational Fluid Dynamics

A more modern branch is Computational Fluid Dynamics (CFD), a numerical simulation technique used to analyze and predict the behavior of fluid flows around objects. It has become a powerful tool for determining the drag coefficients of structures and for visualizing the dynamic effects of flows. Nowadays, there is a wide range of software that can be used to simulate any type of structure under any condition.

In very simplified terms, CFD analysis involves solving the equations governing fluid flow, i.e. the Navier-Stokes equations, using numerical methods. A flow domain of the simulated fluid is defined, the dimensions of which must be much larger than those of the object being traversed in order to obtain an accurate simulation. This domain is then divided into small computational cells using a meshing process, and the equations for each cell are solved iteratively to obtain a solution that represents the flow behavior.

To perform a CFD analysis, a simulation setup is first established. This involves a number of steps, the first of which is the definition of the geometry of the structure and the surrounding domain, where the domain is sized according to a basic parameter which is the characteristic length of the structure. This is followed by the meshing phase, which consists of selecting the type, order, and size of the meshing unit. The boundary conditions and fluid properties must then be defined. This gives you the basic

model on which to run simulations of the flow of interest.
The actual simulation parameters include the choice of turbulence model, which captures the effects of turbulence in the flow, and the discretization scheme, which approximates the governing equations. These parameters have a significant impact on the accuracy and reliability of the results and must be carefully selected based on the specific flow conditions and the desired level of accuracy.

Once the CFD simulation has been performed, the post-processing phase begins, which consists of extracting the desired data. Post-processing also includes visualization of flow patterns, pressure distribution, velocity, turbulence, and other flow variables to provide detailed information on the dynamics of the flow and how it interacts with the structure. These visualizations and contours help to identify aerodynamic concepts that are analytically very complex to determine, such as flow separation, eddies, their distribution and symmetry, and other flow phenomena that contribute to the generation of aerodynamic forces and moments.

It is important to note that CFD analysis is subject to some limitations and uncertainties, its simplicity can lead to completely incorrect solutions. The accuracy of the results depends on the quality and size of the mesh, especially near the walls of the structure. The turbulence model chosen and the hypotheses made during the simulation setup influence the final data, it is necessary to have the settings adapted to the model to be simulated. There are guidelines to follow, but each analysis has its own peculiarities. Validation of CFD results with experimental data is often performed to ensure their reliability and to identify any discrepancies.
However, CFD is a valuable and efficient tool for evaluating the effects of flows on an object, especially when combined with wind tunnel tests other experimental methods, or literature results.

1.3 Aeroelastic Wind Effects on Bridges

Aeroelasticity is a multidisciplinary field that brings together aerodynamics, structural dynamics, and mechanical engineering. In the field of forces, it is the science that studies the interaction between the elastic, inertial, and aeroelastic force fields acting on a structure. Aeroelasticity is a very complex field that can include other factors such as thermal effects, which complicate its study even more. This macro discipline can be divided into two areas: static aeroelasticity and dynamic aeroelasticity [8]. The former deals with the interaction between elastic and aerodynamic forces, while dynamic aeroelasticity adds inertial forces and non-linear effects to the analysis.

Bridges are structures strongly affected by aeroelastic effects due to their slender and elongated geometry and the fact that they are immersed in highly dynamic flow fields. The most common aeroelastic effects on bridges are flutter, galloping, divergence, and buffeting.

1.3.1 Flutter

Flutter is an aeroelastic phenomenon of dynamic instability resulting from the interaction of elastic, inertial, and self-excited aerodynamic forces [9] and is one of the most critical phenomena for slender structures. What happens when the critical wind speed is reached is that the structure begins to oscillate in a divergent manner until it fails. These vibrations typically manifest as torsional or vertical oscillations. The critical speed of the corresponding wind is called the flutter speed, which causes divergent oscillations in the structure, with the same frequency and theoretically increasing amplitude tending towards an infinite value[10]. In practice, these oscillations are stabilized around a maximum amplitude value. During the divergence process, the structure can suffer various types of damage at key points, leading to failure after a few cycles of flutter[9]. Flutter is a phenomenon that has been widely studied in the aerospace field and became of critical importance after the catastrophic collapse of the Tacoma Narrows Bridge in 1940. The ultimate goal of flutter verification is to determine the minimum speed at which this phenomenon is triggered; lower or higher speeds will not cause the structure to vibrate divergently.

1.3.2 Galloping

Galloping is a type of dynamic aeroelastic instability, often referred to as a vortex-induced vibration (VIV) phenomenon, which particularly affects large and thin baffle decks. It can lead to structural instability, fatigue damage, and potentially catastrophic failure. This type of phenomenon generally occurs when wind-generated eddies detach from the deck surface, creating alternating eddies typical of the Kármán vortex phenomenon. The latter generally occurs at relatively normal wind speeds [11], underlining the importance of studying this phenomenon for structures such as bridges.

The motion consists of an oscillation perpendicular to the direction of flow, it is a kind of self-sufficient phenomenon, i.e. once the oscillation phenomenon starts, the lift increases, which further increases its amplitude. This effect, also known as the feedback effect, is due to the fact that all mechanical and aerodynamic damping is completely eliminated[9].

It is possible to distinguish two different types of galloping on a slender structure. The so-called hard-galloping has a higher amplitude, the swaying is more structured and intense and it is also predictable. This type of galloping is quite dangerous for the structure, leading to the collapse of the structure. Soft-galloping is more unpredictable, the swaying is more gentle, and the oscillation is not constant, but it is still dangerous for the structure and can lead to fatigue damage over time.

1.3.3 Torsional Divergence

Torsional Aeroelastic Divergence (ATD) is a dynamic phenomenon consisting of a torsional movement out of the plane of the deck. The definition of ATD is very complex as it is a set of deformations and rotations that the bridge deck undergoes at a critical wind speed. At this critical wind speed, there is an unlimited growth of the structural rotation [14], this theoretical definition is unrealistic in the field of bridge design and therefore it is more reasonable to define the critical divergence of the wind speed as that at which the torsion of a body increases rapidly up to the breaking point [13]. What happens in practice is that the wind flow not only generates aerodynamic forces but also a moment in the structure. If the wind speed is equal to the critical speed, the moment generated by the flow is equal to that associated with a torsional mode of the structure. The moment due to the flow increases the torsional angle, inducing an out-of-plane torsional divergence, there is also a second out-of-plane deformation due to a drag force. The effect of the divergence is always of the combined type, lateral (vertical) instability, and torsional divergence [9]. The vertical movement causes a deterioration of the torsional stiffness, this aspect is characteristic of the torsional divergence [12]. This aeroelastic effect is also very common in bridges with long, flexible, and slender spans.

1.3.4 Buffeting

Buffeting is an aeroelastic phenomenon that can have significant effects on very long-span bridges. Length and flexibility play a key role in amplifying the buffeting effect. Unlike the other effects described so far, this one is characterized by high-frequency oscillations that are always due to turbulence effects, in particular the separation of these eddies that occurs when the flow meets the surface of the body through which it passes. This effect is nothing more than the result of the resonance that occurs for mode shapes at very high frequencies. All aeroelastic phenomena are caused by turbulent winds interacting with the bridge structure. The vibrations are very fast due to the high frequency of the bridge or parts of it. The effect of high-intensity turbulence can lead to slamming, which can severely damage the structure or key components of the structure, leading to complete failure.

All these dynamic aeroelastic effects become significant when the bridge is slender, thin, and highly flexible, even long spans are to be avoided, especially when the wind conditions of the geographical position of the bridge vary over a very wide range. Such structures are certainly more pleasing to the eye and require less material, but if they have not been thoroughly checked from an aeroelastic point of view, they may be subject to damage or, in the worst case, catastrophic failure.

1.4 Wind Design Standards

The Wind Load Standards are guidelines that summarise the essential concepts and checks to be carried out in the design of structures exposed to wind loads. The aim is to guide the designer in the design of a structure that will ensure its safety and structural integrity. The choice of the appropriate standard to follow depends on the geographical location of the project, there are local, national, and international regulations that provide guidelines based on the specific type of structure to be designed. In Europe, the design of buildings and civil structures is governed by the Eurocode, which is divided into different sections, each with a specific purpose. In particular, Eurocode SS-EN 1991-1-4:2005 focuses on the effects of wind on structures and is accompanied by national guidelines, which must always comply with the main European standard but take into account the specificities of the geographic location. The Eurocode provides several detailed procedures for calculating wind loads and their effects on different types of structures, including bridges. Some of these are analyzed in this section.

1.4.1 Wind Velocity

Wind speed is the first parameter to be determined, a fundamental parameter in the calculation of wind loads according to the Eurocode standards. The process involves several stages, including the determination of the basic wind speed, and the consideration of various coefficients depending on altitude and terrain category, all of which should lead to the calculation of the mean wind speed. This is a representative value of the wind speed to be taken into account when calculating the wind load.

Basic Wind Velocity (V_b) The basic wind velocity, denoted as V_b, represents the 10-minute mean wind velocity at a height of 10 meters above ground level, considering a geographic zone without obstacles.

$$V_b = c_s \cdot c_r \cdot V_{b0} \tag{1.6}$$

Where: c_s is the season factor, c_r is the wind directional factor, V_{b0} is the fundamental value of the basic wind velocity. The values of c_s and c_r are provided in the National Annex depending on the site-specific conditions, their conservative value is equal to the unitary value.

Mean Wind Velocity (V_m) The mean wind velocity (V_m) is the 10-minute mean wind velocity at the height of the structural design point. Eurocode offers a formula to calculate V_m:

$$V_m = c_r(z) \cdot c_0(z) \cdot V_{b0} \tag{1.7}$$

Where: $c_r(z)$ is the roughness factor, accounts for the variability of the mean wind velocity at the site of the structure, and depends on the roughness length and terrain factor, all coefficients given by the Eurocode. c_0 is the orography factor, given by the National Annex, its conservative value is the unitary value.
Each of these factors is determined based on site-specific conditions and the height (z) of the structure.

1.4.2 Vortex Shedding and Aerodynamic Instability

Vortex shedding is one of the most important phenomena to be studied in structures exposed to wind. The concept of vortex shedding has been extensively explained previously, it is an aerodynamic effect of the turbulence trail created behind the object crossed by the flow: the alternating eddies are released from opposite sides of the structure when generating fluctuating forces perpendicular to the wind direction, resulting in structural vibrations. In cases where the vortex shedding frequency matches the natural frequency of the structure, aerodynamic instability can occur as the structure goes into resonance.

Critical Wind Velocity (V_{cr}) The critical wind velocity (V_{cr}) is the wind speed at which vortex shedding is most likely to induce aerodynamic instability. It is a vital parameter in assessing the structural response to wind loads. Eurocode defines V_{cr} based on factors like the structure's geometry and natural frequency.

$$V_{\mathrm{crit,i}} = \frac{d \cdot f_{\mathrm{n}}}{S_t} \tag{1.8}$$

Where: d is the characteristic width of the cross-section, f_{n} is the natural frequency of the structure for the considering i flexural mode, and S_t is the Strouhal number, given in the EurocodeS based on the ratio between the two dimensions of the cross-section, Figure 1.5.

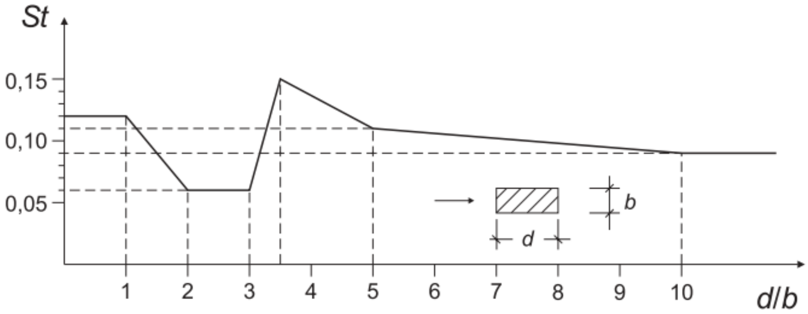

Figure 1.5: Strouhal number for rectangular cross-sections with sharp corners, Eurocode 4,E1, [1].

The Eurocode sets a limit value above which the effects of vortex shedding must be studied. If the critical wind speed for each mode of the structure is less than or equal to 1.25 times the characteristic mean wind speed over 10 minutes, vortex shedding cannot be neglected and must be analyzed. The formula used by the Eurocode is given by equation 1.9.

$$V_{crit,i} > 1.25 \cdot V_m \tag{1.9}$$

Vortex shedding load : the vibration caused by vortex shedding induces an inertial action $F_w(s)$ 1.10, which is described by the Eurocode. The guide gives precise instructions on the direction of the force to be applied perpendicular to the wind direction, along the lift direction.

$$F_W(s) = m(s) \cdot (2 \cdot \pi \cdot f_{i,y})^2 \cdot \phi(s) \cdot y_{F,max} \tag{1.10}$$

Where $m(s)$ represents the vibrating mass per unit length of the structure under analysis, $f_{i,y}$ denotes the i-th frequency of the mode shape being investigated, and $\phi(s)$ corresponds to the mode shape of the structure, normalized to a value of 1 at the position of maximum displacement.$y_{F,max}$ is the maximum displacement related to $\phi(s)$.
One of the approaches given by the Eurocode consists of calculating the maximum displacement following the equation 1.11:

$$y_{F,max} = \frac{d \cdot K \cdot K_W \cdot C_{lat,0}}{S_t^2 \cdot S_c} \tag{1.11}$$

Where: d is the characteristic length of the section, K is the mode shape factor, K_w is the effective correlation number its evaluation depends on the mode shape configuration.$C_{lat,0}$ is the lateral coefficient equal to 1.1 for a rectangular section. S_t is the Strouhal number and S_c is the Scruton number given by the equation 1.12.

$$S_c = \frac{2 \cdot \delta_s \cdot m_{i,e}}{\rho \cdot d^2} \tag{1.12}$$

Where δ_s is the structural damping, $m_{i,e}$ is the equivalent mass for the i-th mode shape. ρ is the air density and d is the characteristic length.

When all these parameters are defined, the inertial force applies along a specific length of the beam structure at a position determined by the i-th mode shape configuration. The Eurocode gives a specific indication of this length.

Chapter 2

Case study: Bomarsund Bridge

2.1 Introduction

The Bomarsund Bridge 2.1, is a newly constructed bridge, located in the connection between Bomarsund and the island of Prästö in the municipality of Sund, in Ålan 2.2. The island is located in a geographical position between Finland and Sweden, an area affected by strong gusts of wind. It is a mainly steel structure rebuilt and designed by the Swedish company WSP. Its construction was completed in the middle of 2023. This bridge has attracted a lot of attention, particularly for the interesting structural and dynamic challenges it poses, such as high vibrations in the arch hungers, especially the longer ones located in the middle span of the bridge. These excessive vibrations are of critical importance due to their potential to induce structural fatigue problems, especially in the attachment part, and consequently threaten the overall integrity of the bridge. Recognizing the importance of the Bomarsund Bridge in the context of wind engineering, this case study examines the correlation between the fluid dynamics and the high vibrations in the arch hangers and the potential consequences of these vibrations on the overall structural health. This bridge is a very interesting case study, and its monitoring by sensors and strain gauges could provide data of great importance for the design of future more resilient and durable bridges in extreme wind conditions such as those experienced by this bridge.

2.2 The Bridges Evolution

The history of the Bomarsund Bridge is a very interesting story, which has been reconstructed in detail in the article: 'Lageralksro över Bomarsund på Åland' in the magazine Stålbyggnad. The Bomarsund Bridge is an important part of Åland's history, a place of historical significance, and a key element in the region's transport network. The original

Figure 2.1: New constructed Bomarsund Bridge, adapted from "Lageralksro över Bomarsund på Åland", Stålbyggnad

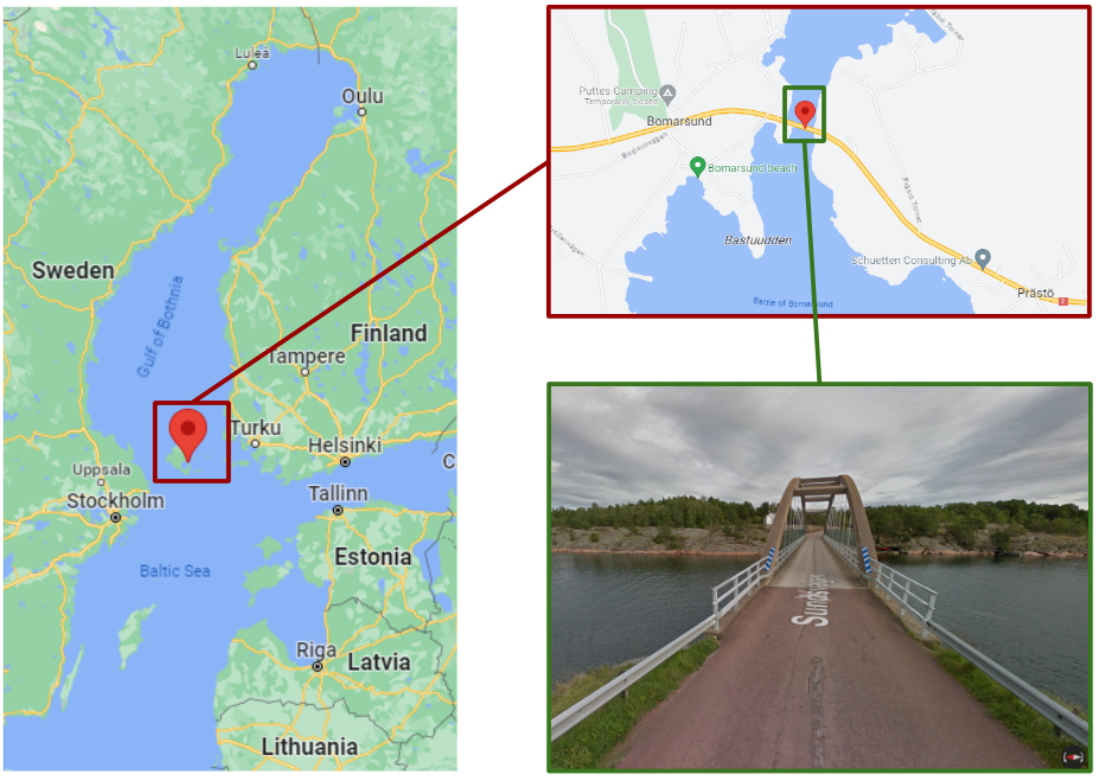

Figure 2.2: Goole maps location of the Bomarsund Bridge.

Bomarsund Bridge was a classic concrete arch bridge with a steel-reinforced deck, a typical engineering design of the time. However, it was decided to completely replace the bridge as it was not designed to withstand today's traffic loads, resulting in durability issues. It had extensive damage at some key points in the structure. In addition, the previous bridge had only one lane, a common feature of Åland bridges, which caused traffic problems, especially during maintenance and resurfacing work. These were the main reasons why the Åland government decided to replace the bridge. In selecting the design for the new bridge, WSP's structural engineers were tasked with finding a solution that could overcome the potential challenges posed by the underlying rock formations as well as the strong gusts of wind characteristic of the bridge's geographical location.

2.3 The Bridges Design

For the new design of the Bomarsund Bridge, WSP engineers chose a Langer beam arch bridge, a massive and harmonious structure. The decision to use this type of arch bridge was dictated by the conditions of the rocky subsoil: it was feared that the rock under the bridge location would not be able to support a classic arch bridge. In contrast to the classic arch, which is anchored directly in the rock, a system of cables is used both inside the arch and between the two arches of the bridge. This solution allows the horizontal loads from wind and traffic to be distributed more efficiently.

The specifications of the new Bomarsund Bridge are impressive, with a span of 70.4 meters and a total length of 80.8 meters. The height of the arch from the roadway is just over 12 meters, the longest inclined tie rod is over 11 meters and the distance between the arches is 13 meters. The two arches of the bridge are stabilized at the top by a K-shaped truss of square cylinders. The bridge has been designed to accommodate different types of traffic, with two lanes for vehicular traffic plus pedestrian and cycle paths, reaching a clear width of 9.55 meters.

The designer of the bridge, Lars Erik Lundenberg, has optimized the design of the bridge to the maximum, not only trying to find an efficient solution from a mechanical and aesthetic point of view but also paying particular attention to adopting design solutions that, in addition to mechanical efficiency and aesthetic harmony, allow optimization in the use of materials. His innovative solution was to use diagonal hangers made of hollow square tubes instead of vertical ones, saving around 200 tonnes of steel in the structure.

Special attention was paid to the realization of the structure, which was manufactured by Nordec in Ylivieska using steel from SSAB in Raahe. The steel components were delivered to the site in 17-meter units and fully painted, which reduced the amount of work required at the site. Welding on site was necessary, but was mainly imitated for the less complex parts to minimize the margin for error and have more control over the construction of the structure. The Bomarsund Bridge is a testament to the fusion of history and innovation, combining the historical heritage of the Bomarsund Fortress with modern engineering solutions to create an efficient and harmonious structure that supports the needs of today's society.

2.4 Bridge Geometry

The geometry of the bridge is very complex, consisting of two arches thickened by a grid of inclined hangers, connected horizontally in the upper part by a bracing system of hollow square tubes. The deck is cast in concrete in static interaction with the grid of steel beams.

The case study focuses more on the hangers and the arch parts connected to them.
The arch is constructed with a hollow beam of a particular shape, as shown in Fig: 2.3, with stiffeners on the inside corresponding to the attachment of the hangers. The elements of the arch section are all welded.
The hangers have a hollow square section, the section is cut by two inclined planes to form a triangular closure by the attacks, as shown in figure 2.5.
The beam at the base of the arch is an IPE beam with plates welded to the top flange at the hanger connection, fig 2.4.

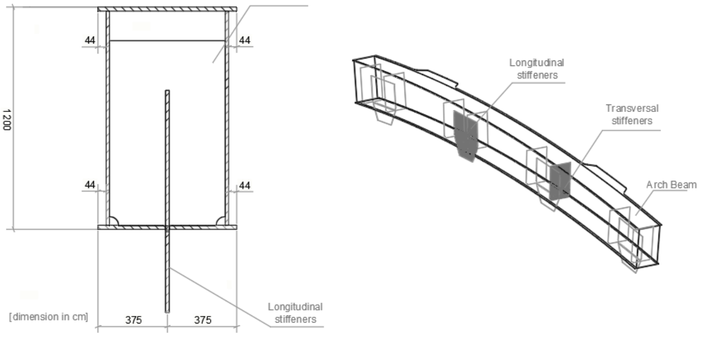

Figure 2.3: Beam profile for the arch element and 3D view of the beam.

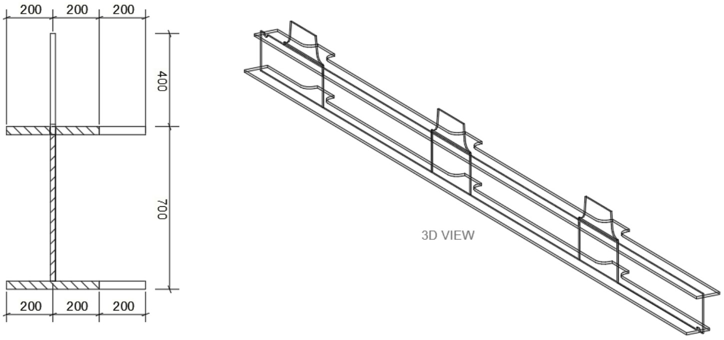

Figure 2.4: Ipe beam and 3D view.

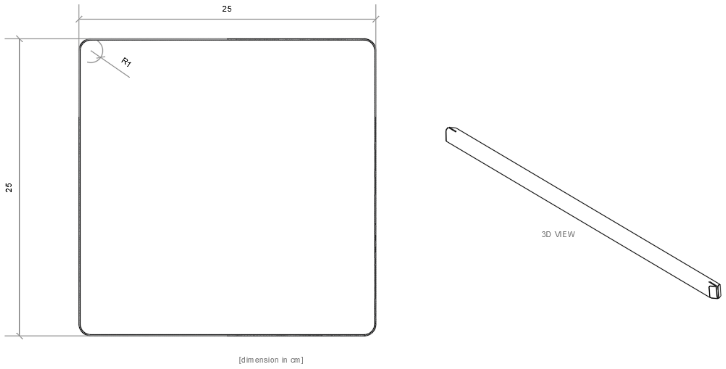

Figure 2.5: Hanger cross-section and 3D view.

Chapter 3

Numerical Analysis of Hangers in the Bridge Structure

3.1 Introduction

Bridges are subject to various environmental loads, including wind forces and the associated vortices they can generate. These aerodynamic flows can induce vibrations and compromise structural integrity by causing fatigue damage for example. This type of load can be more compromising than static loads, understanding and modeling these dynamic loads is of crucial importance in order to better analyze the behavior of the structure and achieve an accurate design. This chapter will present finite element modeling and analysis of hangers using Abaqus software, with the objective of defining natural frequencies and mode shapes to verify wind load calculations, incorporating the effect of vortex shedding in accordance with Eurocode standards.

The objective of this chapter is to define natural frequencies and mode shapes, which play a crucial role in the calculation of wind-induced forces. By accurately capturing these dynamic characteristics, one can improve the reliability of wind load evaluations and ensure a range of reliability related to the structural calculations performed.

To achieve the goal of the analysis, a progressive modeling approach was adopted, starting first with a single hanger and gradually increasing complexity by incorporating additional hangers. A total of five models were developed and analyzed, each representing a different configuration of Nielsen hangers attached to the hollow box arch and the tying IPE chord.

In the upcoming parts of this chapter, finer aspects of each model will be explored, detailing the modeling techniques used and analyzing the results obtained.

3.2 Methodology

In this section, a detailed description of the progressive modeling approach is provided by dictating the various models composed of Nielsen hangers, the hollow box arch, and the connecting IPE chord. In particular, the geometry, dimensions, and material properties of the bridge components used to model the structure on the finite element software Abaqus are presented.

The analysis was carried by focusing on the arch at the south side, from this one a total of five sub-models were analyzed. The first model focused on a single hanger, specifically H16, connected to the arch and IPE beam. A frequency analysis was conducted to determine the first ten natural frequencies and corresponding mode shapes of the hanger. These results served as the basis for further investigation and validation against Eurocode requirements. Subsequent models were then developed, gradually introducing additional hungers to simulate real-world scenarios. Model 2 incorporated hangers H15 and H16, while model 3 included hangers H14, H15 and H16. By gradually increasing the number of hangers, until reaching the actual model of eight hangers, from H12 to H19, 3.1.

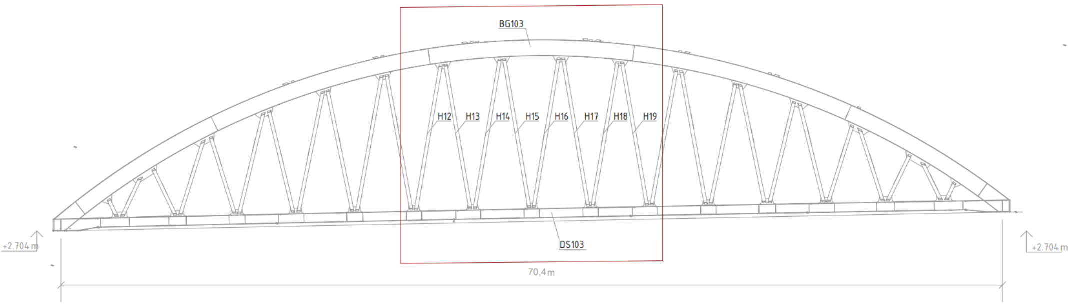

Figure 3.1: Bomarsund Bridge: south side arch .

3.2.1 Geometric Modeling

In order to accurately represent the hangers, the hollow box arch, and the tying IPE chord, a geometric model was created consisting of several shell elements. This approach allows the structural behavior to be captured while minimizing calculation costs, and shell elements were chosen for their ability to effectively represent thin-walled structures, given their small thicknesses, and also allow to describe accurately intersecting shells that exhibit non-linear behavior.

The geometric model was developed based on the design drawings and specifications of the Bomarsund Bridge. Great care was taken to accurately reproduce the dimensions, cross profiles, and connection details of the hangers to the gussets, arch with stiffening plates, and the IPE chord. The model took into account the unique geometry and interaction between the different components of the bridge structure.

3.2.2 Material Proprieties

To ensure reliable results from the frequency analysis performed on the various models, it is essential to accurately represent the behavior of the materials used in the structure. The material properties have been carefully defined based on the specific characteristics and specifications of the material used in the construction.

For consistency and simplicity, the same set of material properties has been assigned to all components. These properties include an elastic modulus (E) of 210 GPa, a Poisson's ratio (ν) of 0.3, and a density of 7850 kg/m^3. These properties reflect the specific characteristics of the materials used and are essential for obtaining accurate and meaningful results from the analysis.

3.2.3 Mesh Modeling

In order to discretize the geometric finite element model, an appropriate meshing strategy was used to accurately represent the complex geometry and capture the structural behavior of the hangers, the hollow box arch, and the binding IPE cord. Considering the unique features of the structure, such as curved elements, sharp edges, and intersections between shells, a meshing strategy using quadratic-dominated elements with a free technique and a median axis-based algorithm was employed. Quadratic-dominated elements were selected for meshing because of their ability to capture finer details of the structural response than linear elements. These elements have higher-order shape characteristics, allowing a more accurate representation of curved geometries. The free technique, also known as free mesh or unstructured mesh, provides the flexibility to create irregular, non-uniform meshes that closely match the geometry. It allows for better resolution of regions with complex features, particularly in the junction area, including various gussets, hangers, and stiffeners. The median axis-based algorithm helps maintain mesh quality by ensuring proper element connectivity, reducing element distortion, and improving overall analysis accuracy. It is particularly beneficial when dealing with complex geometries such as those present in the bridge structure in question.

Particular attention has been given to regions of interest, such as attachment points, and local mesh refinement techniques have been applied to these areas to ensure adequate mesh density and to accurately capture the fine details of the dynamic response. Mesh sizes of 0.02m and 0.025m were chosen to provide the best possible finish, taking into account the maximum number of nodes allowed in Abaqus.

3.2.4 Boundary Conditions

For each of the five models analyzed, a specific section of the arch and IPE beam was considered. To ensure a realistic representation of the structure, fixed boundary conditions were applied to the section. These fixed boundary conditions mimic the connections that would exist in the real bridge, providing stability and constraining the movement of the modeled components.

It is important to note that for the last model, H12-19, an additional consideration was made due to the considerable length of the IPE beam. As the main interest was to study the frequencies of the hangers rather than the motion of the beam itself, it was observed that the frequencies obtained from the analysis were influenced by the motion of the IPE beam rather than the hangers. To address this issue, the effect of the real existing crossbeams welded to the top flange of the IPE beam, which constrained the out-of-plane motion of the IPE beam, was simulated. Additional constraints were implemented to prevent out-of-plane motion of the IPE beam and to focus the analysis on accurately extracting the hanger frequencies.

By applying appropriate boundary conditions, including fixed boundary conditions and additional constraints where necessary, the dynamic response of the Hanger bridge system can be accurately captured and analyzed.

3.2.5 Analysis Setup

The aim of this part of the study was to perform a frequency analysis, also known as an eigenvalue analysis, to identify the dominant vibration modes and provide information on the structural behavior under dynamic loadings, such as wind action.

The frequency analysis was performed using Abaqus software with specific settings tailored to ensure accurate results. The analysis considered the non-linear geometry of the structure, taking into account any geometric non-linearity that could affect the dynamic response. The eigensolver chosen was the Lanczos algorithm, a widely used and efficient method for solving eigenvalue problems in frequency analysis.

A set of 10 eigenvalues was calculated to capture the relevant modes and provide meaningful results. In addition, the eigenvectors representing the mode shapes of the structure were normalized by displacement to ensure a consistent magnitude of displacements and a better representation of the structural response. By using these specific frequency analysis capabilities, the study aimed to accurately determine the natural frequencies and mode shapes of the hangers, providing their dynamic characteristics and their interaction with the overall bridge structure.

3.3 Results Analysis

The analysis focused on examining the frequencies obtained from frequency analysis for each of the five models. The natural frequencies provide valuable insight into the dynamic behavior of the hangers and their interaction with the bridge structure. The frequencies were extracted and presented in a tabular format, highlighting the important characteristics of each model.
For clarity in the presentation of the results, only the first two frequencies and mode shapes are reported in this chapter. For the complete results, please refer to Annex A.

3.3.1 Model H16

Model H16 represents a single hanger, specifically the 16th hanger, which has a length of 11.32 m and is inclined at an angle of 10 degrees with respect to the vertical axis. The arch and the IPE beam are sectioned by two vertical planes located 4.7 m apart.

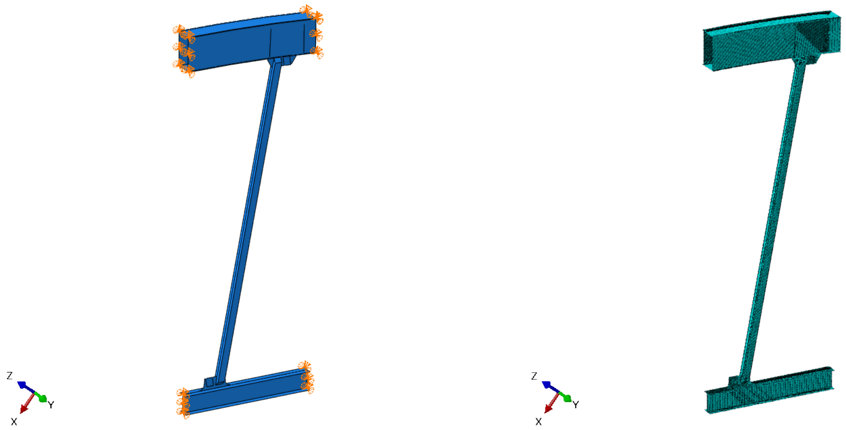

(a) BC (b) Mesh

Figure 3.2: Model H16 Configuration

To accurately simulate the behavior of Model H16, fixed boundary conditions were applied at the cut sections on the arch and the IPE beam, as shown in Figure3.2a. These fixed boundary conditions restrict the movement of the structure at those points and provide a realistic representation of the actual bridge system.

Table 3.1: Model H16: First two frequencies

H16			
MODE	EIGENVALUE	FREQUENCY (Hz)	OSCILLATION
1	1733.1	6.6257	out of plane
2	7798.2	14.055	in plane

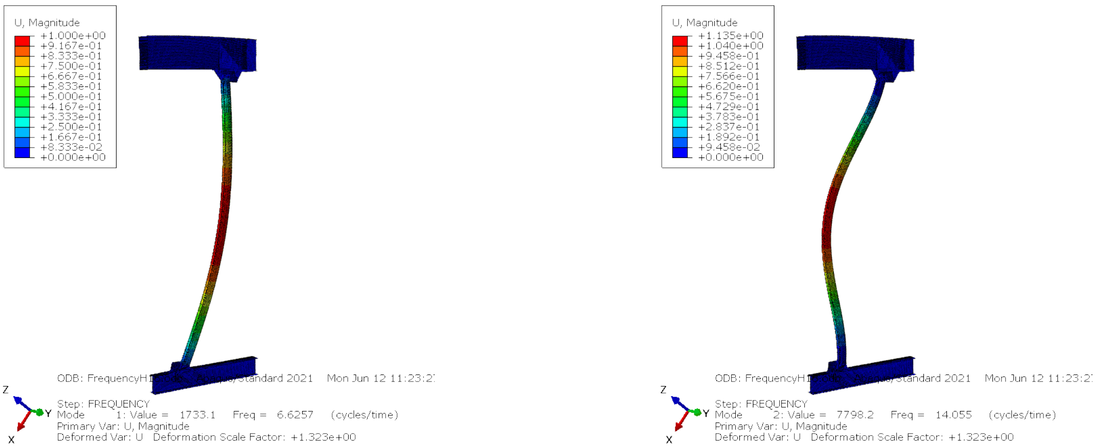

(a) 1^{st} mode shape

(b) 2^{nd} mode shape

Figure 3.3: First two mode shape model H16

Comments The mode shapes obtained from the frequency analysis provide insights into the dynamic behavior of Model H16. It is observed that for the first five mode shapes, see Table A.1, only the hanger exhibits significant motion, while the arch and the IPE beam remain relatively static. This indicates that the lowest natural frequencies primarily correspond to the vibration of the hanger itself.

However, from the 5th to the 10th mode shapes, Table A.1, higher frequencies are observed, and it can be seen that both the arch and the IPE beam contribute to the overall motion. Although these higher modes involve the coupled vibration of multiple components, it is important to note that for this analysis, the focus is on capturing the lowest natural frequencies of the hanger. In this context, the model can be considered acceptable since the first few modes predominantly represent the behavior of the hanger itself.

3.3.2 Model H15-16

The H15-16 model consists of two hangers, H15 and H16, connected to part of the arch and the IPE beam at the base. The geometric model is constructed by accurately representing the shape, dimensions, and positioning of the hangers. The arch and the IPE beam are sectioned by two vertical planes which define the boundaries of the model.

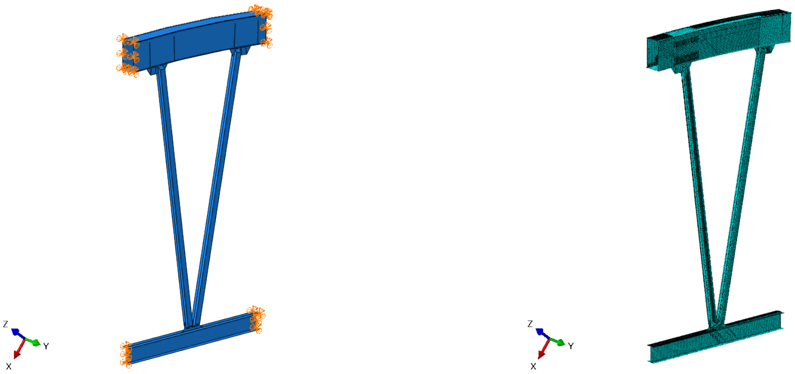

(a) BC (b) Mesh

Figure 3.4: Model H15-16 Configuration

Table 3.2: Model H15-16: First two Frequencies

H15-16			
MODE	EIGENVALUE	FREQUENCY	OSCILLATION
1	1635.2	6.4359	out of plane
2	2203.2	7.4705	in plane

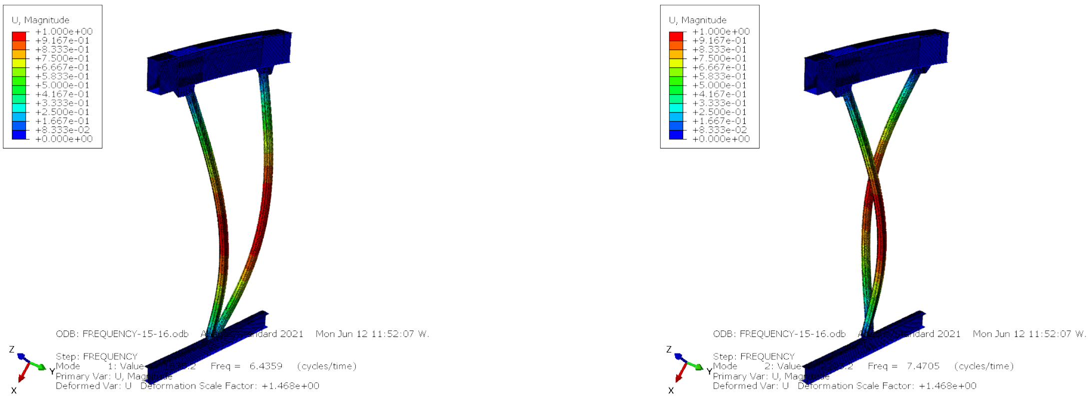

(a) 1^{st} mode shape (b) 2^{nd} mode shape

Figure 3.5: Mode shapes model H15-16

Comments: By incorporating a second hanger into the model, there was a noticeable alteration in the dynamic response of the structure. While the first natural frequency remained consistent with the previous model, the second natural frequency was almost half of the previous discovery. And the third natural frequency has a value around 14 Hz, see Table A.2. This can be attributed to the interaction and coupling effects between the two hangers. The coupling effects impact the system's dynamic behavior, causing changes to the natural frequencies of each component and its mode shape. The addition of a second hanger changes the distribution of masses and stiffness, further influencing mode shapes and associated frequencies. Additionally, the boundary conditions of the single hangers also change due to the inclusion of a lateral element. Therefore, it is justifiable to regard the obtained results as satisfactory, and the model as an accurate representation of the structure. The table A.2 and figure A.2i respectively exhibit the ten frequencies and their accompanying mode shapes.

3.3.3 Model H14-16

Model H14-16 extends the analysis by including an additional hanger, H14, along with H15 and H16. The geometric model is an extension of the previous model, H15-16, and includes the additional hanger, H14. The dimensions and positions of H14, H15, and H16 are accurately represented, together with the arch and the IPE beam. The hangers are slender elements inclined at specific angles to the vertical axis.

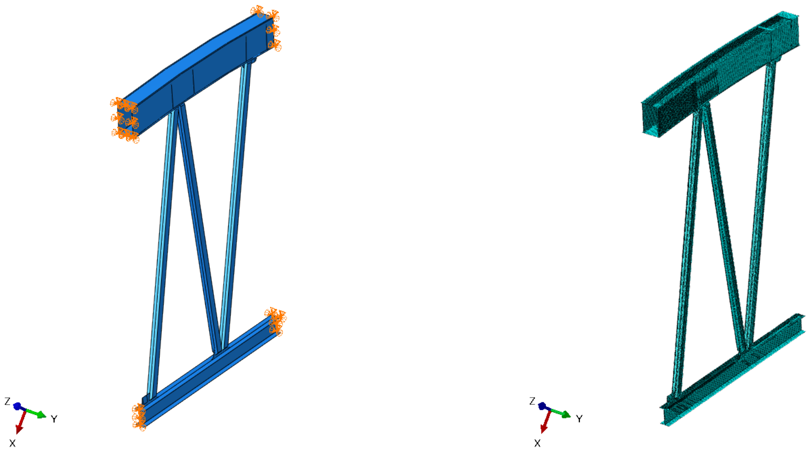

(a) BC

(b) Mesh

Figure 3.6: Model H14-16 Configuration

Table 3.3: Model H14-16: First two Frequencies

H14-16		
MODE	EIGENVALUE	FREQUENCY
1	1598.40	6.36
2	1890.00	6.92

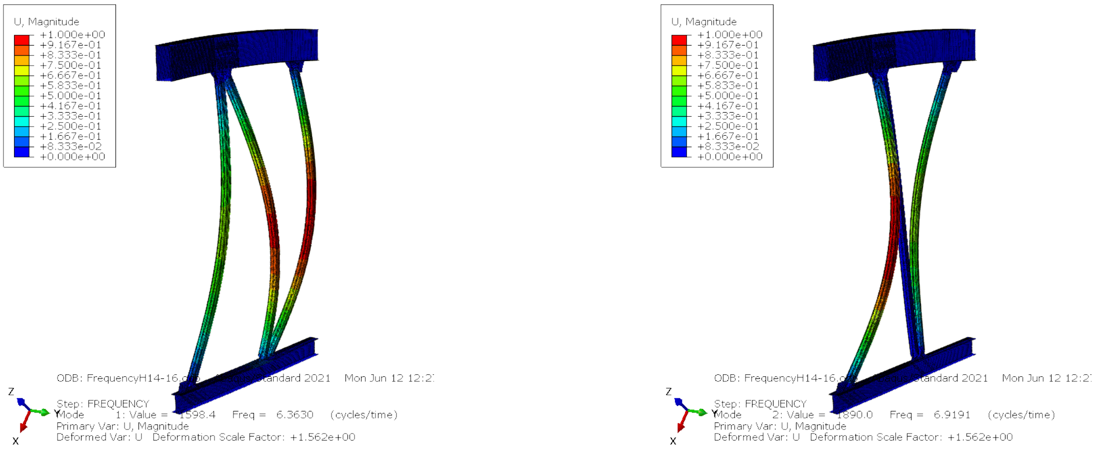

(a) 1^{st} mode shape (b) 2^{nd} mode shape

Figure 3.7: Mode shapes model H14-16

Comments: The interaction observed in the previous model, due to coupling, interaction, and different mass distribution and stiffness, is applicable to the current model as well. The three hangers interact with each other, altering their dynamic behavior, including natural frequency and mode shape configuration. By including the third hanger, the dynamic behavior of the entire system is completely altered. Hanger H16 does not contribute to the second frequency of the model, and the type of oscillation for the overall system cannot be defined since one hanger can have an out-of-plane oscillation while the adjacent hanger can have an in-plane oscillation or not contribute at all. However, upon observation of the central hanger H16, its first and second oscillations are around 6Hz and 14Hz respectively. This information can be found in the table A.3 and figure A.3j.

3.3.4 Model H14-17

The geometric model for H14-17 is an extension of the previous models, including the additional hanger, H17. The dimensions and positions of the hangers are accurately represented, along with the arch and the IPE beam. The hangers are modeled as slender elements with specific inclinations relative to the vertical axis.

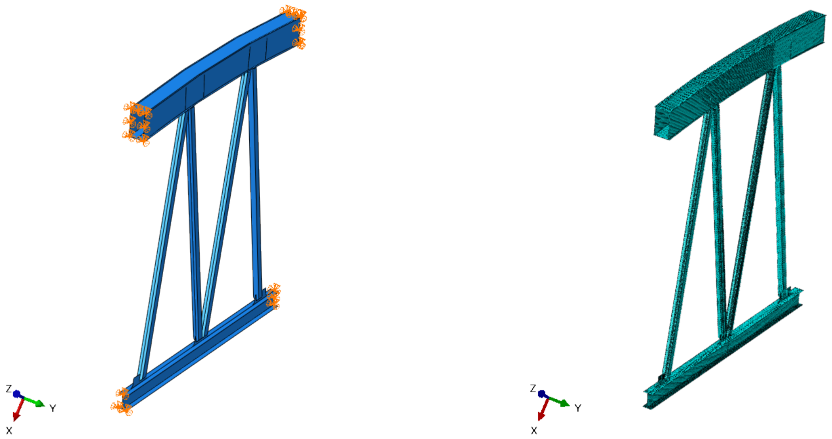

(a) BC (b) Mesh

Figure 3.8: Model H14-17 Configuration

Table 3.4: Model H14-17: First two Frequencies

H14-17		
MODE	EIGENVALUE	FREQUENCY
1	1476.60	6.12
2	1823.50	6.80

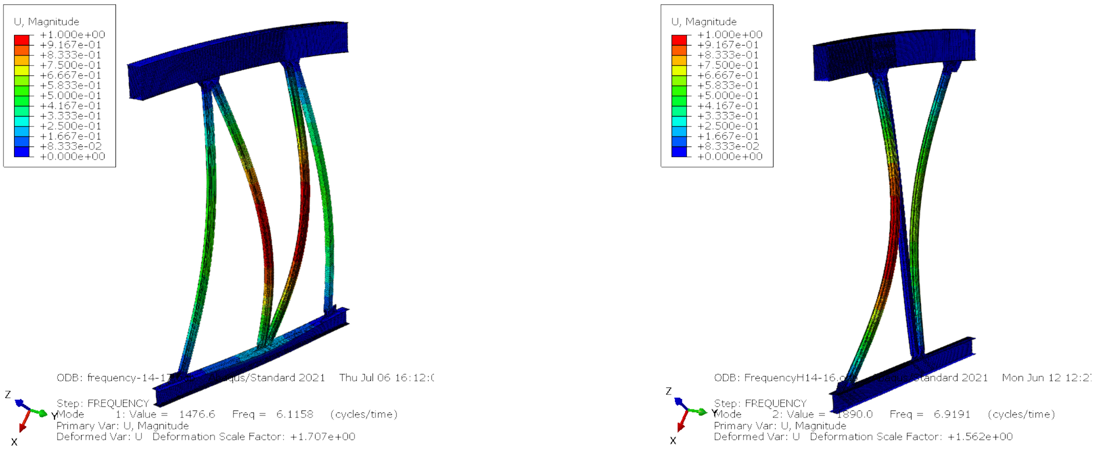

(a) 1^{st} mode shape (b) 2^{nd} mode shape

Figure 3.9: Mode shapes model H14-17.

Comments: The same observation made for model H14-16 can be applied to this model when an additional hanger is added. Focusing on the behavior of the H16 hanger, it is observed that it contributes to the first natural frequency with a magnitude of 6.12

Hz; this value is slightly lower compared to the previously found values. Furthermore, it does not contribute to the second natural frequency of the model. From the third mode shape, a slight motion can be observed. In the sixth mode shape, it is the principal contributor with a natural frequency of almost 14 Hz. See the Table A.4 and the figure A.3i where all the 10 frequencies and mode shapes of this model are organized.

3.3.5 Model H12-19

Model H12-19 consists of eight hangers (H12 to H19) connected to a portion of the arch and the IPE beam. The length of the hangers varies, and they are inclined at different angles with respect to the vertical. The arch and the IPE beam are sectioned by two vertical planes, 21.5 m apart. Fixed boundary conditions are applied at the cut sections on the arch and the beam, as shown in Figure3.10a.

It is important to note that for Model H12-19, the last model in the series, the length of the IPE beam is significant, and it was observed that the frequencies obtained from the analysis were influenced by the motion of the IPE beam rather than the hangers alone. To isolate the frequencies related to the hangers and accurately capture their behavior, a modification was made to the boundary conditions. Additional constraints were applied to simulate a cross beam that constrains the out-of-plane motion of the IPE beam, thus preventing its contribution to the extracted frequencies. This modification allows for a focused analysis of the hanger frequencies and provides more accurate results.

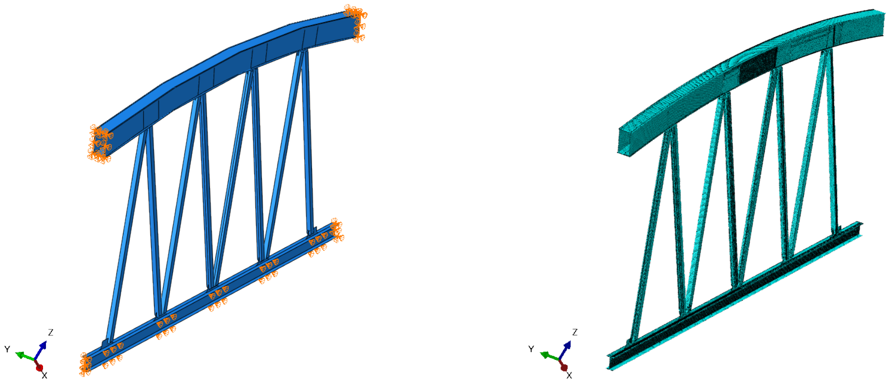

(a) BC

(b) Mesh

Figure 3.10: Model H12-19 Configuration

Table 3.5: Model H12-19: First two Frequencies

H16		
MODE	EIGENVALUE	FREQUENCY
1	1578.7	6.3236
2	1814.3	6.7791

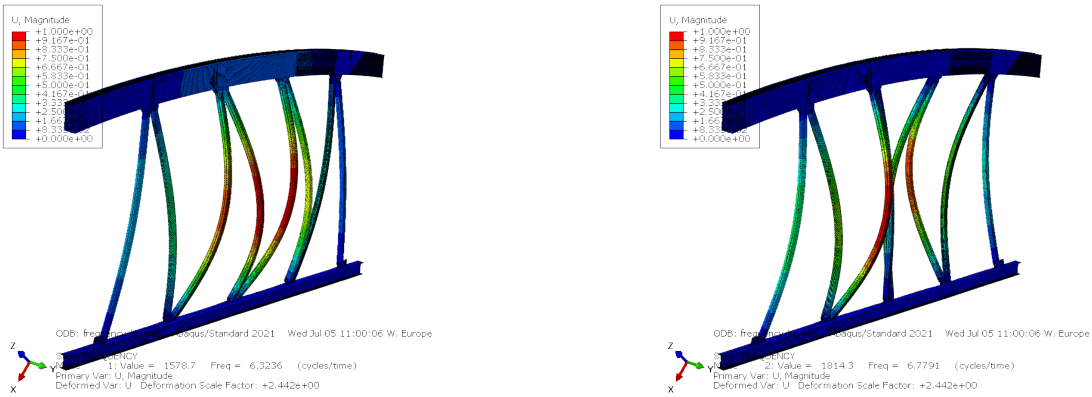

(a) 1^{st} mode shape (b) 2^{nd} mode shape

Figure 3.11: Mode shapes model H12-19.

Comments The mode shapes displayed in Figure A.5i, which were obtained for Model H12-19, demonstrate the vibration patterns linked to every natural frequency. Although the hangers are the main components in motion, the arch and the IPE beam's participation can be noticed at higher frequencies. Identifying the primary contributor to the i-th mode shape becomes intricate for this model. Overall, the range of frequencies, see Table A.5, is still reasonable and aligns with the previous models by applying the modified boundary condition.

3.4 Result Discussion

The examination of different models of bridge hangers yields useful insights into their dynamic behavior and their interaction with the overall structure of the bridge. By analyzing the natural frequencies of these models, intricate relationships influenced by a number of factors such as the quantity and shape of the hangers, become apparent.

For example, in the case of a single hanger, Model H16, the first five modes of vibration predominantly exhibit motion within the hanger itself. Exhbiting a first natural frequency of 6.6 Hz, and a second natural frequency of 14 Hz. As more hangers are introduced, Models H15-16, H14-16, and H14-17, the dynamic response changes noticeably. The interaction and coupling effects between hangers become apparent, and the change of mass and stiffness has a significant effect on the variations of natural frequencies and mode shape configuration.

Adding a third hanger, Model H14-16, transforms the system's dynamic behavior further, where all three hangers interact and influence each other. This trend persists with the inclusion of all the hangers used for the models. In multi-hanger configurations, each hanger's position affects the structure's natural frequencies, with variations in contribution across different modes.

The H12-19 model, the most intricate, contains eight hangers, and constraints are added to isolate hanger-related frequencies and reduce the impact of the IPE beam's length on results. The detailed vibration patterns present in the mode shapes demonstrate the intricate interplay among the hangers, arch, and IPE beam.

In conclusion, the analysis emphasizes that the quantity and positioning of hangers have a considerable effect on the dynamic response of the bridge structure. With an increase in hangers, the interaction and coupling effects become more pronounced, resulting in variations in natural frequencies and mode shapes. The key finding of this study is the range of critical frequencies for the hangers, which oscillate between 6 and 14 Hz. Such a range of frequencies can be employed for forthcoming analyses, aiding the evaluation of the bridge's dynamic behavior.

Chapter 4

Ansys Fluent: 2D & 3D CFD analysis

4.1 Introduction

Ansys Fluent is a widely used computational fluid dynamics (CFD) software that allows for the simulation and analysis of fluid flow and aerodynamic behavior in various engineering applications. It provides a powerful tool for predicting and understanding the complex behaviors of fluids, such as air and water, in different systems.

This chapter mainly summarises the 2D CFD analysis carried out using Ansys Fluent to investigate the aerodynamic coefficients, shedding frequencies, and Strouhal numbers of the models studied. The 3D simulations are carried out to investigate the influence of the domain type on the results. The main objective of the analysis was to evaluate the influence of the flow on the structures and to understand their aerodynamic characteristics. Using Ansys Fluent, it was possible to simulate the airflow around the hanger section and study the flow patterns, velocity distributions, and pressure profiles.

For the initial analysis, a wind domain was created within the simulation to represent the airflow around a closed wall representative of the hollow rectangular section. This allowed a basic understanding of the flow behavior to be established. The hanger sections were then gradually introduced into the wind domain, taking into account their geometry, size, and positioning. This allowed the interaction between the hanger sections and the airflow to be studied and the resulting aerodynamic effects, such as lift and drag, to be assessed.
For each model, the simulation setup was specified, including meshing techniques, solver settings, and post-processing methods.

4.2 Methodology

The simulations are performed in two-dimensional (2D) space, which allows efficient yet accurate representation of the primary aerodynamic characteristics while minimizing computational complexity. Both steady-state and transient analyses are performed to consider different aspects of wind-structure interactions. The unsteady solution was required for this study to capture the shedding frequency and calculate the Strouhal number. All the simulations have the same fluid proprieties, as shown in the table 4.1. For the steady analysis, the solution was run for 6000-12000 iterations, while for the transient solution, the convergence was reached with a time step of 0.01s for a total of 60s of flow simulation.

Table 4.1: Fluid Proprities

Fluid	air	-
Density	1.225	kg/m^3
Viscosity	1.7894e-05	kg/(ms)

4.2.1 Realisable k - ϵ

To accurately model the turbulent flow patterns around the steel section, the Realisable k-ϵ turbulence model was chosen. The term 'realisable' means that the model satisfies certain mathematical constraints on the Reynolds stresses. Neither the standard k- ϵ model nor the Re-Normalisation Group (RNG) k- ϵ model is realisable. The model used is known for its versatility in handling a wide range of turbulent flows, making it well-suited to capture intricate flow features such as streamlined curvature, vortexes, and rotation.

4.2.2 Wall treatment

The k-ϵ turbulence model used for the analysis is mostly valid in the area in which the turbulence is fully developed, this model lacks close to the wall section, giving a non-accurate solution. There are several approaches to overcome this problem one of those is to use the so-called wall function which can model accurately the near wall zone

There are many functions that can be applied, the standard ones are practical and efficient from a computational point of view, but for this specific case study was chosen to apply a different approach. These are based on assumptions that may not be valid for the simulation model. For example, they assume a logarithmic velocity profile near the wall and rely on the mesh near the wall being fine enough to resolve the viscous sublayer. For this model, although was achieved a fairly high mesh refinement, was decided to not use this approach as standard wall functions cause may not give accurate results.

Enhanced Wall Treatment

Ansys fluent allows you to use an advanced feature for the wall functions: Enhanced Wall Treatment is an advanced modeling option that is particularly useful when the standard wall functions are not sufficient. It is based on an improved turbulence concept to provide more accurate predictions of velocity and other specific properties of the viscous substrate. These features have improved accuracy in predicting wall shear stress, simulated heat transfer, and other parameters. This is particularly important for the y^+ parameter as it reduces the specific mesh quality requirements. In addition, this advanced feature is very flexible and it is possible to select the areas in which it is to be applied, for example, areas of complex geometry or points of particular turbulence. This variability is essential as it allows the computational load to be reduced.

Parameter y^+ The y^+ value is a dimensionless parameter of significant importance in the field of CFD, especially for the resolution of the fluid dynamics equations in the boundary layer region. Represents the distance of the centroid of the first grid cell from the wall of the simulated object [7]. This is a distance normalized to the thickness of the viscous boundary layer. In practice, the unit value of this parameter means that the distance of the first cell of the lily is equal to the thickness of the viscous boundary layer, [16]. Its value is given by the following formula 4.1.

$$y^+ = \frac{\rho u_\tau y}{\mu} \tag{4.1}$$

Where: ρ is the fluid density, u_τ is the friction velocity, related to wall shear stress, y is the distance from the wall (measured from the wall centroid to the cell centroid), and μ is the dynamic viscosity of the fluid.
If $y^+ < 1$, the first grid cell is located in the laminar sublayer where viscous forces dominate.
If $y^+ > 30$, the first grid cell is in the boundary layer, where the flow is completely turbulent.
If $1< y^+ < 30$, the first grid cell is within the viscous sub-layer but not too close to the surface wall, in the transition zone of the boundary layer as shown in the figure 1.1.

A y^+ value that is too high or too low can lead to incorrect predictions of the boundary

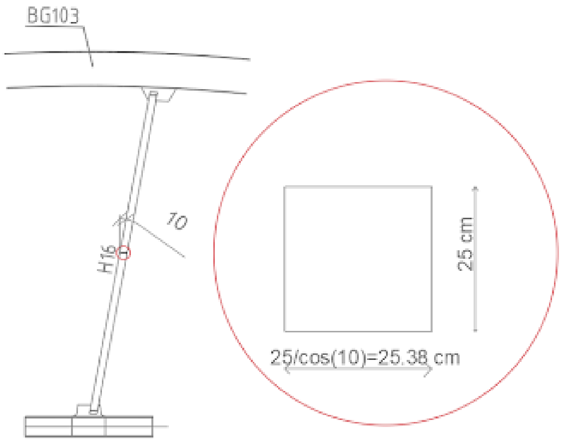

Figure 4.1: CFD rectangular section of the hanger

layer, taking into account its value you can size the mesh around the wall to obtain more accurate simulations.

4.2.3 Computational Wind Domain

For the 2D simulations, the flat section of the midpoint of the longest hanger of the arch was considered. Due to its inclination, the section taken on the median horizontal plane is not perfectly square, but has dimensions of 25.38x25 cm, as shown in the figure 4.1. The characteristic dimension (d) used to calculate the data of interest was d=25.38cm. Based on this, first attempted to size the wind domain. From previous simulations found in the literature, the first domain was of a distance from the inlet and far-field of 4 times d and a distance of 12 times d from the outlet. The domain was far too small, different sizes were tried until the last one of 20 times d from the inlet and far-field and 40 times d from the outlet was reached, see figure 4.2. It should be noted that convergence was obtained even with half the dimensions, but since the simulations had to be carried out over a very wide range of speeds, it was preferable to adopt a larger domain so as to have the same domain for all the 2D analyses.

4.2.4 Boundary Condition

In the computational domain, it is necessary to assign boundary conditions, which involves assigning certain specifications to the fluid in accordance with these conditions. There are three main boundary conditions: the inlet, the outlet, and the wall. There is a

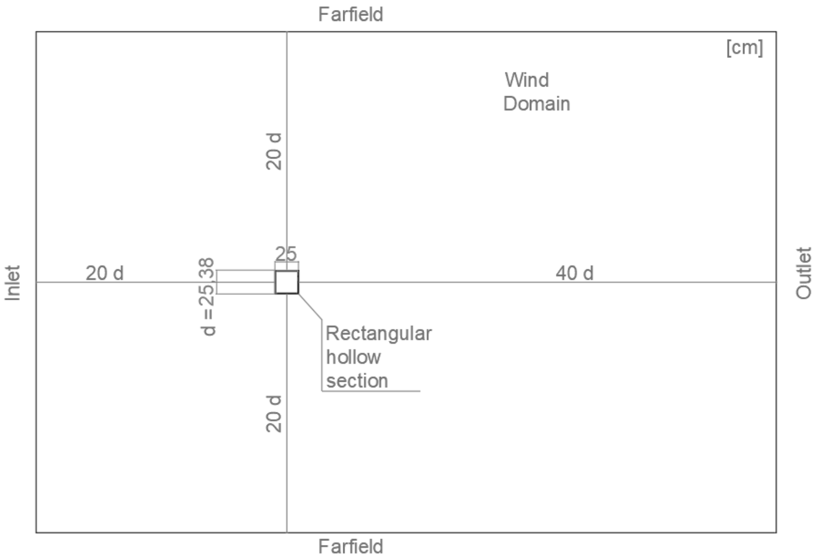

Figure 4.2: Wind domain characteristics with relative boundary conditions.

fourth one assigned to the lateral sides of the domain, those parallel to the fluid, usually the conditions related to the far-field or symmetry are assigned, but they are significant when they correspond to the walls of a cylinder with a flow inside, for example, not important for the specific case study.

Inlet

The inlet boundary condition governs the specifications of the fluid entering the computational domain, such as the inlet velocity, the reference system, absolute or relative to neighboring cells, the velocity profile, and the pressure value. Turbulence properties can also be defined by the turbulence intensity and hydraulic diameter, see 4.2, or the turbulent viscosity ratio for the inlet conditions.

$$D_H = \frac{4A_{inlet}}{P_{inlet}} \tag{4.2}$$

Where A_{inlet} is the area of a surface given by the length of the inlet multiplied by 1m of thickness, and P_{inlet} is its perimeter

Outlet

The outlet boundary condition defines the conditions at the exit point of the computational domain, where the fluid leaves the domain. The settings for the outlet are the reference frame for the backflow conditions, the gauge pressure, the pressure profile multiplier, and the method of specifying the backflow direction.
The turbulence properties can be set to be the same as those specified for the inlet.

Wall

The Wall boundary condition is applied to surfaces within the computational domain to simulate interactions with solid walls. The wall boundary condition is characterized by the motion of the wall, which is assumed to be stationary except in advanced simulations. For this boundary, a number of shear conditions are specified: for example, the 'anti-slip' condition, which ensures that the velocity of the fluid on the wall is zero and that there is no relative motion between the fluid and the wall.

For this analysis, was chose to vary the velocity of the inlet fluid between a range of 2.5 m/s and 30 m/s. The velocity profile is constant and absolute, always orthogonal to both the inlet and outlet While the pressure at the outlet is fixed at zero with a unit multiplier. It was decided to set the turbulence specifications via the turbulence intensity at 5% and the hydraulic diameter calculated by considering a surface area equal to the length of the duct multiplied by one meter of thickness. All the information about the simulation setting is collected in the table B.1.

4.2.5 Mesh

The generation of meshes for CFD analysis is the most critical part, as a compromise must be found between cell fineness and computational cost. The software allows the automatic generation of a mesh, which can then be refined in the areas of interest, such as the vicinity of the case study section and the area where the vortex wave is generated. For the multiple simulations carried out for the case study, different main techniques were used: subdivision of a generic part of the geometric model into a fixed number of parts or assignment of the subdivision dimension. Where necessary, a dependency region was created, to obtain a denser mesh. A very useful approach is to apply a growth rate that allows it to start from the densest area of the mesh and increase the size of the cells in subsequent layers by a given factor. For the area close to the section, where the mesh needs to be denser, the inflation technique can be used, which allows to creation of offsets of the section geometry with a given thickness.

In addition to the meshing approaches, it is essential to evaluate the mesh quality to ensure reliable simulation results. There are several parameters to evaluate, the most important being skewness, minimum orthogonal quality, and aspect ratio.
The skewness is the percentage difference between the optimal cell size and the actual cell size, of which it is necessary to evaluate the maximum value that varies between 0 and 1, the closer it is to zero the better, and the average skewness value is better that it is around 0.33. The orthogonal quality is a vector calculation that gives an indication

of the quality of the mesh. This quantity represents excellent mesh quality when its value is close to one, the average value for the whole mesh should be kept around 0.2. While the aspect ratio is the ratio of the base to the height of the cell, a value less than 35 indicates a good mesh.

By combining these meshing approaches and keeping the quality parameters under control, the mesh has been adapted to provide an accurate representation of the flow field, particularly in areas subject to turbulence effects. This careful mesh design contributes to the reliability and accuracy of the simulation results.

4.2.6 Solver Method

Ansys Fluent allows you to use two resolution approaches: one based on pressure and one based on density. Both can be used for CFD analysis, but in some cases, one formulation may work better than the other. These two approaches differ in the way the continuity and momentum equations are solved and the set of equations to be solved, depending on the type of analysis to be performed. In general, the pressure-based approach is used for incompressible or slightly compressible fluids. The second is used for compressible fluids and for very high simulation speeds. For this particular case study, the pressure-based approach was used.

Iterative Pressure-Velocity Algorithms

There are two solver algorithms for the pressure-based solver, one separate and one coupled. In the former, the governing equations of motion and continuity are solved individually, while in the latter, as the name suggests, they are solved in a coupled manner. The latter has advantages in terms of convergence speed at the cost of more memory.

There are five pressure-velocity coupling algorithms in the Ansys software for the pressure-based approach: SIMPLE, SIMPLEC, PISO, Coupled, FSM, and NITA, the latter being a scheme used for transient flows using the non-iterative time advancement scheme and generally this scheme works in conjunction with the above algorithms [15].

SIMPLE: this is the most widely used algorithm, both for transient and steady solutions, and uses a relationship between velocity and pressure corrections to enforce the conservation of mass and obtain the pressure field. SIMPLEC is a version that allows faster convergence but has limitations, it is used for relatively simple problems and laminar flows without additional turbulence models.

PISO: Pressure-Implicit with Splitting of Operators is best suited for transient solutions, especially when a large time step is required. For steady-state analysis, it has no advantage over SIMPLE or SIMPLE C. The disadvantage of this algorithm is the high computational cost.

FSM: The Fractional Step Method, is indicated when the NITA scheme is chosen as it is slightly less expensive in terms of computation than the PISO scheme.
For this case study it was decided to use the SIMPLE algorithm as it is ideal for both transient and steady-state solutions and is the best from a computational point of view.

4.3 Result

This section presents the results of a number of simulations, each designed to meet a specific purpose of this case study. In particular, there is a macro division between steady-state and transient simulations, the difference between the two is that the latter allows time-dependent data to be obtained and is essential to capture the shedding frequency, which is of considerable importance for the purpose of the research. The steady-state simulations were carried out primarily to have a valid model on which to run a transient simulation but also to assess how much the aerodynamic values differ between the two types of simulation. To give an idea of the time required for the simulations, the steady-state solutions, once optimized, vary in the range of 4-12 hours of simulations, while the transient solutions can take days, especially if animations of the simulation with counting features are also extracted. The steady-state simulations were used to answer another research question regarding the geometry of the section and how this can influence the aerodynamic coefficients, the choice to use the steady-state solution was dictated by the advantage in computational cost. Furthermore, once the relationship between the steady and transient simulation data has been established, it is possible to apply it to models of slightly different geometry.

4.3.1 Steady Solution

The steady solution was used to simulate wind flow of different speeds around a rectangular section and to analyze the shape of the eddies formed behind the object.
These types of simulations were used also to answer the research question regarding the geometry of the section and how this can influence the aerodynamic coefficients, the choice to use the steady-state solution was dictated by the advantage in computational cost. Furthermore, once the relationship between the steady and transient simulation data has been established, it is possible to apply it to models of slightly different geom-

etry.

Rectangular cross-section

The analysis was carried out on a single rectangular cross-section of 25.38 x 25 cm, characterized by sharp, non-rounded edges. Several simulations were carried out, covering a range of wind speeds from 2.5 m/s to a maximum of 10 m/s. Before finalizing the dimensions of the wind domain, a series of simulations were systematically run at different speeds to assess boundary interactions.

The most accurate wind domain, as shown in Figure 4.2, was selected based on observation of the simulation results and the interaction between the flow condition around the centered section and the boundaries. The aim was to obtain a wind domain large enough to allow a distinct flow zone around the focal section but at a reasonable computational cost. In this vicinity of the section the mesh was deliberately coarsened to ensure precision in data extraction, as shown in Figure 4.3.

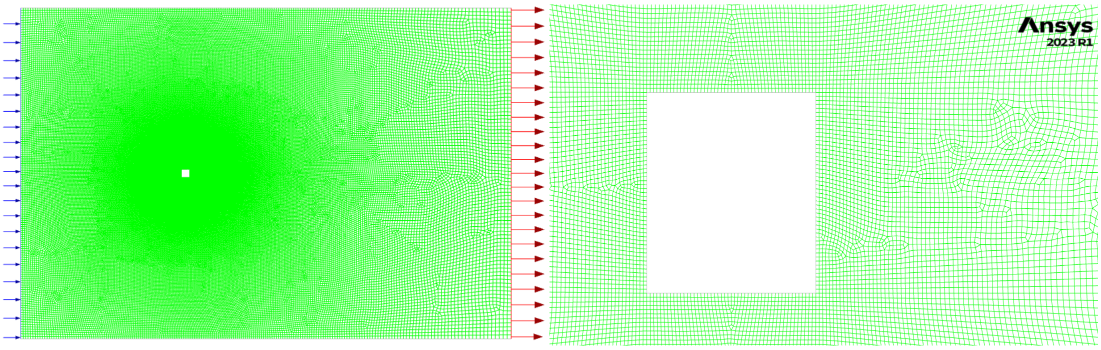

Figure 4.3: Mesh configuration of the wind domain for the steady simulation.

However, it is important to note that the steady-state simulation used in this study does not capture shedding frequencies, making the derivation of the Strouhal number unattainable. The main results extracted from these simulations include the aerodynamic coefficients: drag c_D, lift c_L, and moment c_M.
The simulation started with a number of 500 iterations, but in order to reach the convergence the number of iteration were increased to 6000 and for higher speed doubled. From the results obtained, collected in the table 4.2, it is possible to asses that for the range of speeds simulated the drag coefficient c_D increases slightly with higher wind speeds, while the lift coefficient c_L and moment coefficient c_M exhibit minor fluctuations.

Table 4.2: Rectangular cylinder: not rounded edges.

Wind speed [m/s]	2.5	5.0	7.5	10.0
n° of iterations	6000	12000	12000	12000
Drag Coeff. C_D	1.379	1.397	1.398	1.402
Lift Coeff. C_L	0.000	0.002	0.001	0.001
Moment Coeff. C_M	-5.345	-5.410	-5.414	-5.432
Turbulent Intensity	0.070	0.070	0.070	0.070

The drag coefficient, denoted by c_D, represents the resistance of a cross-section in the direction of the wind flow. The trend of increasing c_D with increasing wind speed is consistent with the fact that the drag force is proportional to the square of the flow velocity. However, it should be noted that this relationship cannot be extended to all speeds, as the drag force also depends on other factors. This issue will be covered in the following sections. An intriguing outcome is achieved for the lift coefficient c_L, which gauges the force perpendicular to the flow. Since the wind force acts without any angle of attack, it is unsurprising that the coefficient fluctuates around zero. This implies that, on average, the hanger division undergoes negligible lift, suggesting that the structure does not create considerable upward forces, a desirable trait for maintaining structure stability. The moment coefficient c_M denotes the hanger section's inclination to rotate in response to fluid forces. Negative values signify the section's orientation of rotation. As with c_D, c_M increases with wind speed, denoting that the section encounters amplified rotational forces at higher wind speeds.

An intriguing outcome of CFD simulations is the recognition of contouring and pathlines in close proximity to the section. This provides a simpler comprehension of the flow motion and its dynamics. Some examples are shown below in Figures 4.4, 4.5. These are extrapolated from the simulation carried out with a wind speed of 5m/s at the inlet.

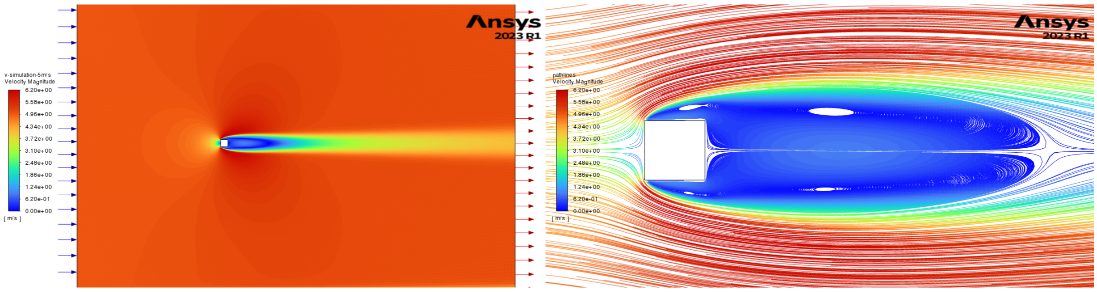

Figure 4.4: Wind flow velocity magnitude: contouring and pathlines.

The symmetrical contouring of pathlines and observation of two perfectly symmetrical vortexes behind the section indicate a steady flow simulation. The vortex region is symmetric about the mid-axis of the wind domain, and its length remains constant in time for each speed. However, an expected result is that the vortex length increases with Reynolds, which corresponds to speed [17]. Small vortexes also form in proximity to the section's side walls, and at the tail end of the two primary vortexes. These vortexes generate dynamic forces on the studied structure, and their positioning and dimensions can significantly impact the section's integrity.

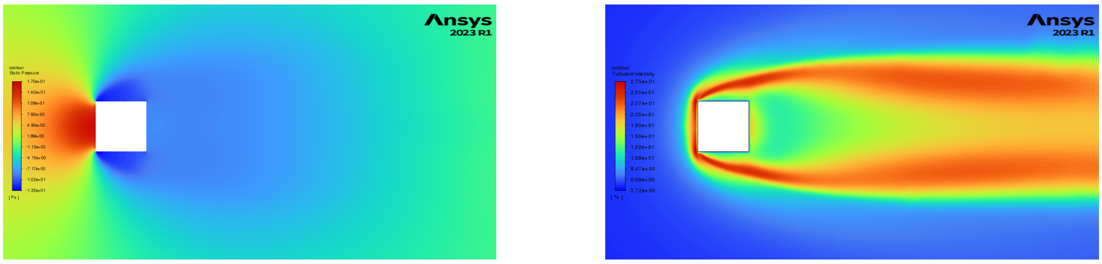

(a)

(b)

Figure 4.5: Wind flow contouring: static pressure (a) and turbulence intensity (b).

When a fluid strikes a body, two distinct pressure zones are commonly observed. These regions in aerodynamics are referred to as the "high-pressure region" and the "low-pressure region". The high-pressure zone is located in the forward portion of the object, where the air slows down and compresses after striking the front surface of the section. The second region is situated at the rear of the section and relates to an area where the pressure decreases due to the formation of vortexes. These vortexes entail a continuous change in the wind direction.
Identifying these two regions is highly important in the field of aerospace as they determine the lift and drag forces acting upon the object. Furthermore, it is crucial to recognize them in structural engineering to understand how aerodynamic forces act on the object.

High turbulence intensity regions form at the front of the section, indicating that the air in these zones is turbulent and has significant fluctuations in velocity. This phenomenon is commonly observed at the stagnation point of an object where the flow comes to a halt and changes direction. The turbulent flow in this area is the result of the interaction between the oncoming flow and the section wall.

Rectangular cross-section rounded edges

In this section, various simulations are conducted with diverse model geometries. The wind domain dimensions and simulation settings remain constant and unaltered, with

the change being implemented solely in the hanger section of concern. Alterations to the mesh were necessary, but diligent effort was made to ensure that quality parameters were comparable or higher than those in the previously presented simulations.
Firstly, three models with varying connecting radii but identical speeds were assessed at a wind speed of 2.5 m/s. This analysis aims to determine the impact of section geometry on the aerodynamic coefficients.

Table 4.3: Aerodynamic coefficients for different model geometries with different radii.

Edge geometry	C_D	C_L	C_M
not- rounded	1.379	0.000	-5.345
r = 1 cm	0.889	0.059	-3.249
r = 1.5 cm	0.779	-0.034	-3.082

Table 4.3 displays the outcomes of three different models, one without rounded edges, the second with an edge radius of 1 cm, and the third with a higher radius of 1.5 cm. The presence of the radius in the wall section undoubtedly affects the aerodynamic coefficient. As the edge radius increased, the non-rounded geometry experienced the highest drag coefficient. At 1 cm and 1.5 cm radii, a notable decline in C_D was evident. Smoothing and increasing the size of the radii of the edges generally decreases drag, in accordance with a common principle of aerodynamics. The reduction in drag is linked to an improvement in the flow characteristics around the section. The edge that was not rounded generated a significant negative moment, demonstrating a strong inclination to rotate under the influence of fluid forces. The negative moment magnitude decreased with rounded edges (r = 1 cm and r = 1.5 cm), which implies a reduced tendency to rotate. Rounded shapes generally result in greater stability due to the reduction of moments that might cause rotation.

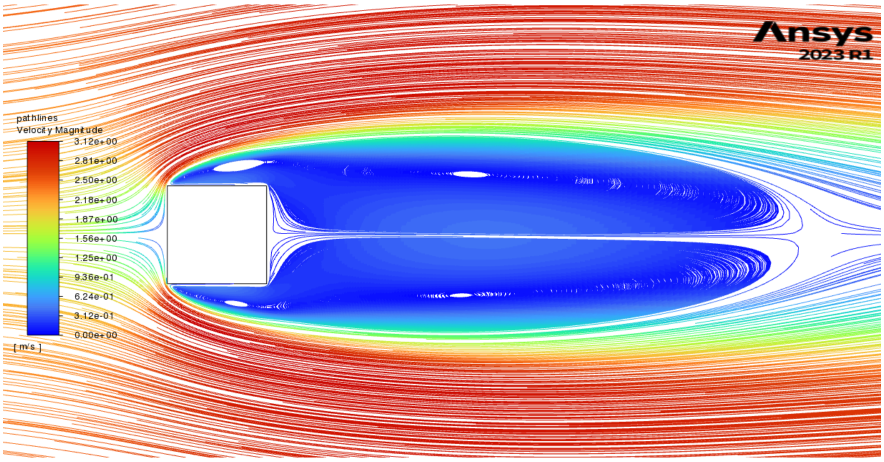

Figure 4.6: Not rounded edges

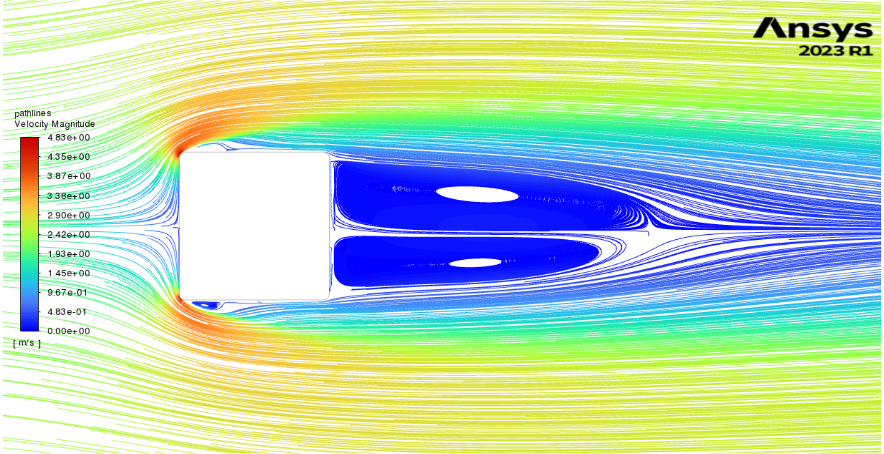

Figure 4.7: Edge r = 1 cm

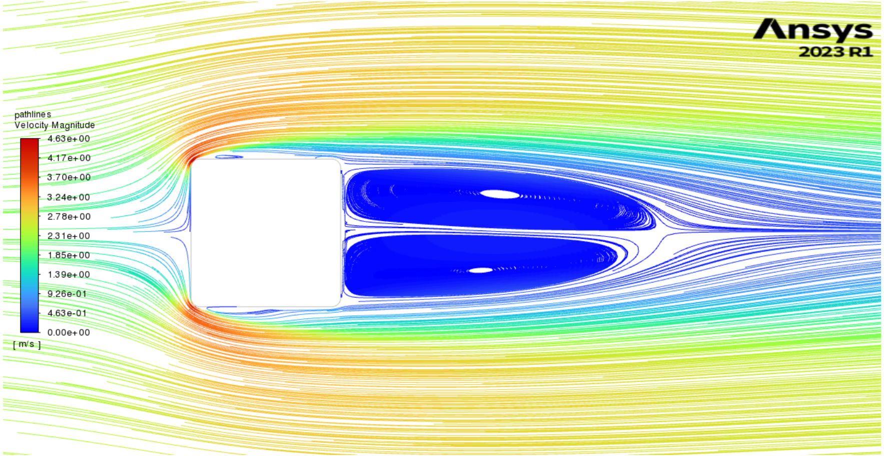

Figure 4.8: Edge r = 1.5 cm

After analyzing the pathlines shown in the figures 4.6, 4.7, 4.8, of the three different sections, it becomes clear that the radius significantly influences the fluid flow behavior. In particular, the streamlines and vortexes are notably impacted by the presence of a radius.

Sections with radii exhibit significantly shorter vortex waves compared to the sections without rounded edges. This phenomenon suggests that the vortexes generated by rounded sections are more confined and compact. The velocity of the fluid flow near the rounded section is significantly lower. The presence of radii seems to reduce the turbulence effects with a consequent increase in the velocity of the fluid flow.

These observations lead to an important conclusion: the resistance encountered by the wind flow is reduced when a section contains radii. The introduction of rounded edges alters the flow patterns, limiting the development of vortexes and reducing the flow velocities in the vicinity of the section.

In practical terms, this means that it is essential to consider the actual radii of the

Table 4.4: Aerodynamic coefficients for the steady solution with section r = 1cm.

Wind speed [m/s]	2.5	5.0	7.5	10.0
n° of iterations	6000	12000	12000	12000
Drag Coeff. C_D	0.889	1.096	1.144	1.145
Lift Coeff. C_L	0.059	0.019	0.000	-0.011
Moment Coeff. C_M	-3.249	-4.155	-4.390	-4.426
Turbulent Intensity	0.100	0.090	0.090	0.090

section edges in order to achieve accurate and realistic simulations. However, for a conservative approach, it may be advantageous to ignore the radius in the simulation. This effectively overestimates the resistance of the section and provides a safety margin. This conservative approach ensures that the verification process accounts for higher aerodynamic forces, thereby increasing the safety and reliability of the structure.

This analysis was extended to evaluate the effect of edge radius, particularly at 1 cm radius, over the remaining three wind speeds. The aim was to investigate whether the trends observed at 2.5 m/s persisted as wind speeds increased. The results confirmed that the hypotheses formulated on the basis of the 2.5 m/s simulations were consistent and applicable to higher wind speeds.

Table 4.4 provides a detailed breakdown of the effective aerodynamic coefficients when considering the presence of a 1 cm edge radius.

In summary, the analysis of the steady-state solutions showed consistent trends over the range of wind speeds investigated. As the wind speed increased, the aerodynamic coefficients showed an upward trend. In addition, these coefficients decreased, i.e. resistance decreased, with the introduction of edge radii, 4.9.

In the 2D simulations, two key aerodynamic coefficients emerged as crucial: the drag coefficient, which represents the section's resistance to wind flow, and the moment coefficient, which indicates the resistance to rotation due to wind forces.

4.4 Transient Solution

The time-dependent simulation creates an unsteady solution that allows the extraction of time-dependent data, capturing aerodynamic effects over different temporal scales. Shedding frequencies and related parameters, including the Strouhal number, can be obtained through this process. This type of analysis provides a detailed examination and comprehensive observation of the phenomenon of flow regimes and turbulence effects.

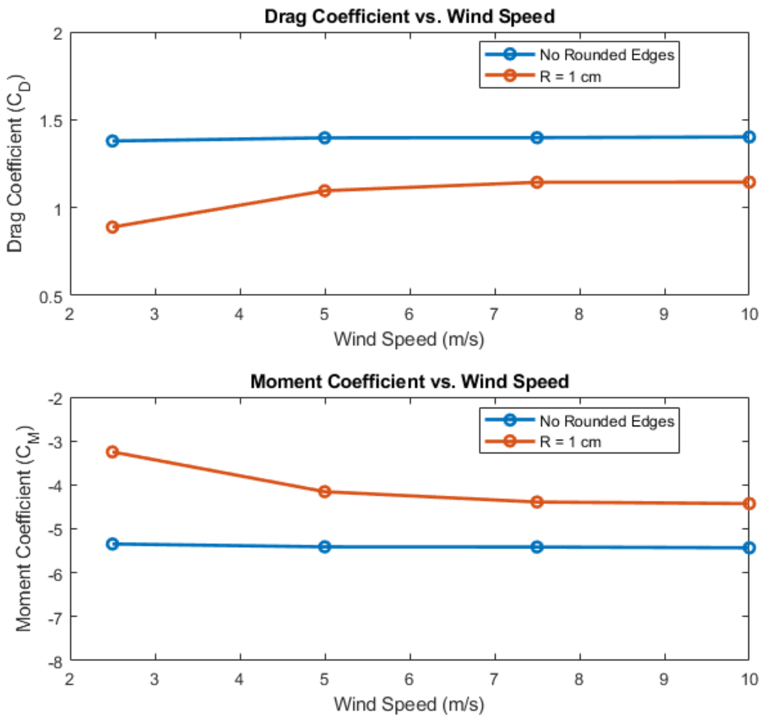

Figure 4.9: C_D and C_M at different speeds of rectangular sections with rounded and not rounded edges.

The range of speeds utilized in these simulations is wider than that utilized for the steady solution, as the focus is shifted towards high speeds and Reynolds number.
All simulations were run for a duration of 60 seconds with a time step size of 0.01 seconds. A sensitivity analysis was conducted for the time step size by refining it for a few speeds, but the variation in the results was insignificant.
In this section, was employed two different models. The first model utilized a single cross-section of the hanger H16, which was identical to the one used for the unsteady solution, with no rounded edges. The second model included three different sections to evaluate the impact of multiple sections on the data of interest. For this final model, the wind domain was increased while maintaining a minimum distance of 20d from the last lateral wall.

4.4.1 Rectangular cross-section

The study assessed various wind speeds ranging from 2.5m/s to 30 m/s. The decision to increase the maximum speed to 30 m/s was necessary, since the characteristic mean wind speed observed at the bridge's location, amounted to 27 m/s.
The findings of the study will be presented in this section utilizing also the corresponding Reynolds number, given that aerodynamic parameters are depicted as a function of

the Re number.

Aerodynamic coefficients, see Table B.2 were extracted for each simulation. The estimated peak frequency of drag and lift, Table B.3, was then calculated using Fast Fourier Transformation (FFT) of their respective signals, and related amplitudes were subsequently extrapolated. This allowed for the calculation of the Strouhal number, Table B.4 based on the estimated peak frequency of lift. Finally, the magnitude of both drag and lift forces was evaluated, and all the data extracted for this model can be consulted in Table B.5.

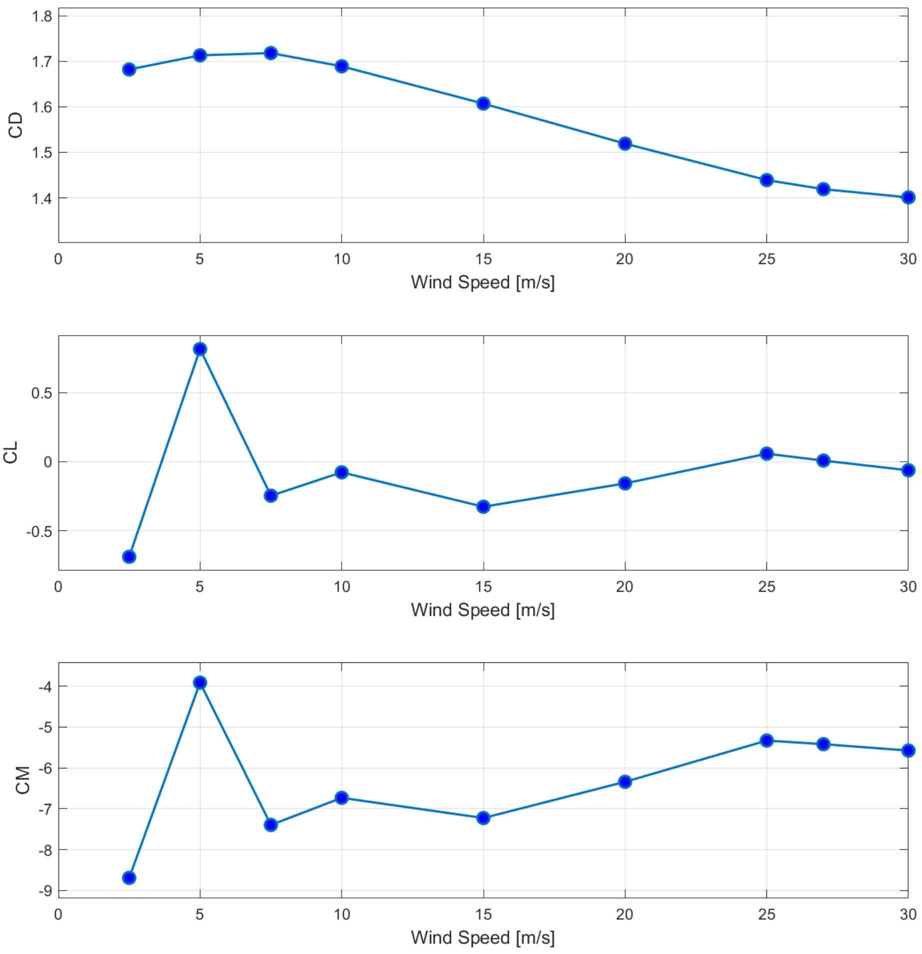

Figure 4.10: Unsteady solution: aerodynamic coefficient at different speeds.

The graphs in Figure 4.10 depict aerodynamic coefficients for a rectangular cross-section that was derived from an unsteady solution at varying wind speeds.

There is a tendency for the drag coefficient (C_D) to decrease as wind speed increases, reaching a minimum of 30 m/s. However, until a speed of 10 m/s is reached, the drag coefficient actually increases, following the same trend as observed in the unsteady solution. Nevertheless, for the remaining speed range, the behavior aligns as expected with the results reported in the literature [18], [19]. This is due to the fact that at higher wind speeds, flow around the structure becomes more streamlined, thereby reducing drag.

For 2D simulations, the coefficient of lift (C_L) is of little significance as its value is small and oscillates around zero. Therefore, it is not possible to define a specific trend for the lift, which changes randomly in magnitude and sign due to the oscillating value around zero.

The moment coefficient gradually decreases at higher speeds, following the trend of the drag coefficient. It appears that there has been a decrease in C_M, indicating a reduced susceptibility of the structure to rotation under wind influence.

The following results are not directly extracted from the simulation report but are obtained by using the aerodynamic coefficient values calculated at each time step to determine the frequency and the Stouhal number.
The frequency domain for both lift and drag was calculated for all unsteady simulations, and subsequently, the Stouhal number was obtained after determining the peak lift frequency.
The initial 10 seconds of the data signal were removed as an initialization period to enhance the accuracy of the results. Then, the Fast Fourier Transform (FFT) was utilized to convert the time-domain data into the frequency domain. This transformation was crucial in comprehending the response of the cross-section to the wind flow in the frequency domain.
After obtaining the frequency spectra, the peak frequencies were identified for both lift and drag.4.11. The trend of the frequencies consistently increases with higher wind speeds, indicating a proportional response to the changing aerodynamic regime.
The amplitude variation of drag and lift forces is a compelling point of interest. The drag coefficient's magnitude is significantly greater than that of the lift coefficient, but the relation between their respective amplitudes is not consistent. The lift experiences a much higher amplitude than the drag. Of note, wind speeds exceeding 20 m/s result in a significant change in the dynamic response, marked by a reduction in drag amplitude. This alteration may indicate a shift in the main forces caused by the flow or a change in the general flow pattern around the structure as the speed increases and the flow

becomes more streamlined.

An intriguing observation pertains to the drag frequency magnitude, which fluctuates between 5.5 Hz and 8 Hz for wind speeds ranging from 5m/s to 10m/s. According to the Abaqus frequency analysis, the first natural frequency of the structure is approximately 6 Hz, while the others vary within a range of up to 14 Hz. The initial natural frequency's vibration is out of plane. As a result, it can be concluded that the critical wind speed for the hangars ranges from 5 to 8m/s. This wind speed range is an ordinary value for the geographic allocation of the Bomarsund Bridge.
The calculation of the Strouhal number, a significant parameter that signifies the shedding of vortexes surrounding the structure, takes into account the lift peak frequency. A decreasing trend of Strouhal numbers with increasing wind speed is observed,4.11 indicating that a shift from regular to more irregular vortex shedding patterns is occurring.

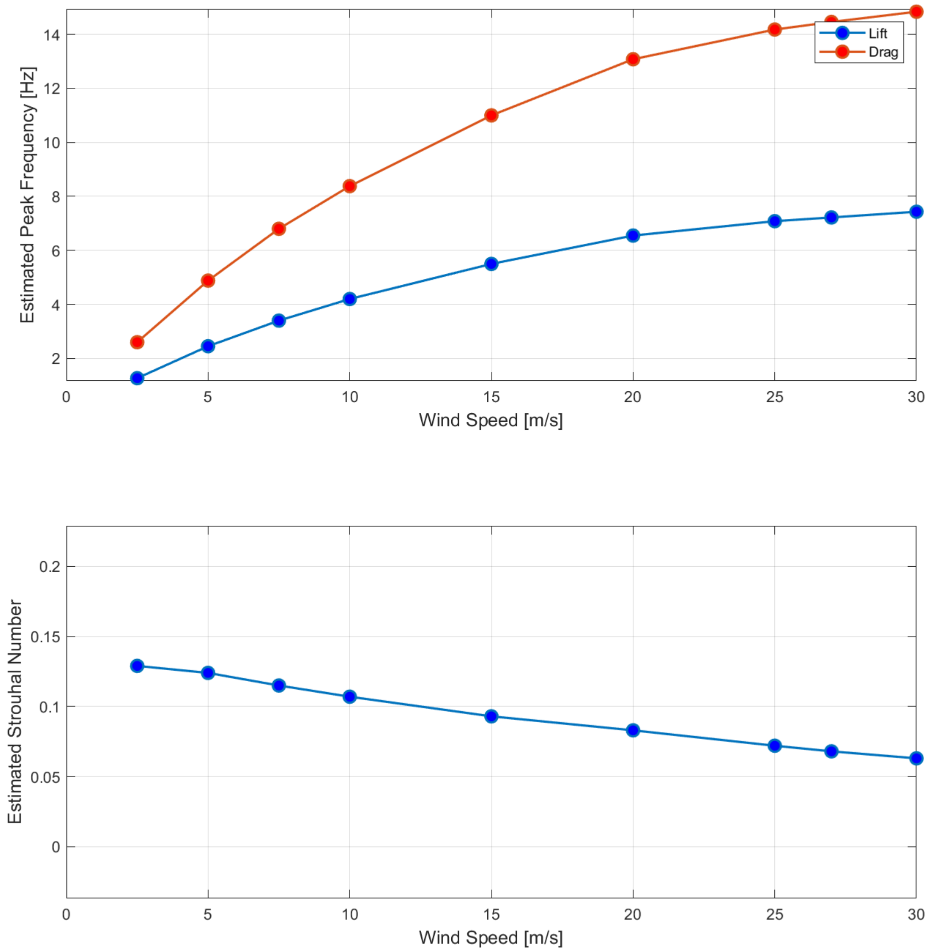

Figure 4.11: Unsteady solution: estimated peak frequency and Strouhal number

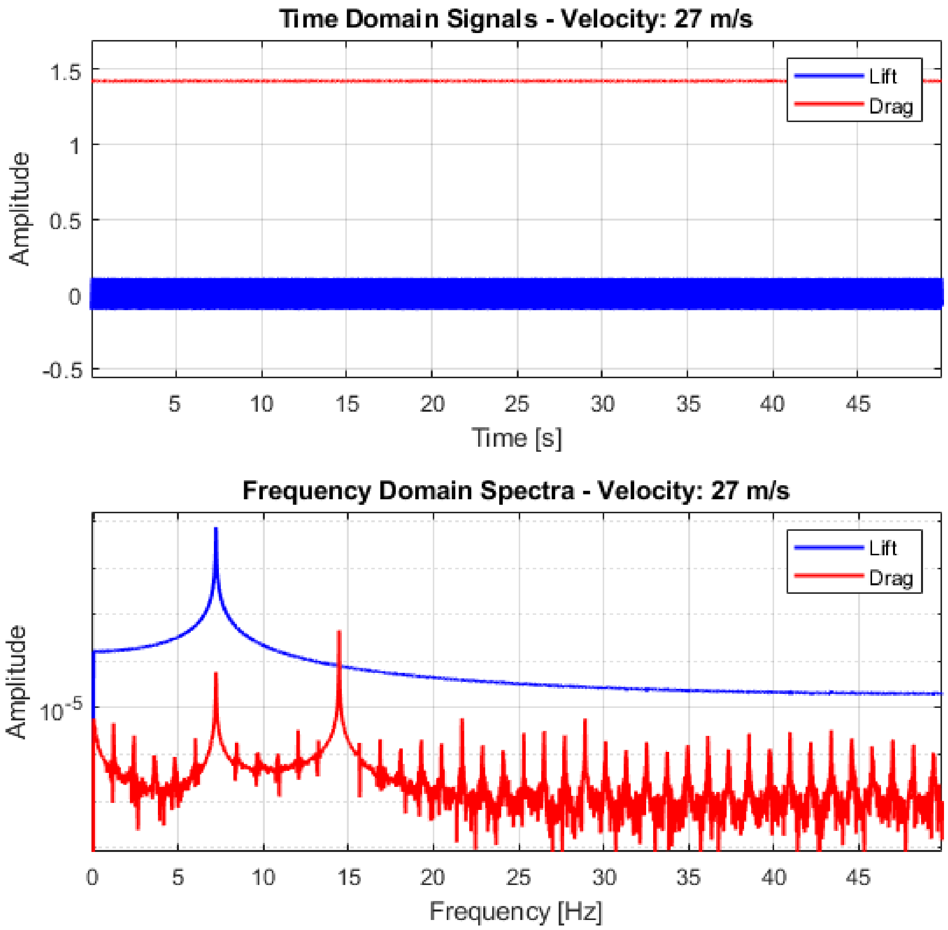

Figure 4.12: Time domain spectra and frequency domain spectra at wind speed of 27 m/s

A characteristic phenomenon of vortex shedding was observed, wherein the peak frequency of drag is twice that of lift in the frequency domain spectra. This outcome can be elucidated by the vortex-shedding process and its interaction with the composition.

Two vortexes of equal strength and opposite signs are shed during each oscillation period in the wake of a structure, such as a rectangular cross-section. It is important to note that the sign of the vortex has no impact on the experienced drag force. This distinctive feature results in a period-doubling effect, in contrast to the lift oscillation. An example of the frequency spectrum in the simulation at a speed of 27 m/s can be observed in Figure4.12.

In this particular study, the drag force is identified as the main force due to its alignment with the flow direction. To ascertain the accuracy of the results, a comparison

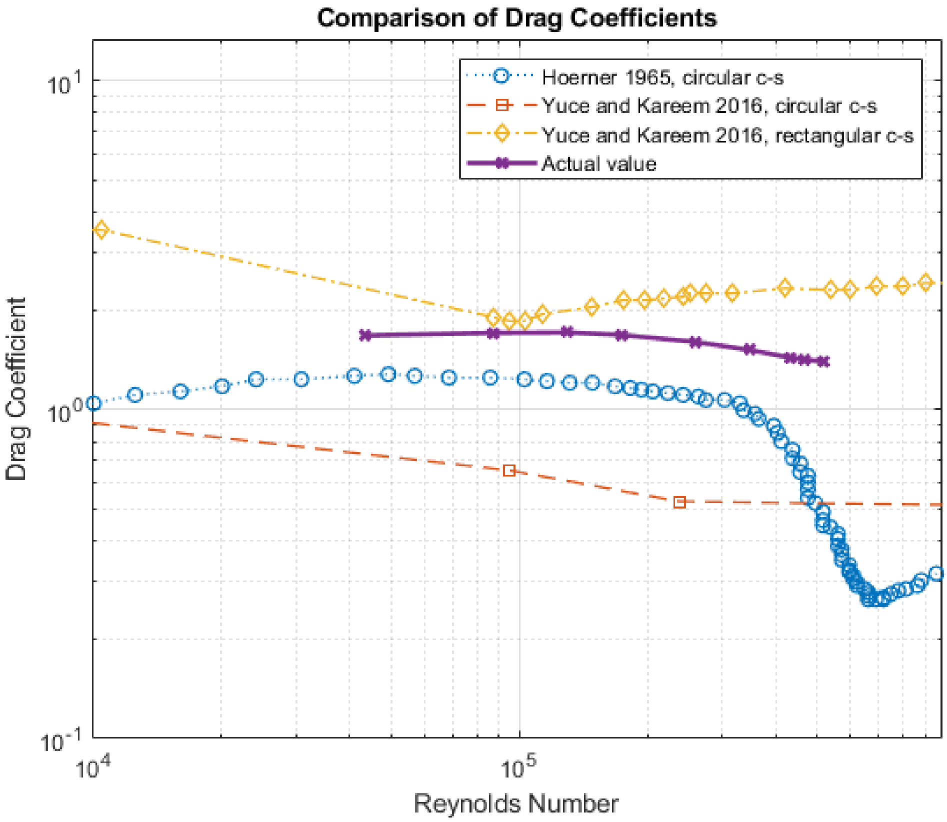

Figure 4.13: Aerodynamic coefficients vs Reynolds

was conducted with literature values, Figure4.13, and two references were consulted: Hoerner's famous drag curve for circular cross-sections [18] and a comprehensive investigation carried out by Yuce and Kareem in 2016 [19]. The latter reference was of significance because it utilized ANSYS Fluent simulation setup and investigated both square and circular sections. In their study, they simulate a wider range of Reynolds numbers, but for the current study case, the Reynolds range is correlated to the range of possible wind speed for the bridge, resulting more limited.

Considering the Hoerner curve, the current simulation results consistently indicated drag values above those of the reference. This variation is justified since Hoerner's curve relates to an ideal circular cylinder, whilst the study concerns a bluff body with a rectangular cross-section.

Referring to the research of Yuce and Kareem, who established distinct curves for circular and square cylinders, the actual rectangular cross-section results take place in the middle of that range. This placement can be considered adequate, the study case uses few simulations for a wide step of Reynolds, while the current study uses narrow steps of Reynolds, describing better the curve in the considered range, Figure 4.13.

Regarding the wind flow configuration, it is interesting to observe how it changes above the range of wind speed simulated. At low speeds behind the bluff body, the Von Karman vortex street forms, allowing the identification of zones where the flow changes direction and local eddies form. As wind speeds increase, the vortex shedding tail becomes more compact and less turbulent, resulting in a more streamlined flow. This explains the reduction in the magnitude of the drag coefficient. In Figure 4.14, two contour images are presented as examples for modifying the vortex shedding tail for low and high wind speeds - one at 7.5 m/s and the other at 27 m/s.

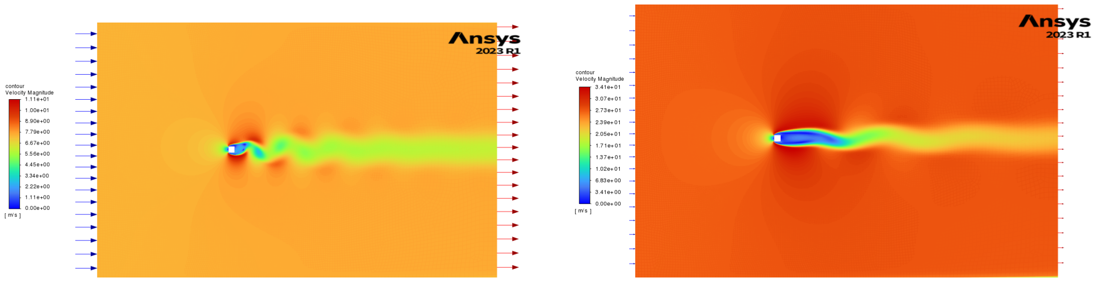

(a) v=7.5 m/s

(b) v=27 m/s

Figure 4.14: Unsteady solution: Velocity contour at different wind speeds.

It is also noteworthy to examine the form of the shedding vortex located at the rear of the cross-section. For the steady solution, the two vortexes were symmetric, but with an unsteady analysis of the effect of turbulence over time, it is apparent that this symmetry is lost. Additionally, lower wind speeds result in larger eddies that are also distributed laterally to the section. At high velocities, the vortex tail becomes more streamlined, and a second vortex forms above the first one. Some examples are reported in the Figure, for different speeds that cover the whole range of wind speed simulated.

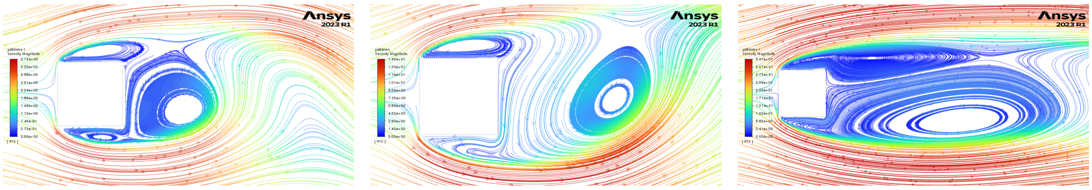

(a) v = 2.5 m/s

(b) v = 10 m/s

(c) v = 27 m/s

Figure 4.15: Unsteady solution: wind pathlines at different speeds.

4.4.2 Interaction between different sections

The following analysis was conducted on a different model. To determine the effective distance between sections, the section of the nearest hangers on the left and right of hanger H16 was added to the previous section. The section spacing equals the actual

distance between the hangers, measured at the middle hanger's height. The wind model is larger than the one used for the single section. The distance between the lateral wall section and the far field is maintained at three times *d*. To calculate the aerodynamic coefficient, the characteristic width of influence is modified, with the new d_new = *0.7614 m* being equal to the sum of the widths of the three sections. It is worth noting that we used the lift frequency of the multiple-section model for the Strouhal number but considered the width of one cross-section when calculating its magnitude. This is because S_t is related to a single vortex shedding wave.
Before conducting unsteady simulations of the three-section models, a steady simulation was carried out to assess mesh quality, wind domain dimensions, and result convergence. All the remaining simulation settings were maintained the same as the previous transient simulations.

Table 4.5: Unsteady solution multi-section model: data extracted for each speed simulated

Wind speed [m/s]	2.5	10	20	25	30
n° time steps	6000	6000	6000	6000	6000
time steps size [s]	0.010	0.010	0.010	0.010	0.010
Drag Coeff C_D	1.782	1.797	1.682	1.657	1.647
Lift Coef. C_L	-0.348	0.119	-0.038	-0.050	0.051
Moment Coeff. C_M	26.81	17.73	19.59	19.55	17.44
Estimated Lift Peak Frequency [Hz]	1.333	4.233	6.432	6.949	7.3321
Estimated Strouhal Number	0.1353	0.1074	0.0816	0.0705	0.0620

The trend of decreasing drag coefficient with increasing wind speed is maintained as studied for the single section model. However, the drag coefficient for the model comprising three cross-sections is significantly lower than that of the model featuring only one cross-section, as depicted in Figure 4.16.

The aim of this analysis was to evaluate the interaction between multiple sections and their impact on the aerodynamic coefficient and related parameters. By adding two additional sections to the wind domain, the characteristic dimension of the model increases almost three times that of the previous model. In terms of the response of the entire body to the encountered wind flow, its resistance increases. However, the three distinct vortex shedding waves formed behind each section interact with each other, influencing both the frequency of the system and the amplitude.

In Figure 4.17, an example of the lift signal for a wind speed of 10m/s is reported. The signal's amplitude drastically decreases around t=10s s and t=40s, which is an effect of the interaction of the eddies formed behind each section. Of interesting observation

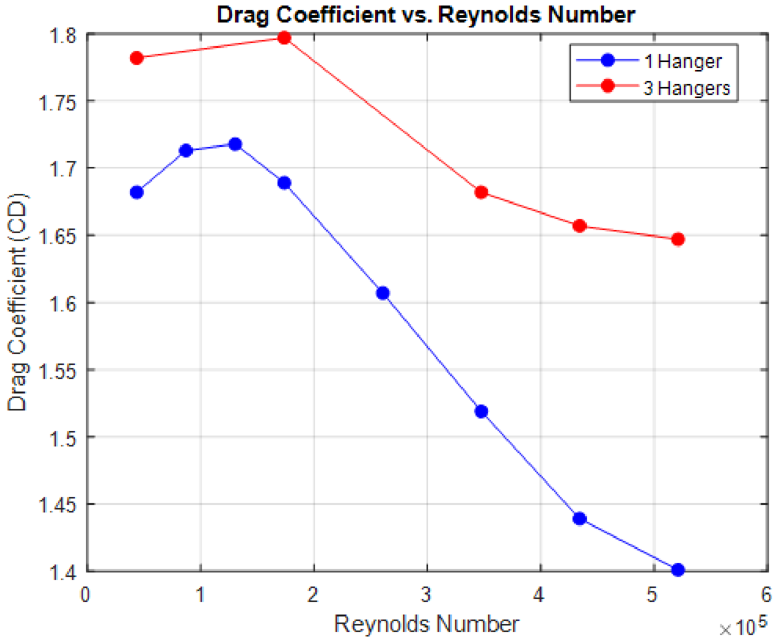

Figure 4.16: Unsteady solution: Drag coefficient of different models.

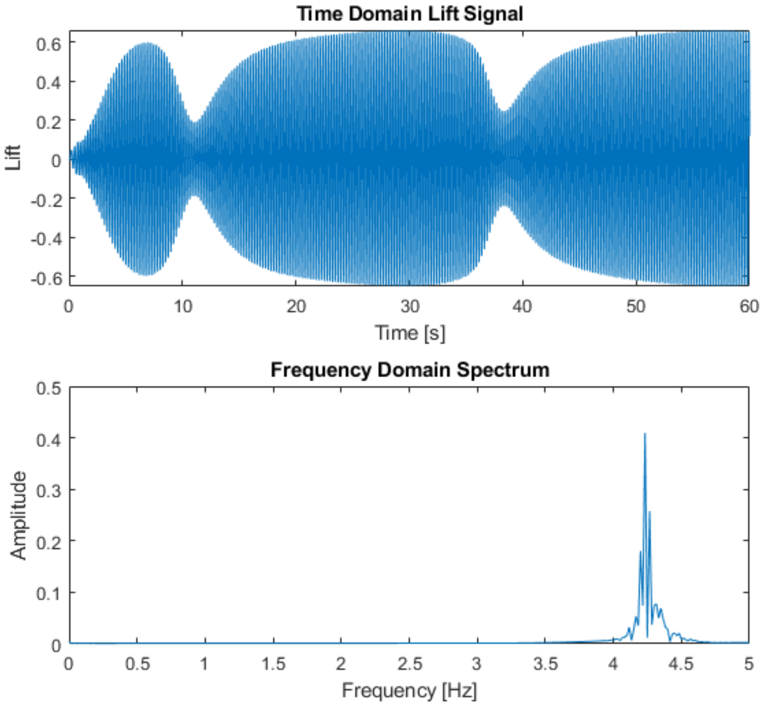

Figure 4.17: Unsteady solution multi-section model: lift signal and frequency domain spectra for wind speed of 10m/s.

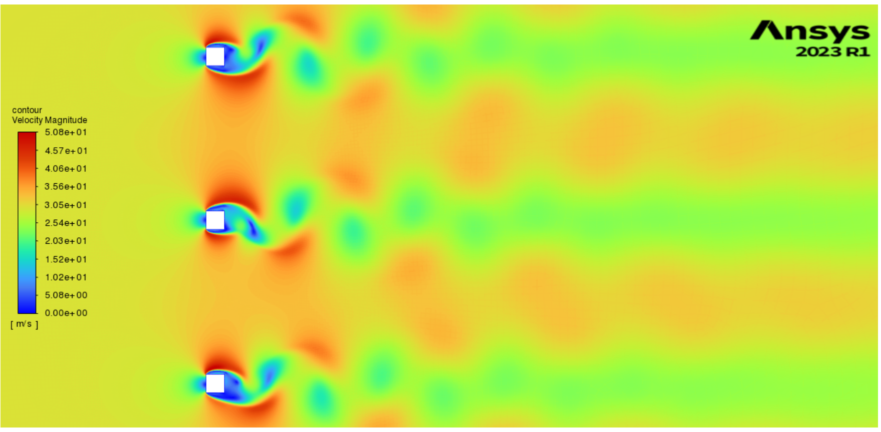

Figure 4.18: Unsteady solution multi-section model: velocity magnitude contour for a wind speed of 30m/s, H15-H16-H17.

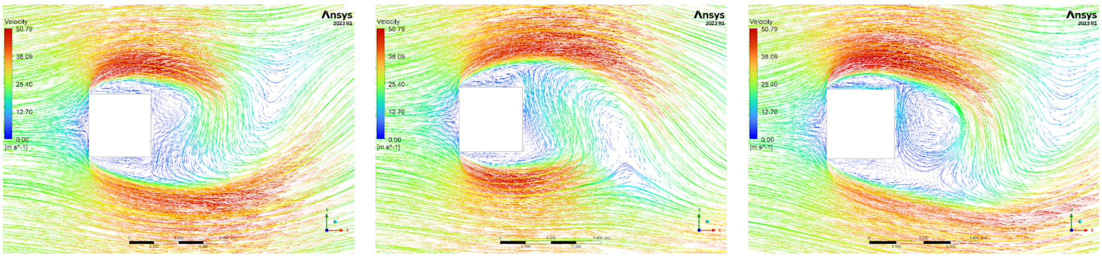

(a) Hanger H15. (b) Hanger H16 (c) Hanger H17

Figure 4.19: Unsteady solution multi-section model: velocity pathlines of the three hangers.

is the velocity contour, displaying the distribution of eddies within the wind domain. The central section displays the highest density of eddies, Figure 4.18, whereas their distribution varies across the distinct sections, the orientation and the dimension of the principle vortex change. This phenomenon is visible in the Figure 4.19.

Focusing on the frequencies and amplitudes, both models demonstrate an increase in the frequencies of drag and lift with increasing wind speeds. However, the second model generally displays reduced frequencies in comparison with the first model.
The second model with several sections illustrates a more nuanced aerodynamic reaction. The findings imply that the structural intricacy introduced by multiple sections affects aerodynamic behaviour considerably, accentuating the significance of such details in realistic simulations.

4.4.3 Wind Load Calculation

The following section presents the findings for defining the wind load in accordance with the Eurocode. The same approach outlined in Section 1.4 was used, with parameters extracted and summarised in Table 4.6. To assess the results, the critical wind speed was calculated and verification conducted to determine if vortex shedding phenomena should be taken into account. For this calculation, were used the first two natural frequencies of the initial model implemented on Abaqus, see Section 3.3.1 .

The first mode shape oscillates transversally to the direction of the bridge at a frequency of 6.63 Hz, while the second natural frequency has a magnitude of 14.06 Hz, relating to longitudinal vibrations. The critical wind speeds for each i-th frequency, which were calculated using the equation 1.9, are $V_{crit,1} = 13.80$ and $V_{crit,2} = 29.28$, respectively. Both of these critical velocities are below the safety threshold of $V_{crit,min} = 34$ above which vortex shedding can be ignored.

After determining the critical wind speeds for each vibration mode shape, the wind's inertial force, taking into account the presence of shedding frequency, was calculated using the equation. The values of inertial wind force for the first and second mode shapes are $F_{w,1} = 6[kN/m]$ and $F_{w,2} = 28[kN/m]$, respectively.

Instead of using the Strouhal numbers given by the Eurocode, it is possible to use those obtained from the unsteady simulation of the model with a single rectangular cross-section without rounded edges at a speed of 27m/s (which corresponds to the mean wind characteristic speed). Then the resulting wind forces for each i-th natural frequency will be: $F_{w,1} = 19[kN/m]$ and $F_{w,2} = 87[kN/m]$, respectively.

The Strouhal number supplied by the Eurocode for a rectangular cross-section remains constant regardless of wind speed, equating to $S_t = 0.12$. However, according to the simulation conducted for this case study, the Strouhal number changes with the wind speed and particularly decreases with wind speed. As a result, for the simulation of a wind speed of 27 m/s, the Strouhal number was equal to $S_t = 0.068$. As specified in the Section 1.2.4, a low Strouhal number typically indicates that the vortex shedding frequency is well matched to the natural frequency of the structure. In such cases, the potential for resonant vibrations is higher.

Table 4.6: Parameters for Wind load Calculation According to Eurocode

Parameter	**Value**
Terrain Category	Class I
Basic Wind Speed, v_{b0}	23 m/s
Wind Directionality Factor, C_{dir}	1
Seasonal Factor, C_{season}	1
Reference Wind Speed, v_b	23 m/s
Reference Height, z	10 m
Roughness Length Factor, z_0	0.01 m
Minimum Height for Wind Speed Profile, z_{min}	1 m
Maximum Height for Wind Speed Profile, z_{max}	200 m
Terrain Factor (k_r)	0.17
Roughness Factor (c_r)	1.173
Orography Factor (c_0)	1
Mean Wind Velocity (v_m)	27 m/s
Strouhal Number (S_t)	0.12
Structural damping (δ_s)	0.006
Scruton number (S_C)	11.575
Characteristic width (d)	0.25 m
Reynolds number (Re)	4.61E+05
Maximum displacement (y_{max})	200 m

4.4.4 3D Unsteady Analysis of hanger H16

This section introduces a distinct analysis using a 3D model, which is a departure from the previous 2D space domain investigations. With the introduction of three-dimensional geometry, significant changes occur in the mesh and the characteristic reference dimensions.

In the model used, the inclination of the hanger of 11° was taken into account and the final geometry is shown in Figure 4.20. The wind domain has an inlet dimension of 10.25m, while the far field dimensions extend to 15.25m, and a height of 11 m. The hanger is positioned centrally between the two far-fields and 5m from the inlet.

A steady-state solution was run on the model before initiating a transient simulation. The aim of this step was to optimize the mesh size and wind domain volume to find a compromise between the accuracy of the simulation results and the computational cost,

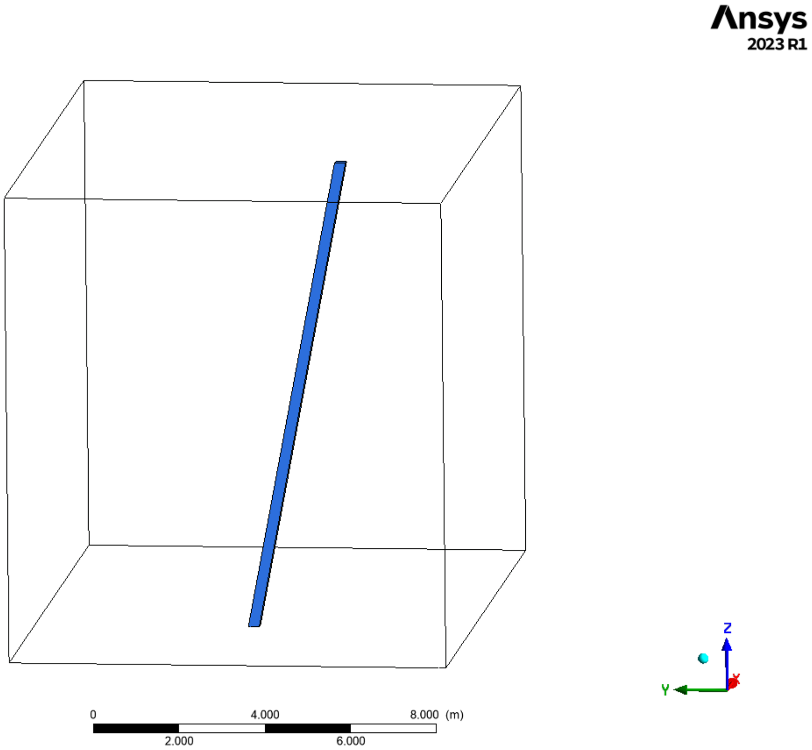

Figure 4.20: Unsteady analysis: 3D model for Ansys simulation.

which is much higher than the 2D simulation. The mesh followed a similar approach to the 2D model, incorporating enhancements to maintain a high quality mesh. The meshing size was refined in proximity to the hanger element, and the distribution of the boundary condition is the same as used for the 2D models..

The simulations covered a range of wind speeds, mirroring the speeds analyzed in the previous 2D rectangular cross-section model. This approach facilitates a comparative assessment of the differences between the two models.

The simulations were run for a maximum of 60 seconds, with a time step size of 0.01s and a maximum of 10 iterations for each step.
For each simulation the aerodynamic coefficient, pressure, velocity magnitude, and turbulence parameters were extracted, see Table B.6. The same calculation performed for the 2D models was also performed for the 3D geometry. It was considered as a characteristic area equal to the depth of the section of 0.25m times the height of the hanger of 11.30m. To obtain the Strouhal number, the depth $d = 0.2538\ m$ was used as the characteristic dimension since the aim was to define this value for the rectangular cross-section, rather than the 3D rectangular cylinder.

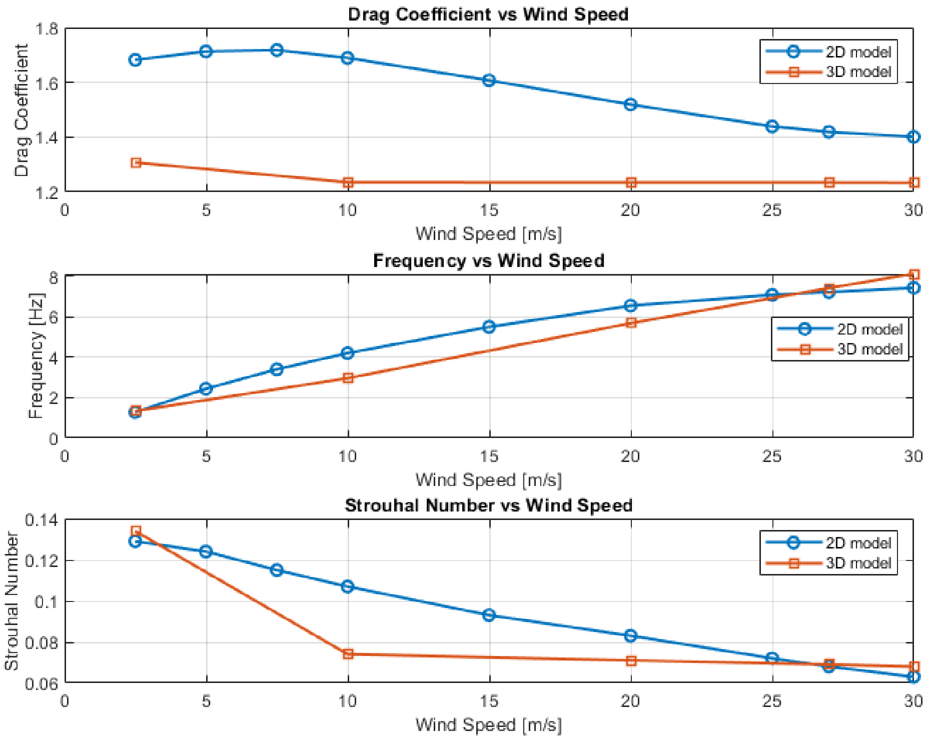

Figure 4.21: Comparison between 2D model and 3D model results.

Looking at the graphs in Figure 4.21, a clear pattern in the drag coefficient with increasing wind speed is evident when examining the results of the 3D model of the hanger. In contrast to the 2D model where there were significant variations of the aerodynamic coefficient between different speeds, the 3D model depicts a more nuanced distinction. In addition, the magnitude of the aerodynamic coefficients is generally lower in the 3D model, when compared to the 2D counterpart.

Besides, an especially captivating observation is apparent in the lift frequency domain. The frequency generally increases over the wind speed range, but specific values at various wind speeds exhibit unexpected disparities. Notably, at a wind speed of 10 m/s, the lift frequency for the 3D model is significantly lower than the corresponding value for the 2D model. However, at higher speeds, the frequency magnitude slightly surpasses that of the 2D model. The same trend is observed for the Strouhal Number.

The analysis of drag frequency for the 3D model presents a significant limitation. As previous simulations have assessed, the frequency of the drag ought to be double that of the lift frequency to achieve a correlation well-established in the literature, [22]-[23], which stems from the insensitivity of drag to the direction of vortexes present behind bluff bodies. However, accomplishing this correlation in the Ansys analysis of

the 3D model requires a different mesh configuration, specifically the implementation of dynamic mesh. This change leads to a notable increase in computational costs and analysis complexity, necessitating more powerful processors. Unfortunately, the standard computer cannot support such simulations.
To illustrate the distribution of vortexes along the hanger were created three reference planes at the base, middle, and top of the hanger, an example is given in Figure 4.22. The turbulence effects vary along the length, as demonstrated in Figure 4.23.

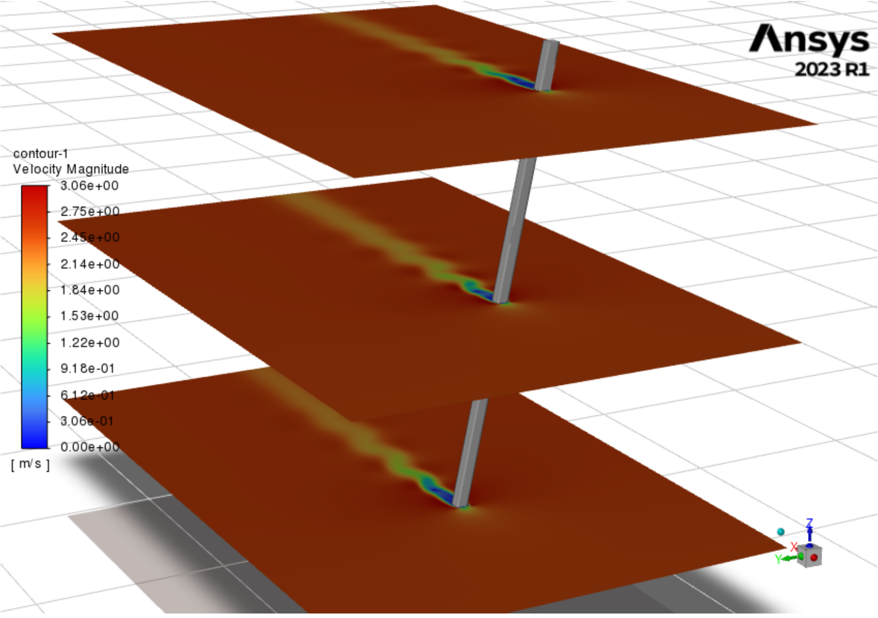

Figure 4.22: 2.5 m/s Wind Velocity Contour.

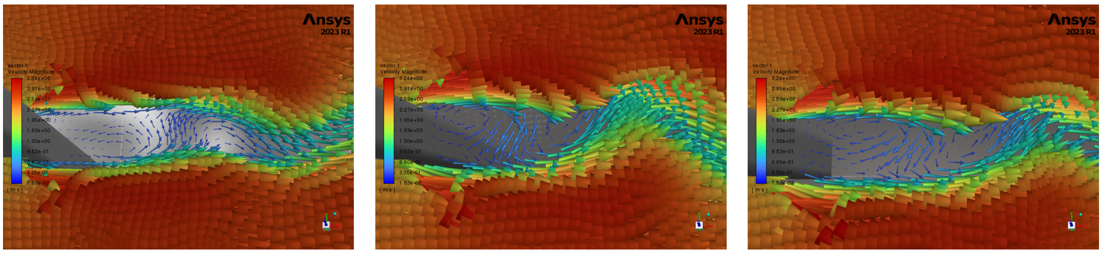
(a) TOP plane (b) Mid plane (c) Bottom plane

Figure 4.23: Velocity magnitude vectors for wind speed of 2.5 m/s.

4.5 Results Discussion

The simulations provide an extensive comprehension of the aerodynamic performance of the hanger section in changing wind scenarios. The differentiation between steady-state and transient simulations offered beneficial observations, enabling the detection of temporally dependent occurrences, such as shedding frequencies.

However, the steady solution overestimates the magnitude of the aerodynamic coefficients and fails to provide any information about the shedding frequency and time-dependent response of the cross-section. This type of simulation remains a valid technique for obtaining an overview of the aerodynamic effects on the structure and for investigating different factors that impact the dynamic behavior of the structure.
Nonetheless, the steady-state simulation unveiled trends in aerodynamic coefficients that pertained to drag, lift, and moment. These trends are also applicable to the unsteady solution.
Importantly, the effects of geometry, particularly the presence of rounded edges, showed a decrease in drag coefficients and an improvement in stability. These findings establish the foundation for succeeding transient simulations.

Moving to transient solutions, by exploring a single rectangular cross-section at varying wind speeds, the dynamic response of the structure was clarified. The variability in aerodynamic coefficients, particularly drag, highlighted the structure's sensitivity to wind speeds of different magnitudes. The examination of shedding frequencies and the Strouhal number disclosed a transition from consistent to inconsistent vortex shedding configurations as the wind speed increased.

The examination of different sections within the field of wind brings to light the complexity of inter-sectional interactions. However, the results obtained from the multisectional model do not differ significantly from those obtained from the single rectangular cross-section. This model incurs a higher computational cost. Therefore, for the purpose of this case study, it suffices to consider only one cross-section to represent the dynamic behavior of the entire structure. However, this modeling can be considered for advanced purposes in order to deeply investigate interactions between diverse structures in a single wind domain.

The findings of the 3D unsteady analysis of Hanger H16 demonstrate a nuanced pattern in aerodynamic coefficients, primarily in the drag coefficient, as wind speeds increase. The differences revealed in the 3D model, in comparison to its 2D equivalent, emphasize the importance of taking into account three-dimensional factors in aerodynamic simulations. However, the 2D analysis can be deemed sufficiently accurate for the purpose of this thesis.
Additionally, the unanticipated fluctuations in lift frequency, particularly at designated wind speeds, introduce an added layer of complexity to the examination. The constraints faced, particularly in obtaining the drag-frequency correlation, highlight the

difficulties associated with moving from 2D to 3D simulations. The requirement for dynamic mesh configurations, while improving accuracy, results in considerable computational demands.

The incorporation of Eurocode standards into wind load calculations has highlighted the significance of examining the impact of wind velocities on critical factors required to determine the inertial force linked to the analysis of vortex shedding. Evaluating Strouhal numbers against Eurocode values underscored the variability with wind velocity, which has a crucial impact on the likelihood of resonant vibrations, and increment the magnitude of the inertial wind force that takes into account the effect of vortex shedding.

Essentially, a complete view of the aerodynamic characteristics of the hanger section is obtained by thoroughly evaluating steady-state, transient simulations, and wind load calculations. This study provides important insights into the impact of wind on structures, which are crucial for developing and evaluating safety protocols in wind engineering design. The results offer valuable information that can be used to enhance the understanding of the subject.

Conclusions

This research provides a thorough investigation into the dynamic interactions between bridge hangers and wind forces, providing valuable insights into key aspects that greatly enhance the understanding of hanger behaviour under various wind conditions.

The set objectives outlined in the introduction have been meticulously achieved through a carefully structured sequence of chapters. The examination of various hanger configurations, spanning from single hangers to multi-section designs, yielded valuable insights into how the quantity and placement of hangers affect the dynamic response of the whole structure. The intricacy of the coupling effects, mode shapes, and natural frequencies became evident, emphasising the necessity of a comprehensive approach to modelling the hanger.

The incorporation of transient analyses introduced a temporal component to the study, thereby facilitating additional exploration of the phenomenon of vortex shedding. Notably, the influence of rounded edges on drag coefficients emerged as a key factor affecting stability and shedding patterns. Limitations and challenges concerning transient analyses, such as computational demands and the requirement for dynamic mesh configurations, were acknowledged.

The comparison between two-dimensional (2D) and three-dimensional (3D) models has yielded crucial insights into the importance of three-dimensional (3D) considerations in aerodynamic simulations. The subtle differences in the aerodynamic coefficients, notably in the drag coefficient, underscore the necessity for a global approach that accounts for geometric complexities to accurately represent the behaviour of the hanger. The practical implications of these findings for bridge design have been analysed, recognising the challenges associated with dynamic mesh configurations in 3D models.

The incorporation of Eurocode standards into the wind load calculations provided a practical aspect of the study. When compared with Eurocode parameters, the assessment of critical wind speeds for vortex shedding highlighted the importance of considering shedding frequencies when assessing inertial wind forces. It also highlighted the importance of considering not only the crosswind response but also the tailwind response. In this particular case, the shedding frequencies due to drag were within the critical range of the natural frequencies of the body under consideration. This correlation between theoretical standards and generated results contributes to the wider application of the findings in real engineering scenarios.

Through the research process, particular research queries were utilized as guidance in analyzing crucial aspects of the interaction between hangers and wind. The findings and debates elaborated on inherent intricacies in hanger performance, thereby presenting applicable considerations to enhance the design and safety of bridges in areas susceptible to wind hazards.

The findings of this research provide valuable practical information for monitoring and understanding the dynamic behaviour of the bridge under investigation. Gaining knowledge of the hangers' dynamics influenced by wind forces in conjunction with geometry and wind speed helps to fine-tune the design of forthcoming bridges. The research emphasises the significance of embracing modern computational modelling techniques to accurately capture the complexity of wind-structure interactions.
Nevertheless, it is crucial to acknowledge some limitations. The research centred primarily on a particular type of bridge and hanger configuration, and extrapolating the outcomes to dissimilar structures necessitates prudence. Future research efforts must address the practical challenges posed by the computational demands of dynamic mesh configurations in 3D models.

This thesis offers a significant contribution to the ongoing discussion on the impact of wind on the hangers of the Bomarsund Bridge by providing a thorough investigation of their dynamics under varying wind conditions. The results can be used by professionals and researchers. The findings obtained from this research can be of practical value in the monitoring of Bomarsund and future designs of bridges, enhancing their safety and resilience. In conclusion, this study provides a basis for subsequent investigations in the wider area of wind-structure interactions, with a direct application to the study of structural fatigue in the field of wind engineering and bridges.

Appendix A

Abaqus Appendix

In this section are reported for each model created on Abaqus the ten mode shapes and the relative frequencies.

A.1 H16

Table A.1: Model H16: First ten Frequencies

H16			
MODE	EIGENVALUE	FREQUENCY	
		(RAD/s)	(Hz)
1	1733.1	41.63	6.6257
2	7798.2	88.307	14.055
3	24185	155.52	24.751
4	56929	238.6	37.974
5	1.10E+05	330.92	52.667
6	1.20E+05	346.63	55.167
7	1.58E+05	396.88	63.166
8	1.87E+05	431.88	68.735
9	1.88E+05	433.47	68.99
10	2.08E+05	455.53	72.5

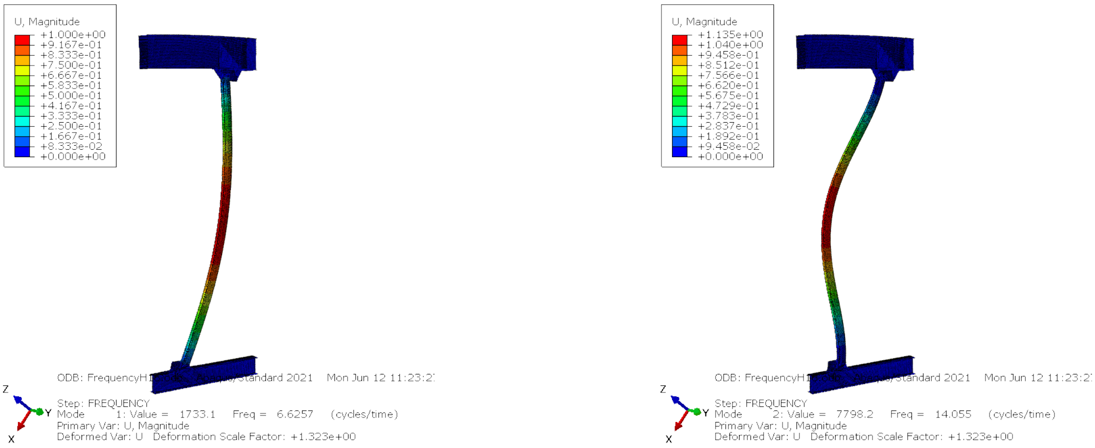

(a) Mode 1

(b) Mode 2

Figure A.1: Mode shapes model H16 (continued)

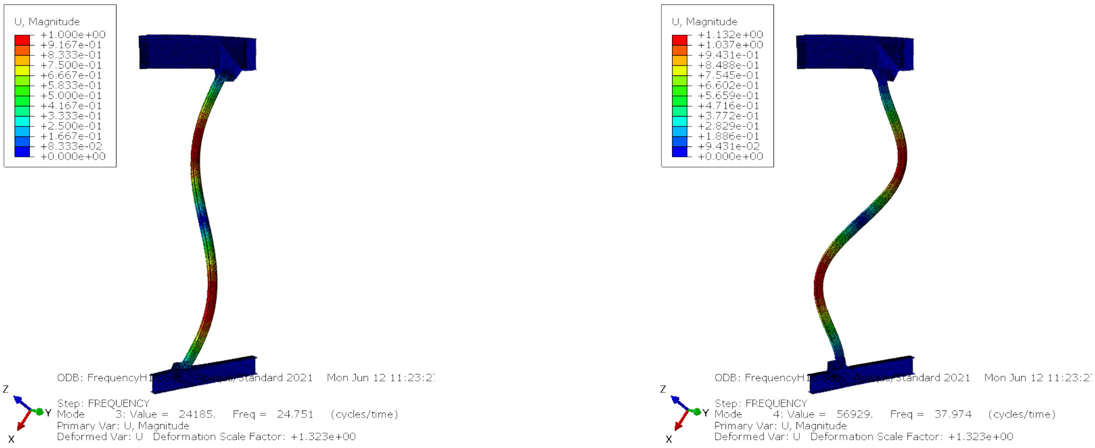

(c) Mode 3

(d) Mode 4

Figure A.1: Mode shapes model H16 (continued)

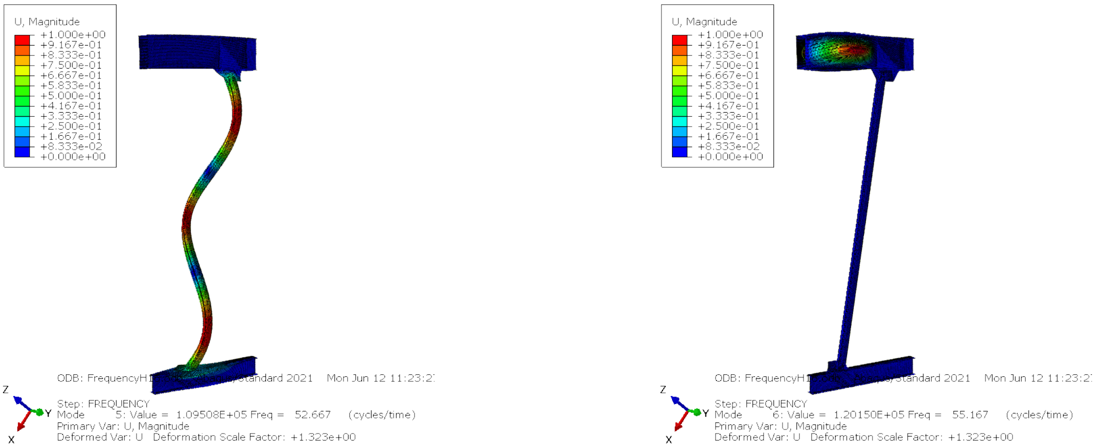

(e) Mode 5

(f) Mode 6

Figure A.1: Mode shapes model H16 (continued)

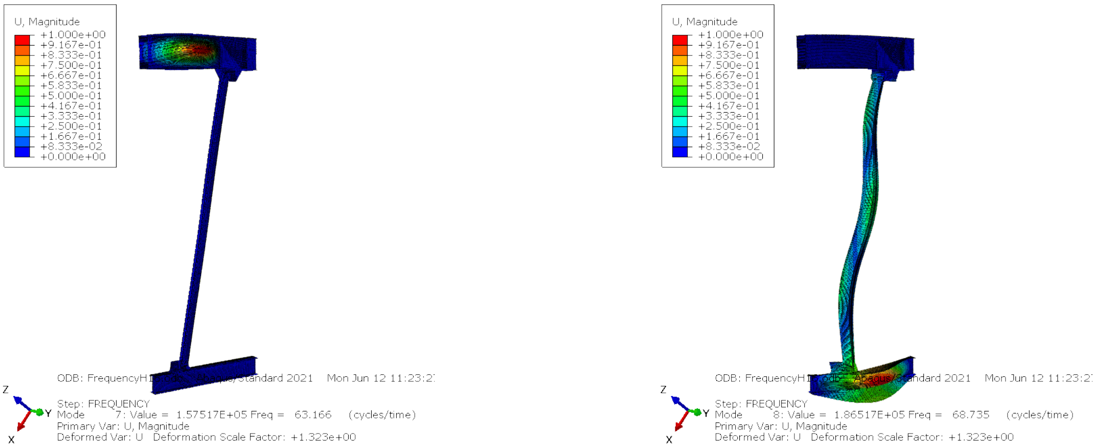

(g) Mode 7

(h) Mode 8

Figure A.1: Mode shapes model H16 (continued)

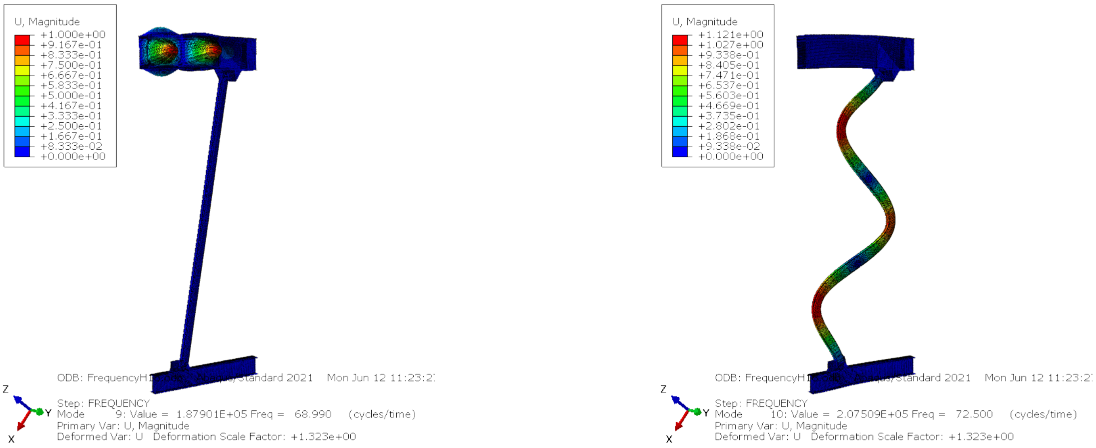

(i) Mode 9

(j) Mode 10

Figure A.1: Mode shapes model H16 (continued)

A.2 H15-16

Table A.2: Model H15-16: First ten Frequencies

H15-16			
MODE	EIGENVALUE	FREQUENCY	
		(RAD/s)	(Hz)
1	1635.2	40.438	6.4359
2	2203.2	46.938	7.4705
3	7769.7	88.146	14.029
4	7998	89.431	14.233
5	19775	140.62	22.381
6	27128	164.7	26.214
7	42362	205.82	32.757
8	56621	237.95	37.871
9	58436	241.73	38.473
10	62383	249.77	39.751

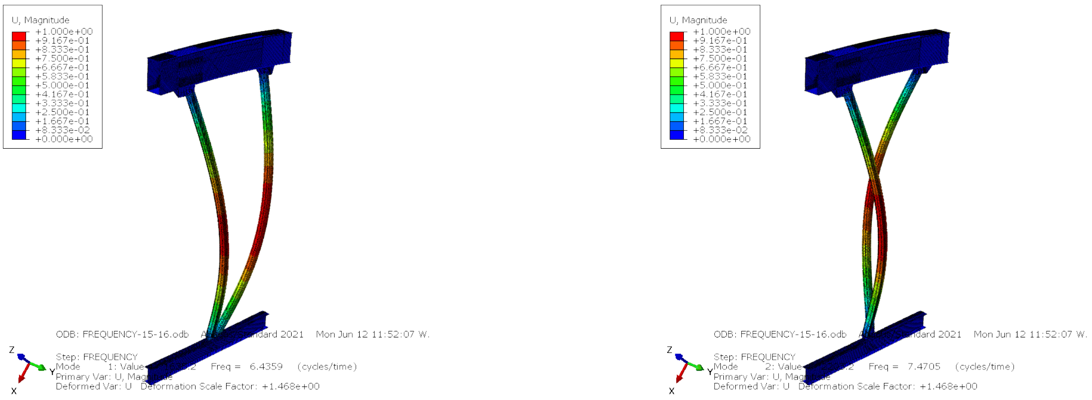

(a) Mode 1

(b) Mode 2

Figure A.2: Mode shapes model H15-16 (continued)

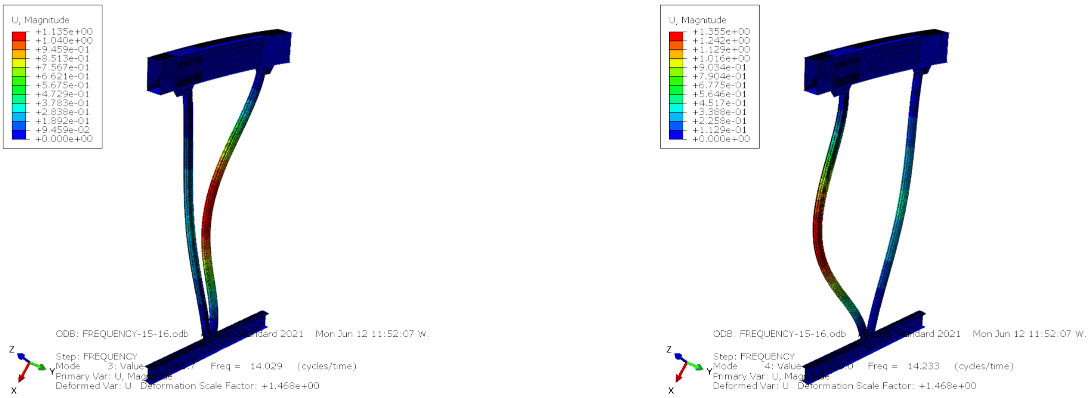

(c) Mode 3

(d) Mode 4

Figure A.2: Mode shapes model H15-16 (continued)

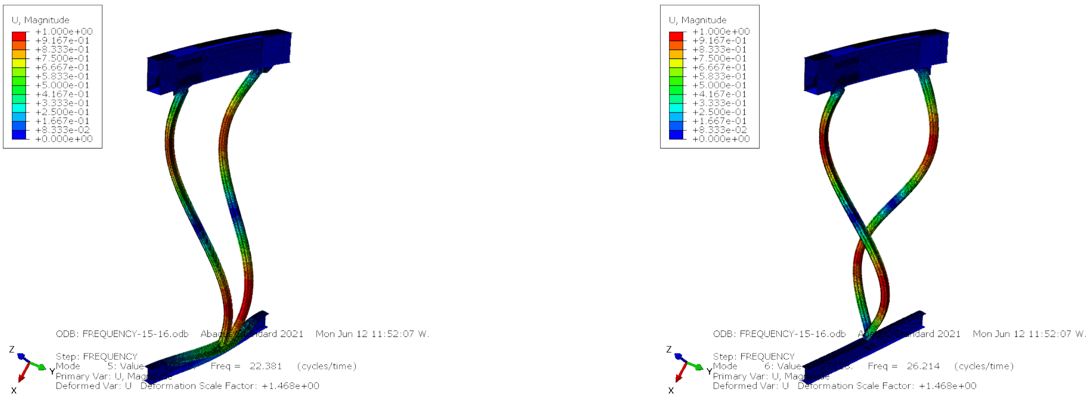

(e) Mode 5

(f) Mode 6

Figure A.2: Mode shapes model H15-16 (continued)

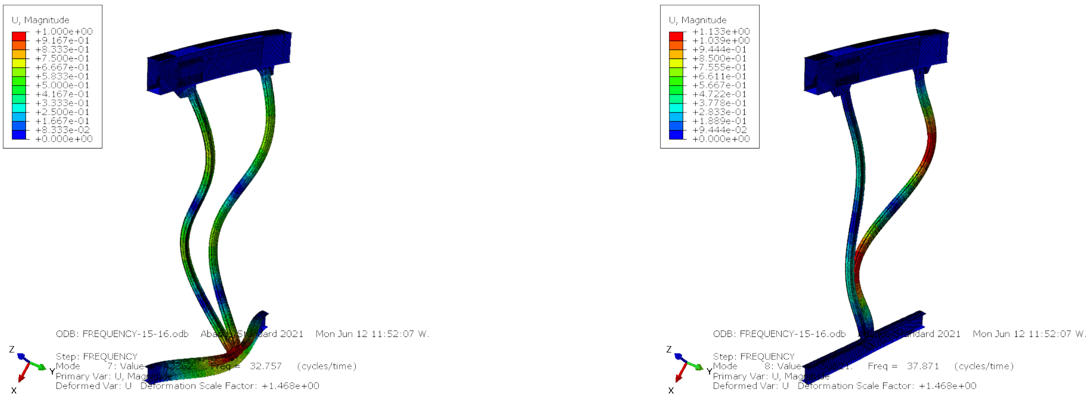

(g) Mode 7

(h) Mode 8

Figure A.2: Mode shapes model H15-16 (continued)

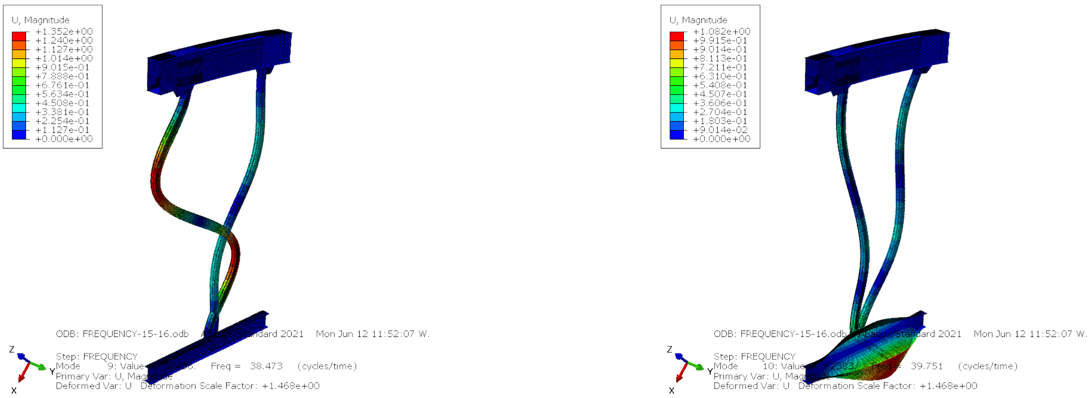

(i) Mode 9

(j) Mode 10

Figure A.2: Mode shapes model H15-16 (continued)

A.3 H14-16

Table A.3: Model H14-16: First ten Frequencies

14-16			
MODE	EIGENVALUE	FREQUENCY	
		(RAD/s)	(Hz)
1	1598.40	39.98	6.36
2	1890.00	43.47	6.92
3	2382.50	48.81	7.77
4	7735.50	87.95	14.00
5	7780.70	88.21	14.04
6	7980.80	89.34	14.22
7	14997.00	122.46	19.49
8	24906.00	157.82	25.12
9	26087.00	161.51	25.71
10	27910.00	167.06	26.59

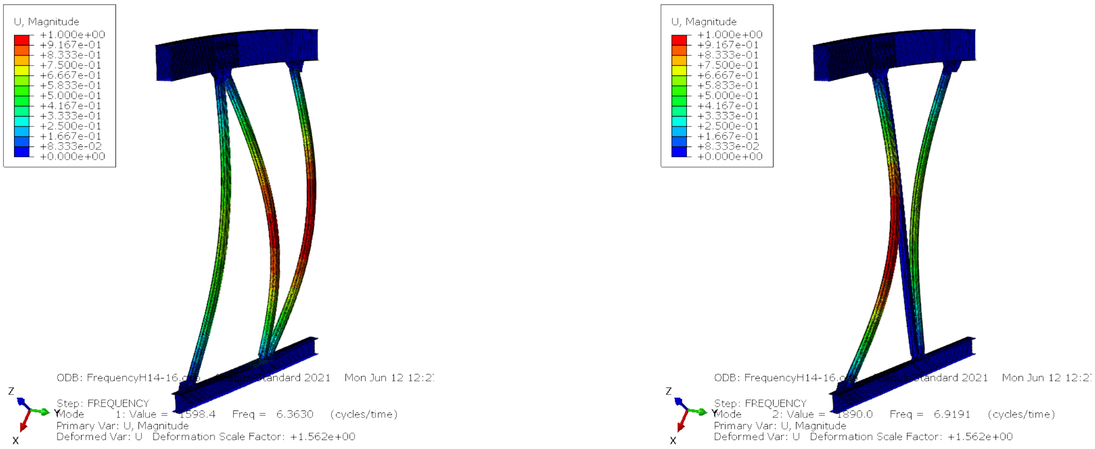

(a) Mode 1

(b) Mode 2

Figure A.3: Mode shapes model H14-16 (continued)

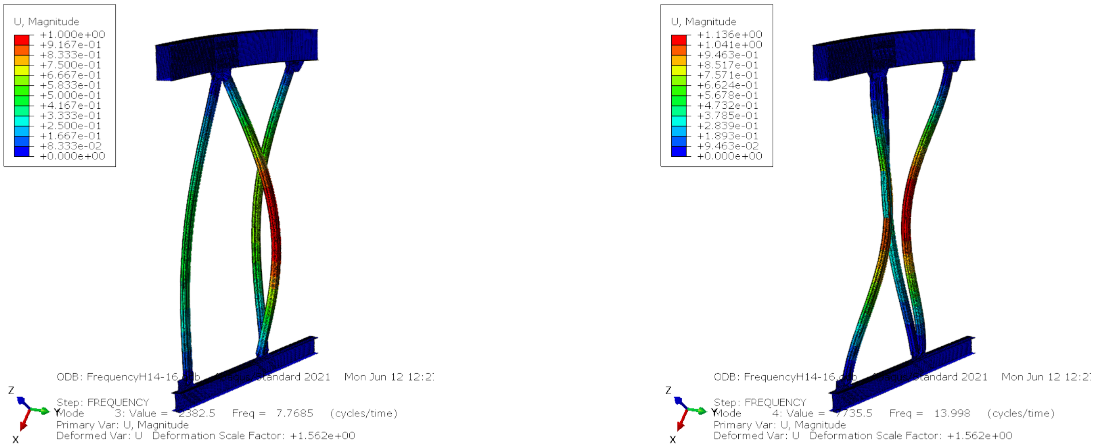

(c) Mode 3 (d) Mode 4

Figure A.3: Mode shapes model H14-16 (continued)

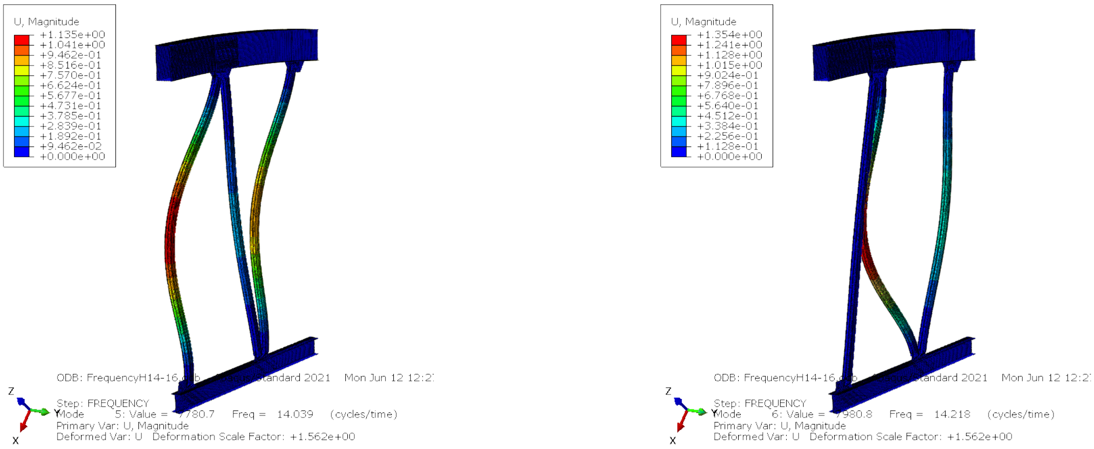

(e) Mode 5 (f) Mode 6

Figure A.3: Mode shapes model H14-16 (continued)

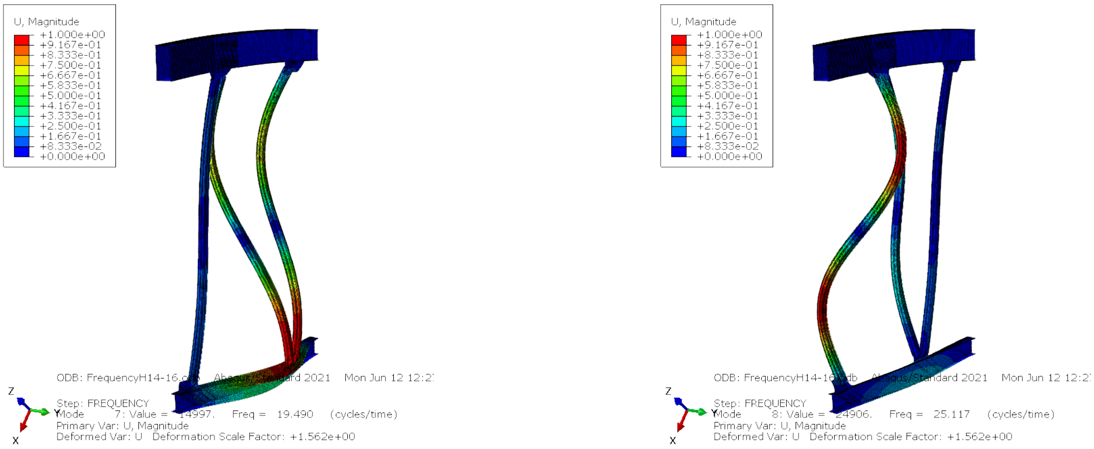

(g) Mode 7 (h) Mode 8

Figure A.3: Mode shapes model H14-16 (continued)

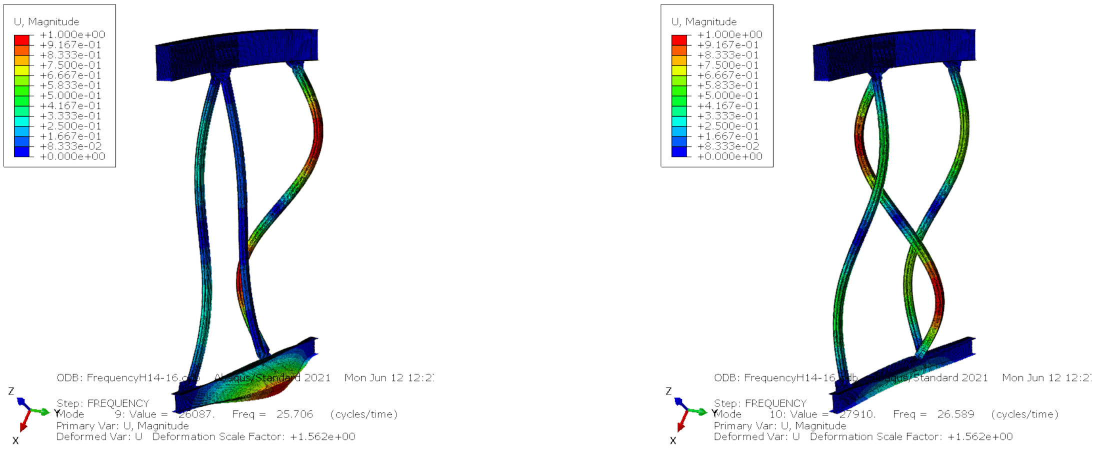

(i) Mode 9

(j) Mode 10

Figure A.3: Mode shapes model H14-16- (continued)

A.4 H14-17

Table A.4: Model H14-17: First ten Frequencies

H14-17			
MODE	EIGENVALUE	FREQUENCY (RAD/s)	(Hz)
1	1476.60	38.43	6.12
2	1823.50	42.70	6.80
3	2032.40	45.08	7.18
4	2499.40	49.99	7.96
5	6921.40	83.20	13.24
6	7672.00	87.59	13.94
7	7714.60	87.83	13.98
8	7922.00	89.01	14.17
9	8059.90	89.78	14.29
10	14404.00	120.02	19.10

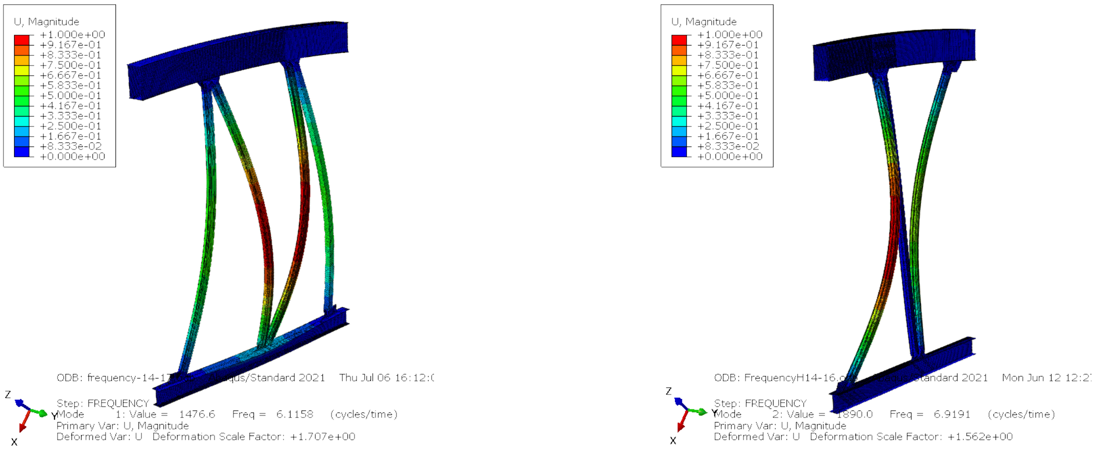

(a) Mode 1

(b) Mode 2

Figure A.4: Mode shapes model H14-17 (continued)

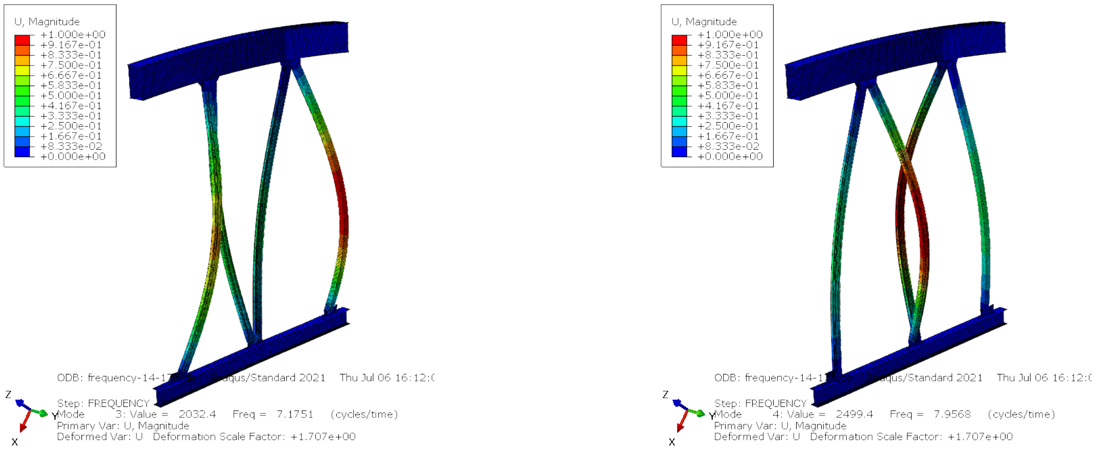

(c) Mode 3

(d) Mode 4

Figure A.4: Mode shapes model H14-17 (continued)

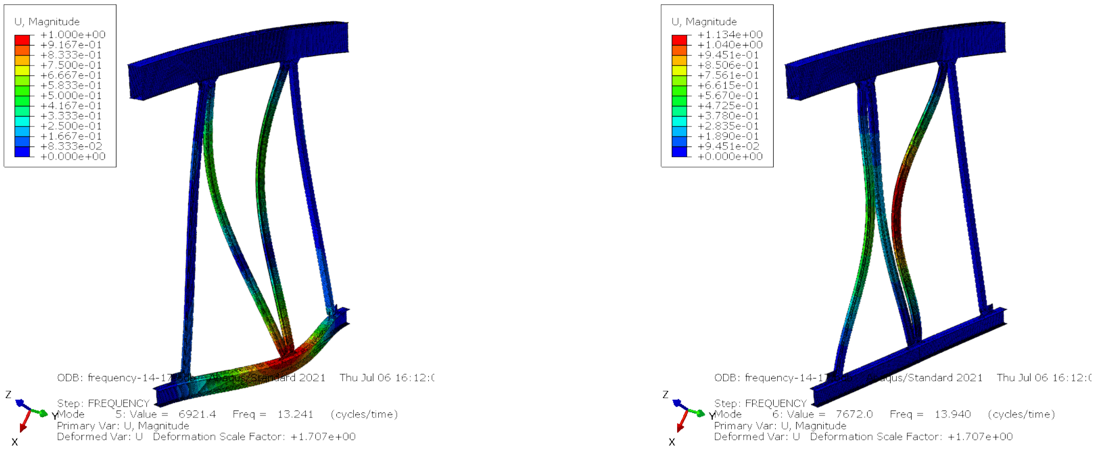

(e) Mode 5

(f) Mode 6

Figure A.4: Mode shapes model H14-17 (continued)

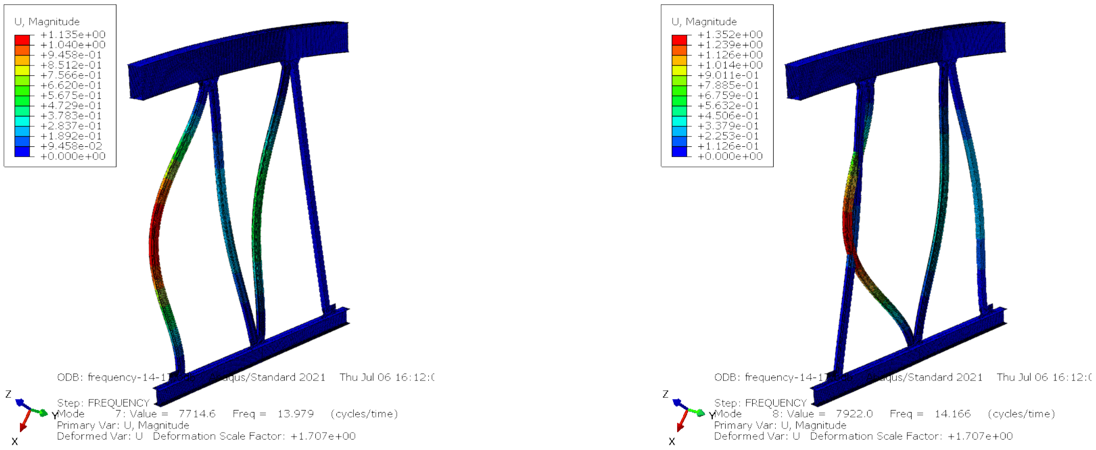

(g) Mode 7

(h) Mode 8

Figure A.4: Mode shapes model H14-17 (continued)

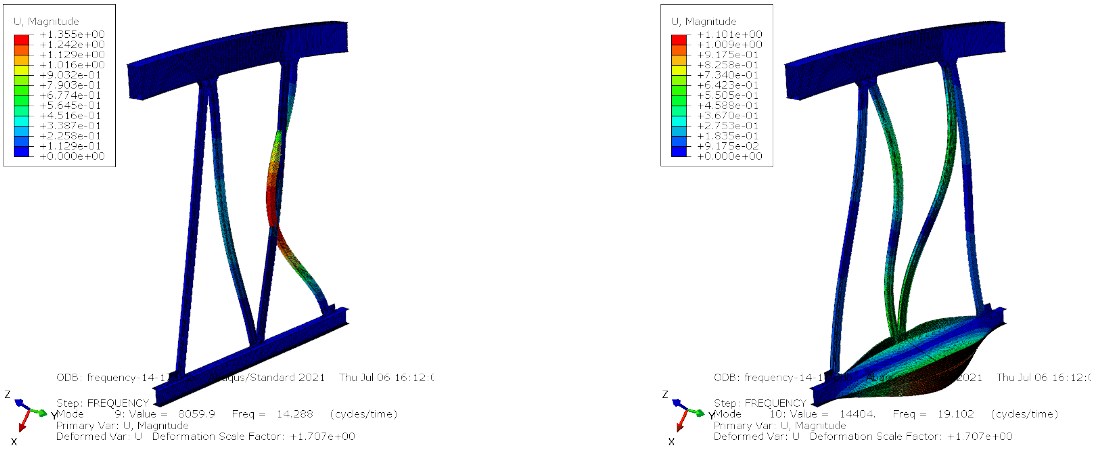

(i) Mode 9

(j) Mode 10

Figure A.4: Mode shapes model H14-17- (continued)

A.5 H12-19

Table A.5: Model H12-19: First ten Frequencies

H12-19			
MODE	EIGENVALUE	FREQUENCY	
		(RAD/s)	(Hz)
1	1578.7	39.733	6.3236
2	1814.3	42.595	6.7791
3	1930.5	43.938	6.9929
4	2016	44.9	7.146
5	2.11E+03	45.957	7.3143
6	2.26E+03	47.566	7.5703
7	2.41E+03	49.066	7.8092
8	2.47E+03	49.666	7.9046
9	3.95E+03	62.869	10.006
10	7.47E+03	86.427	13.755

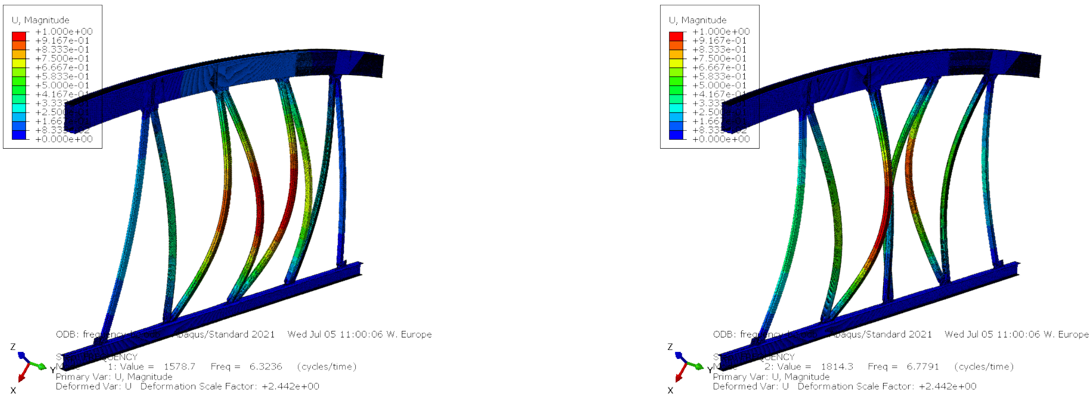

(a) Mode 1

(b) Mode 2

Figure A.5: Mode shapes model H12-19 (continued)

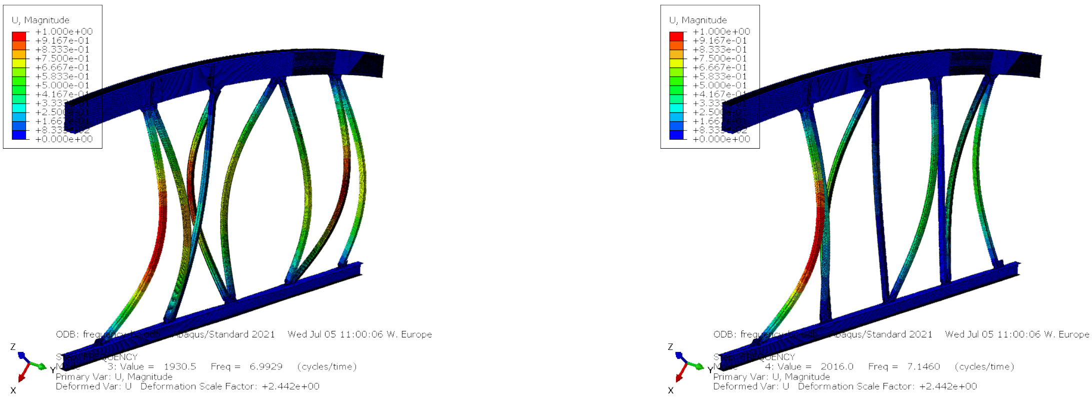

(c) Mode 3 (d) Mode 4

Figure A.5: Mode shapes model H12-19 (continued)

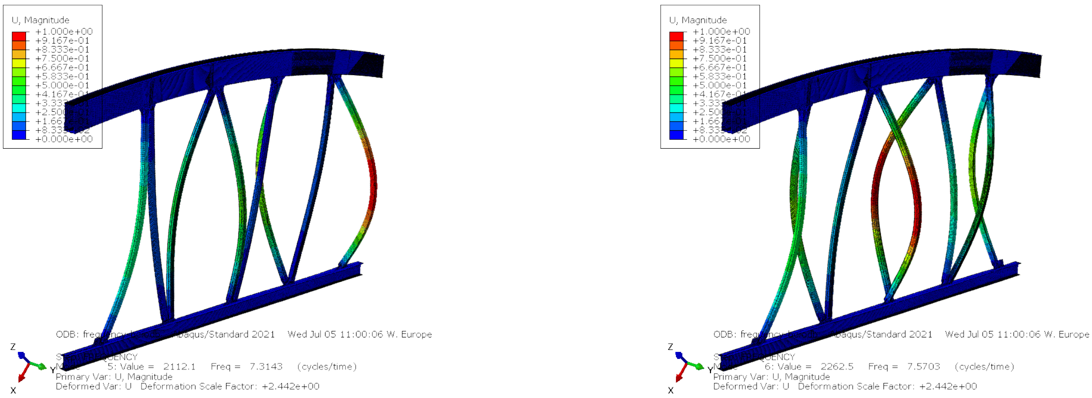

(e) Mode 5 (f) Mode 6

Figure A.5: Mode shapes model H12-19 (continued)

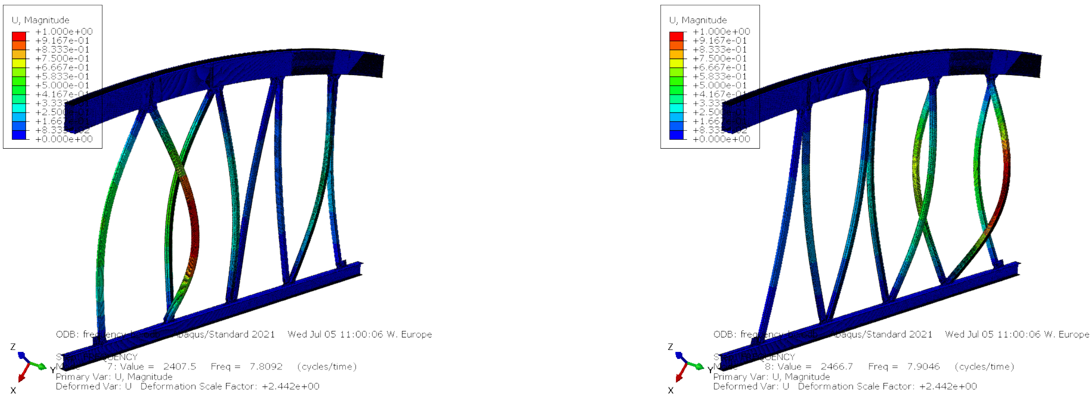

(g) Mode 7 (h) Mode 8

Figure A.5: Mode shapes model H12-19 (continued)

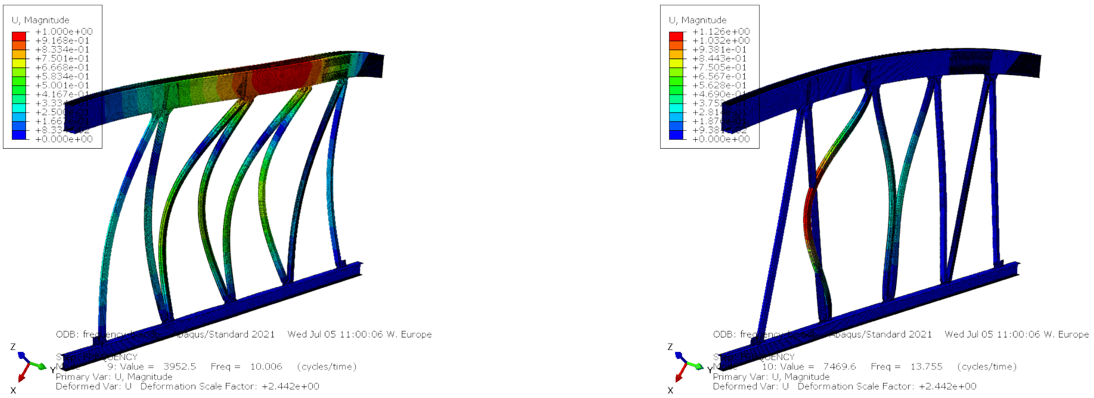

(i) Mode 9

(j) Mode 10

Figure A.5: Mode shapes model H12-19 (continued)

Appendix B

Ansys Fluent Appendix

B.1 Ansys Fluent 2D Simulation

In this section are collected tables related to CFD analysis.

B.1.1 2D Steady simulation

Table B.1: 2D Ansys Fluent simulation settings

Model	Settigns
Space	2D
Time	Steady & Transient
Viscous	Realizable k-epsilon turbulence model
Wall treatment	Enhanced wall treatment
Iterations Steady solution	6000/12000
Iterations Transient solution	6000
Time Step Transient solution [s]	0.010
Reference Area [m^2]	0.254
Method	Simple

	Material properties -Air	
Density [kg/m^3]	1.225	constant
Viscosity [kg/(ms)]	1.79E-05	constant

	Boundary Conditions	
Inlet	Velocity Magnitude [m/s]	2,5 / . . . / 30
	Turbulent Intensity [%]	5.000
	Hydraulic Diameter [m]	1.820
Outlet	Gauge Pressure [Pa]	0.000
	Backflow Turbulent Intensity [%]	5.000
	Backflow Turbulent Viscosity Ratio	10.000
Wall	Wall Motion	Stationary
	Shear Boundary Condition	No Slip

B.1.2 2D Unsteady Simulations

Table B.2: Unsteady solution: Aerodynamic coefficients for rectangular cross section.

v [m/s]	2.5	5.0	7.5	10.0	15.0	20.0	25.0	27.0	30.0
Re	4.3e4	8.7e4	1.3e5	1.7e5	2.6e5	3.5e5	4.3e5	4.7e5	5.2e5
C_D	1.682	1.713	1.718	1.689	1.607	1.519	1.439	1.419	1.401
C_L	-0.689	0.814	-0.247	-0.078	-0.327	-0.158	0.057	0.007	-0.063
C_M	-8.693	-3.912	-7.397	-6.733	-7.227	-6.341	-5.330	-5.419	-5.575

Table B.3: Unsteady solution: Estimated peak frequencies and related amplitudes.

v [m/s]	2.5	5.0	7.5	10.0	15.0
Drag Estimated Peak Frequency [Hz]	2.600	4.880	6.800	8.380	11.000
Lift Estimated Peak Frequency [Hz]	1.280	2.440	3.400	4.200	5.499
Drag Amplitude	0.023	0.026	0.031	0.025	0.014
Lift Amplitude	0.338	0.798	0.891	0.709	0.568

v [m/s]	20.0	25.0	27.0	30.0
Drag Estimated Peak Frequency [Hz]	13.080	14.180	14.460	14.840
Lift Estimated Peak Frequency [Hz]	6.549	7.082	7.220	7.432
Drag Amplitude	0.004	0.001	0.001	0.000
Lift Amplitude	0.302	0.110	0.075	0.065

Table B.4: Unsteady solution: Strouhal number

v [m/s]	2.5	5.0	7.5	10.0	15.0	20.0	25.0	27.0	30.0
St	0.129	0.124	0.115	0.107	0.093	0.083	0.072	0.068	0.063

Table B.5: Unsteady solution data extracted for each speed simulated

v [m/s]	2.5	5.0	7.5	10.0	15.0	20.0	25.0	27.0	30.0
n° time steps	6000	6000	6000	6000	6000	6000	6000	6000	6000
steps size [s]	0.010	0.010	0.010	0.010	0.010	0.010	0.010	0.010	0.010
C_D	1.682	1.713	1.718	1.689	1.607	1.519	1.439	1.419	1.401
C_L	-0.689	0.814	-0.247	-0.078	-0.327	-0.158	0.057	0.007	-0.063
C_M	-8.693	-3.912	-7.397	-6.733	-7.227	-6.341	-5.330	-5.419	-5.575
Drag f [Hz]	2.600	4.880	6.800	8.380	11.000	13.080	14.180	14.460	14.840
Lift f [Hz]	1.280	2.440	3.400	4.200	5.499	6.549	7.082	7.220	7.432
D.Amplitude	0.023	0.026	0.031	0.025	0.014	0.004	0.001	0.001	0.000
L.Amplitude	0.338	0.798	0.891	0.709	0.568	0.302	0.110	0.075	0.065
St	0.129	0.124	0.115	0.107	0.093	0.083	0.072	0.068	0.063
D. Force [N]	1.634	6.656	15.025	26.252	56.220	94.471	139.774	160.804	195.949
L. Force [N]	0.669	3.162	2.158	1.216	11.421	9.839	5.518	0.773	8.768

B.2 Ansys Fluent 3D Simulations

Table B.6: Unsteady 3D analysis: simulation extracted data.

Wind speed [m/s]	2.5	10.0	20.0	27.0	30.0
Re	4.34E+04	1.74E+05	3.47E+05	4.69E+05	5.21E+05
n° time steps	6000	6000	6000	6000	6000
time steps size [s]	0.010	0.010	0.010	0.010	0.010
Drag Coeff. CD	1.307	1.235	1.234	1.234	1.233
Lift Coef. CL	-0.008	-0.053	-0.053	-0.053	-0.053
Moment Coeff. CM	1.233	0.077	1.166085	0.011	1.165
Lift Estimated Peak Frequency [Hz]	1.340	2.960	5.680	7.420	8.120
Drag Amplitude	8.70E-03	1.03E-05	9.41E-06	1.05E-05	1.16E-05
Lift Amplitude	1.49E-02	5.44E-05	4.30E-05	4.37E-05	4.65E-05
Estimated Strouhal Number from Lift	0.134	0.074	0.071	0.069	0.068
Drag Force [kN]	1.41E-02	2.14E-01	8.54E-01	1.56E+00	1.92E+00
Lift Force [kN]	8.91E-05	9.25E-03	3.69E-02	6.73E-02	8.31E-02

Bibliography

[1] European Committee for Standardization (CEN), *Eurocode EN 1991-1-4: Wind Load*, 2005, CEN.

[2] Yunus A. Çengel and John M. Cimbala, *Fluid Mechanics*, 2008, McGraw-Hill.

[3] John D. Anderson, *Fundamentals of Aerodynamics*, 2010, McGraw-Hill Education.

[4] J. Gordon Leishman, *Introduction to Aerospace Flight Vehicles*, 2022,

[5] Paul A. Durbin and Gorazd Medic, *Fluid Dynamics with a Computational Perspective, Chapter ´Creeping Flow´*, 2007, Cambridge University Press.

[6] Pijush K. Kundu and Ira M. Cohen and David R. Dowling and Grétar Tryggvason, *Fluid Mechanics, Sixth Edition*, chapter 10, *Boundary Layers and Related Topics*, 2015, Academic Press.

[7] Gersten, K., Radespiel, Rolf and Rossow, Cord-Christian and Brinkmann, Benjamin Winfried, *Hermann Schlichting and the Boundary-Layer Theory*, *Hermann Schlichting – 100 Years*,pp 3-17, 2009, Springer Berlin Heidelberg.

[8] J. Wright = Encyclopedia of Vibration,FLUTTER, pp 553-565, 2001, Elsevier, Oxford.

[9] Alberto Carpinteri, *Advanced Structural Mechanics*, 2017, CRC Press, Taylor and Francis Group.

[10] T.J.A. Agar, *Aerodynamic Flutter Analysis of Suspension Bridges by a Modal Technique*, 1989, Engineering Structures.

[11] Lian, Jijian and Yan, Xiang and Liu, Fang and Zhang, Jun and Ren, Quanchao and Yang, Xu, *Experimental Investigation on Soft Galloping and Hard Galloping of Triangular Prisms* 2017, Applied Sciences.

[12] Z.T. Zhang and Y.J. Ge and Y.X. Yang, *Torsional stiffness degradation and aerostatic divergence of suspension bridge decks*, 2013, Journal of Fluids and Structures.

[13] E.H. Dowell and R. Clark and others, *A Modern Course in Aeroelasticity*, Fourth Revised and Enlarged Edition, 2004, Kluwer Academic Publishers

[14] Raymond L. Bisplinghoff and Holt Ashley and Robert L. Halfman, *Aeroelasticity*, 1996 Addison-Wesley.

[15] Ansys Fluent 12.0 Theory Guide, *Modeling Turbulence, Chapter 12-24*, 2009 Ansys Inc.

[16] Salim, Salim M. and Cheah, S.C., *Wall y+ strategy for dealing with wall-bounded turbulent flows*, Vol 2, 2009, Int. MultiConf. Eng. Comput. Sci. (IMECS).

[17] Karlson, M.; Nita, B.G.; Vaidya, A., *Numerical Computations of Vortex Formation Length in Flow Past an Elliptical Cylinder.* Fluids Vol. 5, 157, 2020.

[18] Prasenjit Dey and Ajoy Kr. Das, *Numerical analysis of drag and lift reduction of square cylinder*, Engineering Science and Technology, an International Journal, Vol. 18-4, pp. 758-768, 2015.

[19] Mehmet Ishak Yuce, Dalshad Ahmed Kareem, *A Numerical Analysis of Fluid Flow Around Circular and Square Cylinders*, American Water Works Association AWWA, Vol. 108-10, pp. E546-E554, 2016.

[20] L. Mao, Q. Liu, G. Wang, and S. Zhou, *Lift force, drag force, and tension response in vortex-induced vibration for marine risers under shear flow*, Vibroengineering, Vol. 18-2, pp. 1187–1197, 2016.

[21] Williamson C. H. K., Roshko A., *Vortex formation in the wake of an oscillating cylinder*, Journal of Fluids and Structures, Vol. 2, pp. 355-381, 1988.

[22] Dahl J.M., Hover F.S., Triantafyllou M.S. *Two-degree-of-freedom vortex-induced vibrations using a force-assisted apparatus* Journal of Fluids and Structures, Vol.22, pp. 807-818, 2006.

[23] Enhao Wang, Qing Xiao, Atilla Incecik, *Three-dimensional numerical simulation of two-degree-of-freedom VIV of a circular cylinder with varying natural frequency ratios at Re=500*, Journal of Fluids and Structures, Vol. 73, pp. 162-182, 2017.